

Abstract

Highly frustrated systems have degenerate ground states that lead to novel properties. In magnetism its consequences underpin exotic and technologically important effects: high temperature superconductivity, colossal magnetoresistance, and the anomalous Hall effect. One of the enduring mysteries of highly frustrated magnetism is why certain experimental systems have a spin glass transition that it is not determined by the strength of the dominant magnetic interactions. There have been suggestions that some real materials possess disorder of the magnetic sites or bonds that is responsible for the glassy behaviour. In this project I show that the spin glass transition in the model *kagomé* antiferromagnet hydronium jarosite arises from a spin anisotropy and not random disorder. This simplifies the treatment of the complex spin glass dynamics and has implications far beyond magnetism, as spin glasses provide important models for the out-of-equilibrium dynamics in other frustrated systems, including proteins and neural networks.

Investigations into Geometrical Frustrated
Magnetism: *Kagomé* Antiferromagnets

William Geoffrey Bisson

September 10, 2007

Contents

1	Introduction	19
1.1	Magnetism and the Jarosites	19
2	Theory	25
2.0.1	Magnetic Interactions	25
2.1	Curie-Weiss Law	25
2.1.1	Curie Law	25
2.1.2	Derivation of the Curie constant	26
2.1.3	The Weiss Model	28
2.1.4	Magnetic Order	29
2.2	Frustration	29
2.2.1	Bond Frustration	30
2.2.2	Geometric Frustration	30
2.3	An Introduction to Mean Field Theory	33
2.3.1	Symmetry Breaking	35
2.3.2	Ginzburg-Landau theory	35
2.3.3	Two Dimensional Ising model	35
2.3.4	XY-Model	35
2.3.5	Heisenberg	35
2.4	Spin Glasses	35
2.4.1	Physical Properties of a Conventional Spin Glass	36
2.4.2	Interactions within a Spin Glass	37
2.5	The <i>Kagomé</i> Spin Glass	37
2.5.1	Physical Properties of the <i>Kagomé</i> Spin Glass	37

2.5.2	Anisotropy	37
2.6	Topology	37
2.6.1	Introduction to Homotopy and Theory of Defects	37
2.6.2	<i>Kagomé</i> Network and Triangular Networks	37
2.6.3	Solitons - Implications for the <i>Kagomé</i> Antiferromagnet	37
2.7	Overview of Current Research into Frustrated Magnetism	37
3	Experimental Methods	38
3.1	Chemistry and Synthesis of Fe and Cr jarosites	38
3.2	Hydrothermal Synthesis of Fe jarosites	38
3.2.1	Forced hydrolysis	39
3.2.2	Oxidative Hydrothermal Synthesis	40
3.2.3	Forced hydrolysis and oxidative synthesis of deuterated jarosites	42
3.3	Chemistry and Synthesis of Cr jarosites	43
3.3.1	Hydrothermal Methods	43
3.4	Inductively Coupled Plasma Elemental Analysis Techniques	45
3.4.1	Introduction to Inductively Coupled Plasma	45
3.4.2	Acquisition of the ions for elemental analysis	45
3.4.3	Calibration	46
3.4.4	Sample Preparation	47
3.4.5	Sources of Errors	47
3.4.6	Collection of results	48
3.5	Scanning Electron Microscope	49
3.5.1	SEM Morphology studies	49
3.5.2	EDX SEM Elemental analysis	50
3.6	Superconducting Quantum Interference Device Magnetometry - SQUID	51
3.6.1	Temperature Sweep Measurements - Zero Field Cooled and Field Cooled (ZFC/FC)	54
3.6.2	Field Sweep Measurements	55
3.7	Diffraction	57
3.8	Powder Diffraction	61
3.8.1	Powder Diffraction - X-ray	61
3.8.2	Powder Diffraction - Neutron	63

3.8.3	Rietveld refinement	66
3.9	Single Crystal Diffraction	78
3.9.1	Data collection techniques	78
3.9.2	Structure solution	79
4	Iron jarosites $S = \frac{5}{2}$	81
4.1	Chemistry and Synthesis	81
4.1.1	Hydrothermal Methods(1) - Forced hydrolysis	82
4.1.2	Hydrothermal Methods (2) - Oxidative synthesis	89
4.1.3	Synthesis of Fe jarosite Samples for Neutron Diffraction	92
4.1.4	Mechanism for Jarosite formation	93
4.1.5	Analysis of the two Methods and Comparison with Natural Samples	100
4.2	Results of Hydronium Jarosite Synthesis and Physical Characterisation	103
4.2.1	Elemental Analysis Results	103
4.3	Powder Diffraction Results and Analysis of Iron Jarosites	106
4.3.1	Phase identification	106
4.3.2	Comparison of Lattice Parameters with Spin Glass Transi- tion Temperature for the Hydronium Jarosites using Rietveld Refinement	106
4.3.3	The Non-Hydronium Jarosites	116
4.4	Single Crystal Results and Analysis of Iron Jarosite	116
4.4.1	Structural Changes within the Hydronium Jarosites	124
4.4.2	Implications for the Magnetism of the Structure	124
4.5	Physical Characterisation of Iron Jarosite	124
4.5.1	Zero Field/Field Cooled Measurements	124
4.5.2	Hysteresis Measurements	124
4.5.3	Understanding the Magnetic Structure	124
4.6	Neutron Thermo-diffraction Studies and Magnetic Diffraction of Iron Jarosites	125
4.6.1	Neutron Powder Diffraction Technique	125
4.7	Results and Analysis of Neutron Diffraction for the Iron jarosites	125
4.7.1	Nuclear Structure	125

4.7.2	Magnetic Structure	125
4.8	Origins of the Spin Glass Dynamics in Hydronium Jarosite	125
4.9	Origin of Long Range Magnetic Order in the Non-Hydronium Jarosites	125
4.10	Models to Explain the Anisotropy	125
5	Chromium jarosites $S = \frac{3}{2}$	126
5.1	The Crystallographic Structure	126
5.1.1	Neutron Powder Diffraction at HRPD	126
5.1.2	Neutron Powder Diffraction at D20	128
5.2	The Magnetic Structures of the Chromium Jarosites	128
6	Conclusions	130
6.1	The Iron Jarosites	130
6.2	The Chromium Jarosites	130
6.3	Discussion of the Topological Nature of the <i>Kagomé</i> Network	130
6.4	Comparison between the Classical and the Quantum limit	130
6.5	Future Work	130
A	Crystallography Appendix	131
A.1	Rietveld Refinement	131
A.1.1	Profile Functions	133
A.2	Single Crystal structure solution	134
A.2.1	Direct Methods	135
A.2.2	Patterson methods	137
	Bibliography	138

List of Figures

1.1	a) Polyhedral representation of hydronium jarosite, the O from the H_3O^+ is shown in red representing the A-site. The bridging hydroxyl groups shown in black, which are just above and below the <i>kagomé</i> plane, lead to form a canted Fe-coordinated octahedra. This canting has important consequences for the magnetism of the jarosite structure. b) a view along the <i>c</i> axis showing the canted Fe octahedra and the <i>kagomé</i> network overlaid to show the arrangement of the Fe^{3+} ions.	23
2.1	a) the system's inability to simultaneously minimise all the exchange interactions leads to frustration as shown by the third spin. b) shows two distinct compromise arrangements where the moments are orient 120° from each other. This introduces the concept of chirality into the system	31
2.2	The two diagrams show two red triangles at the centre of a edge sharing lattice of triangles with moments placed at the vertex of each triangle. The red triangles represent the two different chiral forms of antiferromagnetically coupled ions, each moment aligned 120° from each other. Maintaining the 120° alignment the chiral form of the red central triangle propagates coherently throughout the structure because each triangle shares two moments with its nearest neighbours, therefore dictating the alignment of the third moment upon a triangle. The degeneracy therefore does not scale with size and remains with a double degeneracy.	32

2.3	The two diagrams show two red triangles with the same chirality at the centre of a vertex sharing lattice of triangles with moments placed at the vertex of each triangle. The red triangles are both the same chiral form of antiferromagnetically coupled ions, each moment aligned 120° from each other. Maintaining the 120° alignment the chiral form of the red central triangle does not determine the spin configuration of the neighbouring triangular plaquette and as shown either chiral form can be present. For one central chiral form with three nearest neighbours a ground state degeneracy of six can be achieved. This degeneracy scales with the size of the system ultimately producing a macroscopically degenerate ground state.	32
2.4	The different chiralities and spin folds possible for the kagom anti-ferromagnet. The orange and green triangles have the $\kappa = +1$ and the $\kappa = -1$ chiralities respectively. Zero energy excitations termed ‘spin folds’ (highlighted in yellow) can occur within structures with both uniform and staggered chiralities: a) shows an ‘open spin fold’, which traverses a lattice if based upon the uniform chirality (the $\mathbf{q} = 0$ structure); b) shows a ‘closed spin fold’ based upon a lattice with staggered chirality (the $\sqrt{3} \times \sqrt{3}$ structure).	34
3.1	The Pyrex tubes from Ace Glass Inc., provided an excellent reaction for hydrothermal synthesis. There are many advantages of using Pyrex pressure tubes over conventional bombs: firstly, a better temperature gradient through the reaction vessel; secondly, it allows visual inspection of the reaction; thirdly, it gives a far better surface for jarosite crystal growth and finally it allows for a rapid turnaround and mass production of jarosite synthesis. The positioning of the Pyrex tube at an angle of deviation from upright of approximately 35° was found to provide the best angle for crystal growth up the Pyrex tube. The divisions on the ruler show millimeters.	41

3.2	Bomb design for Cr jarosite synthesis. Temperatures reaching 300°C are needed for Cr jarosite synthesis and the need for a heavy duty bomb made from stainless steel. A Pyrex tube, fashioned by glass blowing which contains the reactants, is slipped into the bomb and 15cm ³ of water added to equalize the pressure upon the Pyrex tube. A stainless steel plug (Figure 3.2(b)) with back fitted O-ring fits neatly into gap and is secured using another cap.	44
3.3	Schematic for DC SQUID. a) shows the pickup coils where the magnetic flux from the sample is detected, either in the absence or with an applied field. b) shows the loop with the two Josephson junctions at points X and Y. The current is recombined at Z and the output from Z is shown in c). The oscillating voltage relates to the magnetic flux applied at X, obtained from the interference of the two superconducting phases passing through X and Y.	52
3.4	An expected hysteresis loop by applying large positive and negative fields to produce saturation in the magnetisation of the sample. The gap produced by the two magnetisation curves is called the coercivity and describes the hardness of the system. A more fluid movement of reorientation of spins will result in a small coercivity	56
3.5	Positive hysteresis loops taken from a virgin curve. A small field is gradually applied (red squares) whereupon at a field (H_1) the field is gradually reduced to zero and then gradually increased back to H_1 (red circles). The field is continually applied to a new greater field, H_L , whereupon it is gradually decreased to zero field (green line) and following a loop is made from zero to H_1 and back to zero (purple squares) before increasing beyond (orange squares) H_L . Lower insert shows how the two positive sub-loops taken from the virgin curve are not congruent, whereas at 300K (upper insert) the two sub-loops are congruent highlighting that the domains at 300K are acting independently. (This figure is taken from the article [1] investigating magnetic correlations in the high temperature superconductor $\text{La}_{2-x}\text{Sr}_x\text{CuO}_4$ prior to the superconducting transition.)	58

3.6	Predicted displacement hysteresis loops: the corecitivity is expected to be small or negligible but a displacement in the magnetisation between the red and black hysteresis curves. The red hysteresis curve is for where the sample has been field cooled in a small field prior to measurement.	59
3.7	In order for constructive interference to occur, the beam which traverses an extra distance of $2d\sin\theta$, that distance must be equal an integral number of wavelengths, $n\lambda$: as θ increases so the d spacings become smaller.	60
3.8	The Ewald construction shows how the unlikely condition of a Bragg reflection occurs. An incident X-ray with wave vector \mathbf{k} will terminate at any reciprocal lattice point shown as the shaded points on the right. This distance from a chosen origin to that lattice point will form the radius of a diffraction sphere, $k = 2\pi/\lambda$. A Bragg reflection will only occur if the sphere will pass through another reciprocal lattice point. The relationship between wave vector \mathbf{k} and the diffracted beam \mathbf{k}' is the reciprocal lattice vector \mathbf{G} , $\mathbf{k}' = \mathbf{k} + \mathbf{G}$ and the angle θ is the Bragg angle.	62
3.9	Schematic showing the instrument layout for HRPD. The greatest resolution is achieved by the back scattering bank and very useful for small d spacing going out as far as 5-6 Å. The 90° bank has the greatest solid angle and high flux. The low angle bank unfortunately has the poorest resolution and lowest intensity due to the small solid angle and is insufficient for magnetic scattering. The schematic is taken from the HRPD manual on the ISIS website.	66
3.10	The D20 is a two axis medium resolution high flux powder diffractometer. The monochromator is a 111 single Ge crystal. The detector is a position sensitive detector, covering $160^\circ 2\theta$, containing ^3He and propane comprising of 1600 cells, the first and last 32 cells are redundant. The schematic is taken from the D20 manual on the ILL website.	67

3.11	Two plots of the same pattern (a) is the full pattern and (b) highlights at low angle the asymmetry that can result from axial divergence from high resolution X-ray diffractometers. The drop in form factor for X-rays can clearly be seen in (a), though collection to high 2θ provides accurate lattice parameters. The green line represents the model, the red crosses are the individual data points and the purple line is the difference between the model and the data.	77
4.1	increasing temperature improves the size, quality and quantity of hydronium jarosite crystals using 100% H ₂ O as a solvent.	86
4.2	increasing reaction time improves the size of the jarosite crystals and reduction in precursor debris when using 100% H ₂ O as a solvent. The pH falls with increasing reaction time and in these conditions the surface is attacked pitting the surface with triangular holes. The reaction time is a balance to ensure no remaining unknown precursor material is left and good sized well formed crystals - decided to be 21 hours	88
4.3	The SEM images of various H ₂ O/MeOH mixtures at 120°C show how low concentrations of MeOH increase the effective temperature of jarosite formation and produce large single crystals - though an increase in twinning, interpenetrating crystals and stacking faults due to rapid crystal growth possibly centred on the inversion centre. High concentrations eventually leads to unwanted Fe oxy-hydroxy sulphates as shown by the occurrence of Schwertmannite (core-like appearance)	90

4.4	SEM images of various H ₂ O/MeOH mixes between 130-150°C to show how higher concentrations coupled with an increase in temperature causes changes to the crystal growth. At high temperatures with high concentrations of MeOH, mottling of the pseudo cubes occurs to the formation of unwanted Fe oxy-hydroxy sulphates as shown by the occurrence of needle like structures. At lower temperatures high concentrations of MeOH produce interpenetrating triangular prisms, even producing fetching formations shown in the purple tinted picture.	91
4.5	Showing how high methanol concentration combined with high temperatures favours the growth of amorphous iron oxy-hydroxy sulphate phases. Figure (a) shows a slight mottling occurring and the appearance of needle like unwanted phases. Figure (b) shows increasing methanol concentration leaves minimal jarosite formation instead predominately amorphous iron oxy-hydroxy sulphates any remaining jarosite formation is severely mottled. Mottling occurs as a result of the extremely low pH levels present. 90% MeOH concentration levels regardless of temperature fail to produce any Fe oxyhydroxy jarosites instead what appears to be Mikasaite - crystalline iron sulphate - Fe ₂ (SO ₄) ₃	95
4.6	Figure (a) shows the jarosite precursor and the beginning of jarosite formation with the rotation of the SO ₄ ²⁻ unit and the addition of further SO ₄ ²⁻ units and a monovalent cation to ensure jarosite as the product, which results in Figure (b). The plane of the Fe-OH units becomes buckled upon jarosite formation because of the introduction of more sulphate units, octahedrally coordinating with the central Fe ³⁺ ion. This distortion of bond angles will change the exchange pathway between the Fe ³⁺ centres, in turn will affect the resultant magnetic behaviour.	98

4.7	Potassium jarosite (orange) and Szomolnokite (discovered as a white intermediate phase), covering the Fe wire and dispersed among the jarosite precipitate. Use of Pyrex tubes not only allows better temperature gradients, but allows visual inspection. The divisions on the ruler define millimeters	99
4.8	The powder data from the white intermediate (blue pattern) matches the powder taken by Wildner and Giester [2] of Szomolnokite (red pattern) – $\text{Fe}^{2+}\text{SO}_4\cdot\text{H}_2\text{O}$. Both powder diffraction data sets were imported into Fullprof [3] and plotted using WinPLOTR [4].	100
4.9	Structural representation of the jarosite structure. The sulphate groups cap above and below the Fe octahedra sitting along the 3-fold axis. Each of these subunits is separated by the A-site, K^+ in the diagram. (b) Szomolnokite has a more open structure; the distortion from rhombohedral is only slight: $\beta \sim 120^\circ$ and the a and b lattice parameters are similar to the a parameter in jarosite.	101
4.10	Rietveld refinement plot for hydronium jarosite sample 024 taken from the Bruker D8 diffractometer at room temperature. There is a raised background due to the Cu radiation causing the Fe to fluoresce, leaving the data sufficient only to obtain lattice parameters. The purple plot is the difference between the observed data (red) and the model (green). The same setup (refer to subsection 3.8.1) was used for all the other jarosites listed in Tables 4.5 and 4.7.	107
4.11	Spin glass freezing temperature plotted against the synthesis temperature of hydronium jarosites using 100% H_2O as solvent. It shows that synthesis conditions can influence the spin glass transition temperature and how there is a strong correlation between synthesis temperature and T_g	108

- 4.12 T_g plotted against the c parameter of the crystal structure for hydronium jarosites synthesised in 100% H_2O solvent; the samples included are listed in Table 4.5. The graph shows how this change in T_g correlates to a structural change in the c parameter of the unit cell: decreasing T_g corresponds to a more 3D structure as the jarosite structure contracts along the c axis. The red point represents the lowest temperature synthesis of hydronium jarosite ($120^\circ C$) and results in poorly formed jarosite and this point is excluded in the data fit. The change along c occurs primarily in a contraction in the T-A-T sheeting across the 12 coordinate site, where the H_3O^+ unit resides in the A-site position. 110
- 4.13 T_g plotted against the c parameter of the crystal structure for hydronium jarosites synthesised in various concentrations of MeOH/ H_2O solvent at $120^\circ C$. The samples are S9-S16, increasing in MeOH concentration from S9-S16, refer to Table 4.7 for further information. The graph shows that values of T_g correlate to a structural change in the c parameter of the unit cell: decreasing T_g corresponds to a more 3D structure as the jarosite structure contracts along the c axis. The correlation between decreasing values of T_g and the contraction along the c axis also corresponds to an increasing MeOH concentration. The data points shown are sequential in MeOH concentration. The change along c occurs primarily in a contraction in the T-A-T sheeting across the 12 coordinate site, where the H_3O^+ unit resides in the A-site position. 111

- 4.14 T_g plotted against the c parameter of the crystal structure for hydro-
 nium jarosites synthesised in various concentrations of MeOH/H₂O
 solvent at 130°C. The samples are S21-S28, increasing in MeOH con-
 centration from S21-S28, refer to Table 4.7 for further information.
 The graph shows that values of T_g correlate to a structural change
 in the c parameter of the unit cell: decreasing T_g corresponds to
 a more 3D structure as the jarosite structure contracts along the c
 axis. The correlation between decreasing values of T_g and the con-
 traction along the c axis also corresponds to an increasing MeOH
 concentration. The data points shown are sequential in MeOH con-
 centration. The change along c occurs primarily in a contraction in
 the T-A-T sheeting across the 12 coordinate site, where the H₃O⁺
 unit resides in the A-site position. 112
- 4.15 T_g plotted against the c parameter of the crystal structure for hydro-
 nium jarosites synthesised in various concentrations of MeOH/H₂O
 solvent at 140°C. The samples are S30-S35, increasing in MeOH con-
 centration from S30-S35, refer to Table 4.7 for further information.
 The graph shows that values of T_g correlate to a structural change
 in the c parameter of the unit cell: decreasing T_g corresponds to a
 more 3D structure as the jarosite structure contracts along the c
 axis. The correlation between decreasing values of T_g and the contraction
 along the c axis also corresponds to an increasing MeOH concentra-
 tion. The data points shown are sequential in MeOH concentration.
 The change along c occurs primarily in a contraction in the T-A-T
 sheeting across the 12 coordinate site, where the H₃O⁺ unit resides
 in the A-site position. The data set is not as extensive because in-
 creasing MeOH concentration coupled with increasing temperature
 result in the occurrence of unwanted Fe oxy-hydroxy sulphates. . . . 113

- 4.16 T_g plotted against the c parameter of the crystal structure for hydronium jarosites synthesised in various concentrations of MeOH/H₂O solvent at 140°C. The samples are S1-S4, increasing in MeOH concentration from S1-S4, refer to Table 4.7 for further information. The graph shows that values of T_g correlate to a structural change in the c parameter of the unit cell: decreasing T_g corresponds to a more 3D structure as the jarosite structure contracts along the c axis. The correlation between decreasing values of T_g and the contraction along the c axis also corresponds to an increasing MeOH concentration. The data points shown are sequential in MeOH concentration. The change along c occurs primarily in a contraction in the T-A-T sheeting across the 12 coordinate site, where the H₃O⁺ unit resides in the A-site position. The data set is not as extensive because increasing MeOH concentration coupled with increasing temperature result in the occurrence of unwanted Fe oxy-hydroxy sulphates. . . . 114
- 4.17 T_g plotted against the c parameter of the crystal structure for all hydronium jarosites shown in Tables 4.5 and 4.7. It clearly shows a structural change is occurring which causes an overall contraction along c that gives rise to a corresponding decrease in T_g 115
- 4.18 T_g plotted against the a parameter of the crystal structure for hydronium jarosites synthesised at various temperatures using 100% H₂O as the solvent; the samples included are listed in Table 4.5. The graph, unlike for other synthesis series, does not show any correlation between values of T_g and to a structural change in the a parameter of the unit cell. 117

- 4.19 T_g plotted against the a parameter of the crystal structure for hydro-
 nium jarosites synthesised in various concentrations of MeOH/H₂O
 solvent at 120°C. The samples are S9-S16, increasing in MeOH con-
 centration from S9-S16, refer to Table 4.7 for further information.
 The graph shows that values of T_g correlate to a structural change
 in the a parameter of the unit cell: decreasing T_g correlates with
 an expansion along the a axis. The correlation between decreasing
 values of T_g and the expansion along the a axis also corresponds
 to an increasing MeOH concentration. The data points shown are
 sequential in MeOH concentration. 118
- 4.20 T_g plotted against the a parameter of the crystal structure for hydro-
 nium jarosites synthesised in various concentrations of MeOH/H₂O
 solvent at 130°C. The samples are S21-S28, increasing in MeOH con-
 centration from S21-S28, refer to Table 4.7 for further information.
 The graph shows that values of T_g correlate to a structural change
 in the a parameter of the unit cell: decreasing T_g correlates with
 an expansion along the a axis. The correlation between decreasing
 values of T_g and the expansion along the a axis also corresponds
 to an increasing MeOH concentration. The data points shown are
 sequential in MeOH concentration. 119
- 4.21 T_g plotted against the a parameter of the crystal structure for hydro-
 nium jarosites synthesised in various concentrations of MeOH/H₂O
 solvent at 140°C. The samples are S30-S35, increasing in MeOH con-
 centration from S30-S35, refer to Table 4.7 for further information.
 The graph, unlike for other synthesis series, does not show any cor-
 relation between values of T_g and to a structural change in the a
 parameter of the unit cell. 120

4.22	<p>T_g plotted against the a parameter of the crystal structure for hydronium jarosites synthesised in various concentrations of MeOH/H₂O solvent at 150°C. The samples are S1-S4, increasing in MeOH concentration from S1-S4, refer to Table 4.7 for further information. The graph, unlike for other synthesis series, does not show any correlation between values of T_g and to a structural change in the a parameter of the unit cell.</p>	121
4.23	<p>T_g plotted against the c parameter of the crystal structure for all hydronium jarosites shown in Tables 4.5 and 4.7. It shows a structural change is occurring which causes an overall expansion along a that gives rise to a corresponding decrease in T_g. This can only be said to be a trend as the distribution in the a axis widens as T_g decreases.</p>	122
5.1	<p>Pictures showing the experimental setup for sub 2K temperature diffraction studies for the Cr jarosites. Cr jarosite is gently packed into the Al can (Figure 5.1(a)) and the Al can is secured to the bottom of ³He insert (Figure 5.1(b)).</p>	129
A.1	<p>This Figure shows two aspects of diffraction. O is the origin of a volume element, there are two origins separated by a distance r. The difference in diffraction phase angle for the wave vectors \mathbf{k} and \mathbf{k}' are $\mathbf{k} \cdot \mathbf{r}$ and $-\mathbf{k}' \cdot \mathbf{r}$ respectively. The total phase angle difference is $(\mathbf{k} - \mathbf{k}') \cdot \mathbf{r}$. The scattering vector is, $\Delta\mathbf{k}$, defined as $\mathbf{k} + \Delta\mathbf{k} = \mathbf{k}'$. In elastic scattering $\mathbf{k}' = \mathbf{k}$ and for a Bragg reflection to occur, $\Delta\mathbf{k}$ has to coincide with \mathbf{G} ($\Delta\mathbf{k} = \mathbf{G}$) for a particular reciprocal lattice vector and the occurrence is at an angle 2θ, twice the angle from the origin of scattering for wave vector \mathbf{k}.</p>	138

List of Tables

4.1	Synthesis conditions for non-hydronium jarosites using hydrothermal techniques all solutions were made up to 15cm ³ of H ₂ O.	84
4.2	Synthesis conditions for non-hydronium jarosites using the oxidative technique; all reactions were carried at 170°C for 48 hours	89
4.3	Synthesis conditions for deuterated jarosites using either the oxidative technique (Fe wire) or forced hydrolysis (Mikasaite). The mass shown for the Fe wire is the amount averaged between each Pyrex tube.	92
4.5	Table showing the synthesis conditions, lattice parameters and magnetic characterisation for hydronium jarosite samples prepared using 100% H ₂ O as the solvent. S.C. stands for single crystal and shows where the data was taken from - NCS (Southampton) or SRS (Daresbury station 9.8)	104
4.7	Table showing the synthesis conditions, lattice parameters and magnetic characterisation for hydronium jarosite samples prepared using a mix of H ₂ O and MeOH as the solvent. S.C. stands for single crystal and shows where the data was taken from - NCS (Southampton) or SRS (Daresbury station 9.8)	105
4.8	Single crystal data for hydronium jarosite sample No. 24. Data was collected at Southampton university with MoK _α radiation at 85(2)K. Solved using Direct methods and refined using Shelx-97 The space group is $R\bar{3}m$ with a unit cell of $a = b = 7.34940(10)\text{Å}$ and $c = 16.9411(4)\text{Å}$. The R value is 0.0231	123

5.1 Single crystal data for a sample of hydronium chromium jarosite.
Data was collected at Southampton university with MoK α radiation
at 85(2)K. Solved using Direct methods and refined using Shelx-97
The space group is $R\bar{3}m$ with a unit cell of $a = b = 7.2362(6)\text{\AA}$ and
 $c = 16.952(3)\text{\AA}$. The R value is 0.0187 127

Chapter 1

Introduction

1.1 Magnetism and the Jarosites

Jarosites have been utilised throughout the millennia by man and are of great importance albeit jarosites are only humble secondary minerals formed through the weathering of pyrite, FeS. Phoenicians traded argento jarosite as a source of silver. Excavations at the Riotinto site in Southern Spain have showed that, during the Spanish Stone Age I smelting of jarosite bearing earth occurred. The sophistication of the works, considering the time period, is remarkable; to be able to extract the silver from Lead, Arsenic, Antimony and Iron all contained in the rich deposit of jarosites in the Riotinto area. The jarosite name comes from a ravine in Spain called Barranco del Jaroso in the Sierra Almagrera near Almeria where it was first classified as a mineral in 1852 [5].

The importance of jarosite still continues to the present day. It is purposely produced during Zinc purification and refinement process to remove waste deposits [6]. The discovery on Mars of jarosite by the NASA MER-B Rover, suggests that water was once present on Mars, because of high water content present in the jarosite structure [7]. Research into jarosite focuses primarily on the environmental consequences associated with finding its deposits. Jarosite formation comes primarily from the weathering of pyrite, or where there are high concentrations of dissolved Fe^{2+} , Fe^{3+} and SO_4^{2-} ions in water in the presence of a very low $\text{pH} < 2$ and has the general formula $\text{AFe}_3(\text{SO}_4)_2(\text{OH})_6$, ($\text{A} = \text{H}_3\text{O}^+$, NH_4^+ , K^+ , Na^+ , Rb^+ , Ag^+ , $\frac{1}{2}\text{Pb}^{2+}$

Chapter 1. Introduction

or $\frac{1}{2}\text{Tl}^{2+}$) [8]. The jarosite structure is best described in space group $R\bar{3}m$ [9], though spectroscopically mineralogists have been arguing over whether the inversion centre exists for many years [10]. High $\text{Fe}^{2+,3+}$ containing polluted water systems stem from acidic mine tailings leaching into it; along with high concentrations of iron, toxic elements such as Arsenic, Lead and Selenium. These elements may be leached and the jarosite structure has the remarkable ability to uptake them into the crystal structure, only for them to be deposited further afield upon the slow dissolution of jarosite in waters of higher pH.

The topic of magnetism has a long and complicated history with many myths associated with the early discoveries of magnetic materials. The lodestone is the prime example as it is the first material to be discovered to have magnetic properties (bearing in mind everything does have a magnetic response): the attraction of iron objects to the mineral. Lodestone is a magnetised form of magnetite, Fe_3O_4 , through the alignment of the internal magnetic domains to create a net magnetic moment. Magnetite contains a mixture of two Fe^{3+} and one Fe^{2+} ions and the magnetic behaviour displayed by magnetite is intrinsic to its crystal structure and its complexity. The subject of magnetism can only be understood by studying the microscopic level.

William Gilbert wrote, many say the first ever proper scientific text, on the phenomena of magnetism in 1600 [11] and made two very important observations - firstly that the Lodestone has a dipole and was quick to apply this realisation that the Earth most posses a dipole too – explaining why compasses pointed north. Secondly the observation of what is now known as the Curie point, T_C through the heat working of iron. It was observed as the iron was cooled down after being heated to a very high temperature that the metal had become magnetised. Above the Curie point, iron will behave as a paramagnet and will align itself with an external field - usually the Earth's magnetic field - and upon cooling this alignment is retained and the magnetisation increases upon further cooling. The magnetisation of ferromagnet rapidly increases with applied field until a saturation point is reached where the magnetisation either increases weakly or stays constant with increasing applied field. Any increase in magnetisation above the saturation point is the intrinsic magnetisation. The remaining magnetisation when the external field is

Chapter 1. Introduction

removed is the spontaneous magnetisation. Spontaneous magnetisation is inversely proportional to temperature and reduces to zero at the Curie point. For iron metal, $T_C = 1043\text{ K}$

Such phenomena are determined by exchange interactions between the atoms or ions in a material mediated by the chemical bonding of a system; metallic, ionic, covalent or dative, each governing the configuration of the electronic structure. A magnetic moment arises from the combination of the orbital angular momentum and the associated spin of the electron. Ultimately, understanding the finer details of the moment and the interactions with its neighbours are crucial to reveal any electronic ground state.

Ferromagnetism is a widely appreciated phenomena stemming from the exchange interactions dictating that all the magnetic moments, crudely described, align parallel with respect to each other producing a net magnetic moment. Heating above a critical point - the Curie point - will overcome the exchange interactions and allow the moments to have greater degrees of freedom and become essentially independent. The response to an external magnetic field will be to align itself with that field though increasing thermal energy will disrupt and eventually breakdown any magnetic order. Below the Curie point, the exchange interactions will begin to align the moments, even in the absence of a magnetic field. This interaction becomes stronger with decreasing temperature and the system will reach full magnetic saturation at $T=0\text{K}$ - no thermal fluctuations remain to disrupt the magnetic order asides quantum fluctuations. The bulkmagnetisation of a sample below the Curie point will also be further reduced by the creation of domains. Domains are sections of correlated moments but these domains are arranged so as to carve up the magnetism to offset the high energy associated producing a large magnetic field.

Antiferromagnetism, which this project is primarily based upon, similar to ferromagnetism, that an exchange interaction exists to align the magnetic moments, but so as to produce to no net magnetisation. There are many types of ordering of how this can be achieved; a simple ordering type is a head to toe arrangement of the moments, but more complex structures can exit such as helical ordering. The antiferromagnetic transition is from paramagnetic behaviour (independent moments)

Chapter 1. Introduction

to the onset of long range magnetic order is known as the Néel transition - in honour of Louis Néel, the eminent French scientist. The transition is marked by a peak in the magnetic susceptibility.

This project explores exotic phenomena resultant from a new electronic ground state - the *kagomé* spin glass. Spin glass properties have traditionally been thought to be a combination of two components: disorder - site vacancies, doping, distortions or from random exchange interactions and exchange pathways; and magnetic frustration. Frustration is the inability of a system to satisfy the exchange interactions to obtain the lowest energy ground state therefore raising the energy of the ground state. The consequences are far reaching; changing the nature and temperature of critical transitions and forcing the system to explore other ground states. Spin glasses are a good example of how disorder and magnetic frustration transpire to produce a system continually evolving, moving from one ground state to another, on time scales from almost instantaneous to infinity, yet the system always appears frozen. Spin glasses are governed by kinetics and display out-of-equilibrium dynamics, comparable to other systems including; protein folding and neural networks, hence why ideal physical models are very useful to study for far more complex systems. This project looks at the possibility of a spin glass where disorder is negligible or its effects are insignificant, instead the system is highly frustrated. In this case the highly frustrated manifold is a result of the geometric arrangement of the magnetic atoms, leading to spin glass behaviour possibly more exotic than previously studied spin glasses.

Possibly the most studied highly frustrated manifold is the *kagomé* network. It is a 2-dimensional network of vertex sharing triangles. The name *kagomé* derives from a form of Japanese basket weaving bearing this motif as shown in Figure 1.1b). The most investigated physical system containing a highly frustrated magnetic manifold based upon a *kagomé* network is the jarosite crystal structure.

Very recently in the history of jarosite, research has focused on its magnetic properties: the crystal structure was discovered to possess one of the best known examples of a topological array of antiferromagnetically coupled ions that make up the *kagomé* network. The Fe^{3+} ions in the jarosite structure form layers of vertex sharing triangles making up the *kagomé* network as shown in Figure 1.1b). The

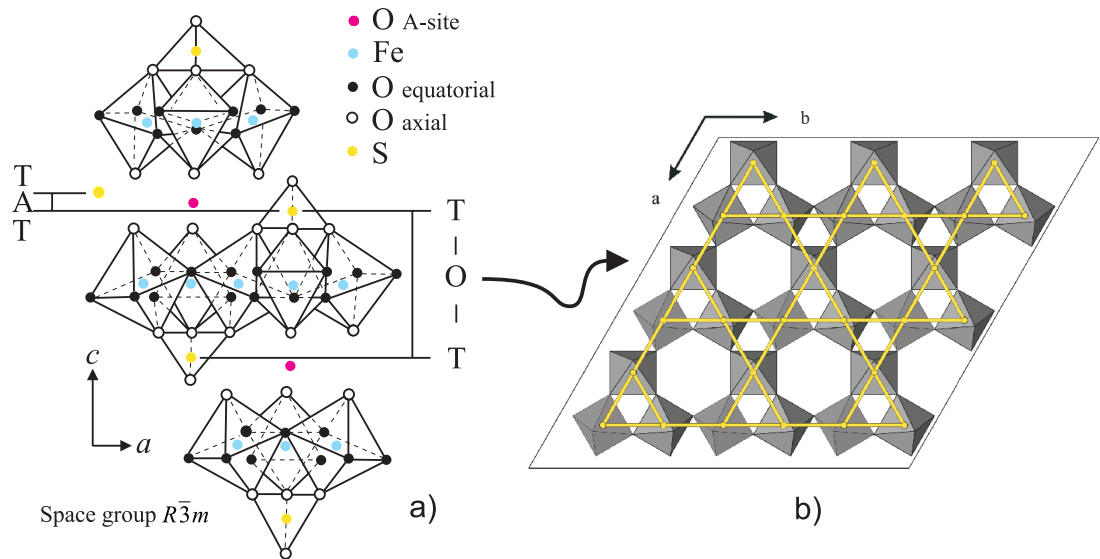


Figure 1.1: a) Polyhedral representation of hydronium jarosite, the O from the H_3O^+ is shown in red representing the A-site. The bridging hydroxyl groups shown in black, which are just above and below the *kagomé* plane, lead to form a canted Fe-coordinated octahedra. This canting has important consequences for the magnetism of the jarosite structure. b) a view along the *c* axis showing the canted Fe octahedra and the *kagomé* network overlaid to show the arrangement of the Fe^{3+} ions.

Fe^{3+} ions are bridged together by hydroxyl groups situated slightly above and below the *kagomé* plane. The bridging hydroxyl groups mediate the magnetic exchange between the Fe^{3+} ions to produce an antiferromagnetic exchange between the ions. The Fe-oxygen coordinated octahedra are capped above and below by tetrahedrally coordinated sulphate groups to form the T-O-T sheets shown in Figure 1.1a). Separating each of these T-O-T layers is the 12 coordinate site where the A-site ions reside - making the T-A-T sheet (Figure 1.1a). The *kagomé* layers of Fe^{3+} ions are therefore sufficiently separated that the magnetic system is essentially 2-dimensional.

This project focusses primarily on the presence of anisotropy and how that can bring about a critical phase transition at finite temperature in *kagomé* systems based upon Heisenberg and Ising systems: within the classical limit and on the Quantum limit.

The model *kagomé* system used are iron jarosites, Heisenberg $S=\frac{5}{2}$ and chromium

Chapter 1. Introduction

jarosites with possible Ising like behaviour $S=\frac{3}{2}$. The phase transitions displayed by varying the A-site ion or incremental changes in synthesis conditions can determine the nature of that transition and control the temperature of a transition.

Chapter 2

Theory

2.0.1 Magnetic Interactions

2.1 Curie-Weiss Law

2.1.1 Curie Law

Induced magnetic flux, \mathbf{B} , will cause moments to align parallel with the flux and the field strength, \mathbf{H} , and in free space the simple relationship in CGS units is $\mathbf{B} = \mathbf{M}$; permeability of free space in CGS is unity. The effect of \mathbf{B} upon a sample induces a magnetisation, \mathbf{M} , in linear samples \mathbf{M} is proportional to \mathbf{H} shown simply as $\mathbf{M} = \chi\mathbf{H}$.

Susceptibility, χ , is a dimensionless fundamental parameter to describe the magnetisation or magnetic state induced by an applied field within a sample with a linear response. In the paramagnetic region the susceptibility is described simply by the Curie law (2.1) where the susceptibility is inversely proportional to temperature.

$$\chi = C/T \tag{2.1}$$

2.1.2 Derivation of the Curie constant

The derivation of the Curie constant is useful to understand the intrinsic nature of susceptibility and the difference between transition metals and rare earth metals. μ_{eff} (2.2) is the effective magnetic moment experienced by every paramagnetic ion within an applied field.

$$\mu_{eff} = (3k_B/N)^{\frac{1}{2}}(\chi T)^{\frac{1}{2}} \quad (2.2a)$$

$$= [g^2 s(s+1)]^{\frac{1}{2}} \mu_B \quad (2.2b)$$

$$\mu_B = \frac{e\hbar}{2m_e c} = 2.9732 \times 10^{-21} \text{erg Oe}^{-1} \quad (2.2c)$$

where $g=2.0023$ is the Landé g -factor derived in (2.3)

$$g = \frac{3}{2} + \frac{S(S+1) - L(L+1)}{2J(J+1)} \quad (2.3)$$

where S , L , and J are the total spin, total orbital angular momentum and total angular momentum quantum numbers respectively. The magnetic moment per individual atom or moment is, $\mu = -g\mu_B J$ and the difference between each micro state, the degeneracy is resolved in a magnetic field, is $E = -\mu \mathbf{B} = M_J g \mu_B \mathbf{B}$. The energy levels are separated by a factor of gM_J , M_J is the projection of J . In the case of $L=0$, $E = \pm \mu_B \mathbf{B}$ for a single spin there are two populations levels split $M_J = \frac{1}{2}, \mu = -1$ and $M_J = -\frac{1}{2}, \mu = 1$ set out in (2.4).

$$\begin{aligned} \frac{N_1}{N} &= \frac{e^{\mu \mathbf{B}/k_B T}}{e^{\mu \mathbf{B}/k_B T} + e^{-\mu \mathbf{B}/k_B T}} \\ \frac{N_2}{N} &= \frac{e^{-\mu \mathbf{B}/k_B T}}{e^{\mu \mathbf{B}/k_B T} + e^{-\mu \mathbf{B}/k_B T}} \end{aligned} \quad (2.4)$$

N_1 and N_2 are the populations of the two levels, the total N is the number of atoms

Chapter 2. Theory

or ions. The resultant magnetisation for N is

$$\begin{aligned}
 \mathbf{M} &= (N_1 - N_2)\mu \\
 &= N\mu \frac{e^{\mu\mathbf{B}/k_{\text{B}}T} - e^{-\mu\mathbf{B}/k_{\text{B}}T}}{e^{\mu\mathbf{B}/k_{\text{B}}T} + e^{-\mu\mathbf{B}/k_{\text{B}}T}} \\
 &= N\mu \tanh(\mu\mathbf{B}/k_{\text{B}}T)
 \end{aligned} \tag{2.5}$$

This can lead to the approximate identity $M \cong N\mu(\mu\mathbf{B}/k_{\text{B}}T)$ when $\mu\mathbf{B}/k_{\text{B}}T < 1$, $\tanh(\mu\mathbf{B}/k_{\text{B}}T) \cong \mu\mathbf{B}/k_{\text{B}}T$. M_J will have $(2J + 1)$ energy levels which will be resolved equally in the presence of \mathbf{H} leading the magnetisation shown in (2.6).

$$\begin{aligned}
 \mathbf{M} &= NgJ\mu_{\text{B}}B_J(x) \\
 x &\equiv gJ\mu_{\text{B}}\mathbf{B}/k_{\text{B}}T
 \end{aligned} \tag{2.6}$$

x is the Zeeman energy and B_J is the Brillouin function (2.7)

$$\begin{aligned}
 B_J(x) &= \frac{2J+1}{2J} \coth\left(\frac{2J+1}{2J}x\right) - \frac{1}{2J} \coth\left(\frac{x}{2J}\right) \\
 J = \frac{1}{2}, x < 1, \coth x &= \frac{1}{x} + \frac{x}{3} - \frac{x^3}{45} + \dots
 \end{aligned} \tag{2.7}$$

This result leads back to the susceptibility (2.8)

$$\frac{\mathbf{M}}{\mathbf{B}} \cong \frac{NJ(J+1)g^2\mu_{\text{B}}^2}{3k_{\text{B}}T} = \frac{\mathbf{C}}{T} = \chi \tag{2.8}$$

The Curie constant rewritten, traditionally used by inorganic chemists is shown in (2.9a). The susceptibility, χ , gives a direct measure of the effective moment (2.9b).

$$\mathbf{C} = \frac{N\mu_{\text{eff}}^2}{3k_{\text{B}}} \tag{2.9a}$$

$$\mu_{\text{eff}}^2 = g^2J(J+1)\mu_{\text{B}}^2 \tag{2.9b}$$

The rare earths show a good relationship between expected and observed for total angular momentum., unlike the transition metal ions which show only a good relationship with spin only - $g[S(S+1)]^{\frac{1}{2}}$. The differences arise because the 3d orbitals, unlike the 4f orbitals, are the outermost and therefore experiences crystal

field splitting, resulting in $L = 0$ and quenching the orbital contribution. The magnetic interaction for 3d ions is purely spin-spin coupling, unlike f orbitals which are non-bonding. Anisotropy can be present which can induce a slight spin orbit coupling even in Fe^{3+} , $L = 0$ or detected from Mössbauer experiments and Electron Paramagnetic Resonance (EPR) that very small spin-orbit coupling can exist [12–14].

2.1.3 The Weiss Model

A ferromagnet is characterised by the presence of spontaneous magnetisation in the absence of \mathbf{B} : this occurs at a temperature known as the Curie temperature, T_C . Above T_C the spontaneous magnetisation disappears and paramagnetic behaviour exists. $T \leq T_C$. Here the symmetry is broken and all the moments align themselves parallel with each other, in a chosen direction. This would suggest an internal field or exchange which allows each spin to feel the average spin of all other spins in the mean field approximation. Each spin will experience a field proportional to the magnetisation (2.10).

$$\mathbf{B}_E = \lambda \mathbf{M} \quad (2.10)$$

λ represents the strength of the effective field. The Weiss model of magnetism describes the situation where below T_C the magnetic order is self sustaining and as the temperature is increased so thermal fluctuations will destroy this order and eventually at the critical temperature, T_C thermal fluctuations destroy the order. The occurrence of the spontaneous magnetisation can be seen with comparison to the Brillouin function. Incorporating equation (2.10) into equation (2.6) results in $x = gJ\mu_B(\mathbf{B} + \lambda\mathbf{M})/k_B T$. In the absence of a magnetic field $\mathbf{B} = 0$, $\mathbf{M} = k_B T x / g\mu_B J \lambda$. In the case of $T > T_C$ then the gradient of \mathbf{M} against x is steeper than the Brillouin function and thus no spontaneous magnetisation. When $T > T_C$ then initial gradient of the Brillouin is steeper.

2.1.4 Magnetic Order

2.2 Frustration

Frustration is an intrinsic component for spin glasses, though frustration can occur in many magnetic examples without leading to spin glass behaviour. Frustration is the inability of the system to reach its lowest ground state energy, usually caused by competing interactions [15] preventing the satisfaction of pairwise interactions. The competing interactions arise either out of differing exchange pathways or the geometry of the system.

The systems inability to reach a ground state raises the ground state energy and can produce unexpected properties. Research into frustrated systems began in earnest with the intense interest in spin glasses during the 1950s and 1960s. Frustration as a topic was reinvigorated after the discovery of the High Temperature Superconductors (HTS) which the saw the current BCS theory (Bardeen, Cooper, and Schrieffer) on superconductivity inadequately fail for many reasons, but primarily the band gap in the cuprates is greater than 50 meV and is beyond any phonon contribution [16]. P. W. Anderson suggested underlying the electronic ground state of the new HTS was frustration and that the ground state is similar to antiferromagnetically coupled ions arranged to form a triangular lattice [17]. The early 1990s witnessed an explosion in publications concerning magnetic frustration, many centered on geometric arrangements of moments to produce frustration.

There are many ways to introduce competing interactions. A mix of antiferromagnetic and ferromagnetic interactions spread randomly throughout a lattice, where not all the interactions between neighbours can be all minimized. The spin glass phenomena was originally found in doped metal alloys; AuFe and CuMn where small quantities of Fe or Mn can produce the spin glass phenomenon. At small levels of doping Fe distances would be too great to interact with each other and instead effects such as the Kondo effect [18] or weak moments, or the opposite effect, giant moments. It is only when the long range effects (20-30 Å) of the RKKY [19] (Ruderman, Kittel, Kasuya and Yosida) interaction become involved that competition between moments occur. The Kondo effect, giant moment and the RKKY interaction are discussed in the section spin glasses, however, de-

Chapter 2. Theory

pending on the distance between impurity moments the oscillatory nature of the RKKY will change between antiferromagnetic coupling and ferromagnet coupling giving rise to competing interactions. As the doping increases so the proximity of the impurities will be closer and shorter range interactions will begin to dominate. In non-metallic bonded compounds, rather than metal alloys, where spin glass behaviour is observed, it is the bonds between the atoms that will dictate the magnetic interactions. Here the level of magnetic frustration can be considerably increased.

2.2.1 Bond Frustration

The framework of the lattice and the nature and strength of the constituent bonds can lead to frustration. Disparity in the strength of the coupling between magnetic sites can lead to competition and the generation of degeneracy of ground states. A simple example of frustration can be shown on a square lattice with differing antiferromagnetic interactions.

Simple Square plaquette

The Mattis Model

Vortices

2.2.2 Geometric Frustration

Antiferromagnetically coupled ions arranged upon a single triangle can not minimise their exchange interactions (Figure 2.1a) and a compromise is reached where the moments align themselves 120° from one another forming two distinct chiral forms (Figure 2.1 b). This is an example of highly frustrated magnetism purely as a result of the underlying geometry leading to a ground state degeneracy of two for a single triangle.

Triangular Lattice

How the triangles are tessellated will dictate the scope of the degeneracy for a macroscopic system. Tiling the triangles by edge sharing will not further change

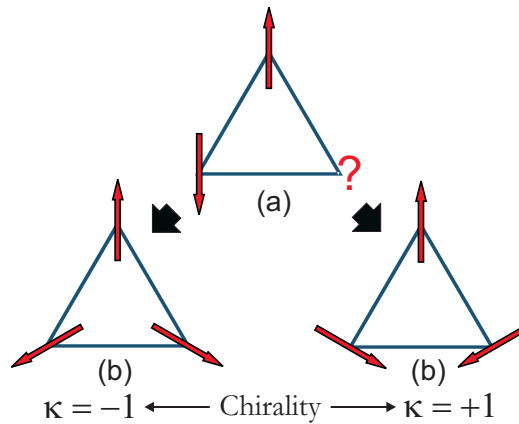


Figure 2.1: a) the system’s inability to simultaneously minimise all the exchange interactions leads to frustration as shown by the third spin. b) shows two distinct compromise arrangements where the moments are orient 120° from each other. This introduces the concept of chirality into the system

the degeneracy with size as Figure 2.2 shows. The chirality of the central red triangle dictates the spin configuration of the neighbouring triangles because two of the three moments that make up a neighbouring triangle are from the central red triangle. This leads to a coherent propagation of one chirality throughout the lattice therefore the system retains a degeneracy of two.

Kagomé Lattice

Tessellating the triangles by their edges ensure that only one moment upon a triangle is determined by its neighbour and therefore not able to determine the spin orientation of its closest neighbour. This is exemplified in Figure 2.3; one central chiral form does not dictate the spin configuration of an adjacent triangular plaquette and this can lead to a degeneracy that scales with size producing a macroscopically degenerate system.

The vertex connectivity of this lattice allows the system to explore ground states through other ground states whilst maintaining the 120° configuration for a ground state. These involve the collective spin reorientation of two sublattices, the axis of the reorientation defined by a third sublattice. In the absence of any energy barriers there will be a fluid movement of spins and this fluid movement will

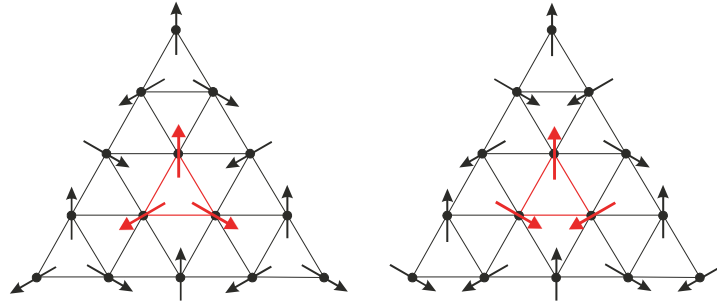


Figure 2.2: The two diagrams show two red triangles at the centre of an edge sharing lattice of triangles with moments placed at the vertex of each triangle. The red triangles represent the two different chiral forms of antiferromagnetically coupled ions, each moment aligned 120° from each other. Maintaining the 120° alignment the chiral form of the red central triangle propagates coherently throughout the structure because each triangle shares two moments with its nearest neighbours, therefore dictating the alignment of the third moment upon a triangle. The degeneracy therefore does not scale with size and remains with a double degeneracy.

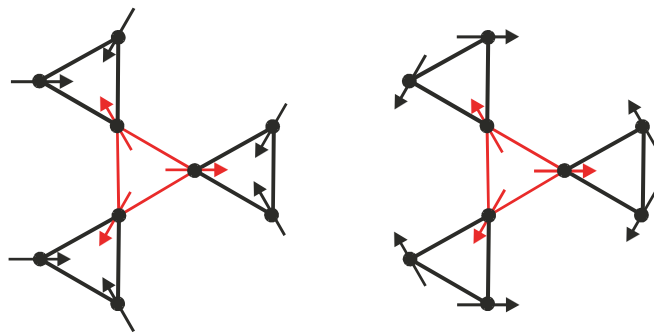


Figure 2.3: The two diagrams show two red triangles with the same chirality at the centre of a vertex sharing lattice of triangles with moments placed at the vertex of each triangle. The red triangles are both the same chiral form of antiferromagnetically coupled ions, each moment aligned 120° from each other. Maintaining the 120° alignment the chiral form of the red central triangle does not determine the spin configuration of the neighbouring triangular plaquette and as shown either chiral form can be present. For one central chiral form with three nearest neighbours a ground state degeneracy of six can be achieved. This degeneracy scales with the size of the system ultimately producing a macroscopically degenerate ground state.

continue all the way down to $T = 0$ K. Any energy barrier arising from anisotropy, magnetic site disorder, randomness or defects will ensure the fluid movement will cease at a finite temperature.

Chirality

Spin Folds

2.3 An Introduction to Mean Field Theory

Phase transitions are an integral part of nature and characterize one form of matter from another. The more obvious and common phase transitions are from liquid to gas or the melting of a solid. What characterizes the phases transition in these situations is symmetry breaking. Imagine the solid phase as a regularly periodic arranged crystal. The number of symmetry operations will be limited, dependant upon the smallest repeatable periodic arrangement - the unit cell- but, immaterial for this example, because the translational symmetry is very restricted. The crystal structure is essentially fixed and only transitionally invariant from a combination of a limited number of lattice basis vectors.

Upon melting to a liquid the regular arrangement of atoms will breakdown giving rise to a system where the translational symmetry of the atoms is almost unrestricted, the only restraint coming from the short range interactions that restricts the liquid to a given volume. A liquid will, similar to a perfect sphere have full rotational symmetry. A transition from a liquid phase to a gas phase, only a second order transition, will remove the restraint of a finite volume hence further increasing the translational symmetry. An order parameter is used to describe the nature of an associated phase change. For the states of matter involving liquids, gases and solids this is characterized by enthalpy.

For a ferromagnet the order parameter will be the magnetisation. Similar for a solid-liquid transition, the moments in a uniaxial ferromagnet will possess full rotational and translational symmetry above the Curie point, T_C . Below T_C the moments will align in one direction. This demonstrates once again the symmetry breaking involved as a particular direction is chosen to align all the moments. The ground state chosen does not possess the symmetry of the underlying Hamiltonian

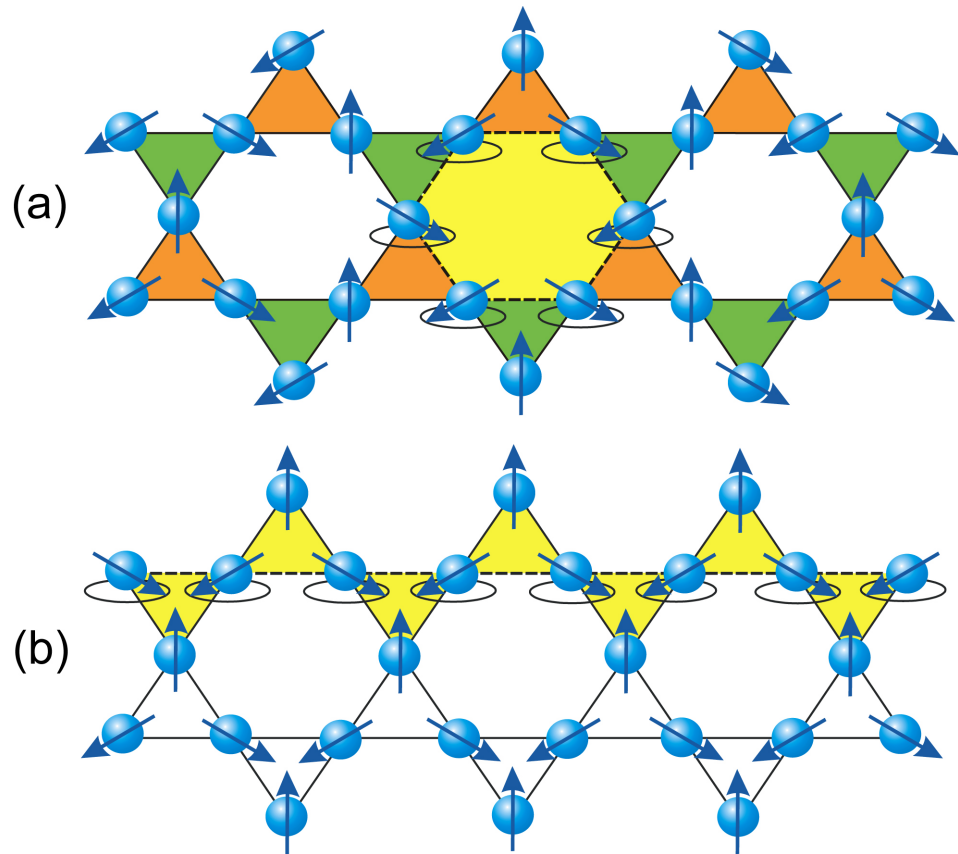


Figure 2.4: The different chiralities and spin folds possible for the kagom anti-ferromagnet. The orange and green triangles have the $\kappa = +1$ and the $\kappa = -1$ chiralities respectively. Zero energy excitations termed ‘spin folds’ (highlighted in yellow) can occur within structures with both uniform and staggered chiralities: a) shows an ‘open spin fold’, which traverses a lattice if based upon the uniform chirality (the $\mathbf{q} = 0$ structure); b) shows a ‘closed spin fold’ based upon a lattice with staggered chirality (the $\sqrt{3} \times \sqrt{3}$ structure).

and in this instance the system is in a metastable state. The moments could choose to line up in the opposite direction, to reverse all the moments simultaneously is an extremely unlikely event. The metastable state of a ferromagnet has a stability time longer than the age of the universe. Though smaller, simpler systems, with smaller energy barriers will oscillate between metastable states as in the case of an ammonia molecule oscillating between two stereo conformations arising from the presence of a lone pair of electrons. The pyramidal structure will invert between the two conformations at a particular frequency. That frequency is the energy difference between the ground state and the first excited state. The ground state, in this case, is a superposition of the energy eigenstates represented by the two metastable states.

2.3.1 Symmetry Breaking

2.3.2 Ginzburg-Landau theory

2.3.3 Two Dimensional Ising model

2.3.4 XY-Model

2.3.5 Heisenberg

2.4 Spin Glasses

Spin glasses are a state of matter which exists with both broken symmetry and broken ergodicity in the limit $N \rightarrow \infty$. This makes it an exotic state of matter when compared to a ferromagnet, which upon being cooled to T_C undergoes spontaneous symmetry breaking by selecting a particular direction for the configuration of the moments in the limit $N \rightarrow \infty$: this system will not explore configurations in the opposing direction. In the case of a spin glass, the system will continue to evolve below the transition temperature evidenced with a continually reducing remnant magnetisation changing from either a very short period of time, but not spontaneous, up to millennia.

The broken ergodicity for a spin glass is complicated, there are many different

Chapter 2. Theory

states for the system to exist in and unlike a system in thermal equilibrium where the properties will be an average of the entire system, for a spin glass the properties reflect the current stable state the system is in. This many stable state system is best envisaged as a set of valleys, each with its own local minima and the system traverses from one ground state to another by moving along these valley boundaries.

What gives rise to the broken ergodicity are competing interactions, leading to frustration in trying to satisfy the pairwise interactions, even as far as next nearest neighbours, and the system's inability to reach the lowest ground state energy. Frustration is explained in detail in the section frustration. Though it has always been conceived that frustration is a prerequisite, disorder or randomness is integral too for spin glasses. Mydosh expresses that without randomness, either site or bond, then a spin glass transition will not be achieved, but instead a slow blocking to a ground state where large magnetic fluctuation dominates. In particular Mydosh references the example of the *kagomé* antiferromagnet as not displaying spin glass like behaviour. Albeit, this thesis will primarily support the presence of spin glass behaviour in a highly frustrated manifold such as the *kagomé* antiferromagnet and give an explanation for its occurrence without intrinsic disorder: prior an appraisal of current spin glass theory is needed.

2.4.1 Physical Properties of a Conventional Spin Glass

Spin glasses are systems with multiple degenerate ground states created by the frustration. The system can evolve from one ground state to another, possibly at $T = 0$, below T_g .

Variations of T_g with applied field

2.4.2 Interactions within a Spin Glass

RKKY

Randomness

Magnetic Anisotropy

2.5 The *Kagomé* Spin Glass

2.5.1 Physical Properties of the *Kagomé* Spin Glass

Variations of T_g with applied field

2.5.2 Anisotropy

Dzyalonshtinsky-Moriya Interaction

XY Anisotropy

Easy Axis Anisotropy

2.6 Topology

2.6.1 Introduction to Homotopy and Theory of Defects

2.6.2 *Kagomé* Network and Triangular Networks

Chirality Revisited and Spin Folds

2.6.3 Solitons - Implications for the *Kagomé* Antiferromagnet

2.7 Overview of Current Research into Frustrated Magnetism

Chapter 3

Experimental Methods

This chapter involves many techniques; the synthesis and quantification of the samples made; crystallography to determine the crystal and magnetic structures and magnetic characterisation.

3.1 Chemistry and Synthesis of Fe and Cr jarosites

Jarosites have always been synthesised from varying concentrations of the iron and required A-site sulphate solution at or below 100°C to replicate industrial processes [6]. The need to try to achieve near 100% occupation became important with the realisation of the frustrated magnetic properties and exploration of hydrothermal methods developed [20,21].

The techniques required to produce high quality Fe jarosite are explored in this chapter utilizing hydrothermal techniques. This was then expanded upon to synthesize Cr jarosites which require more extreme conditions [22].

3.2 Hydrothermal Synthesis of Fe jarosites

Hydronium jarosite can only be readily synthesised under hydrothermal conditions [8]. The need to increase Fe occupation and determine why hydronium jarosite was magnetically different has led to several hydrothermal methods based upon super critical water heated under pressure. Therefore the need to produce jarosites using

Chapter 3. Experimental Methods

hydrothermal techniques - reactions carried out using super critical H₂O.

3.2.1 Forced hydrolysis

All forced hydrolysis hydrothermal synthesis used Pyrex pressure tubes and a fixed concentration of 0.55M Fe³⁺ based upon synthesis of hydronium jarosite by Earle *et al* [21]. Earle *et al* introduced a new approach to forced hydrolysis for the synthesis of hydronium jarosite with the mixing of MeOH and H₂O as a solvent. The ideal ratio for the solvent mix was found to be a 50/50 ratio of MeOH:H₂O. The best conditions for hydronium jarosite synthesis using a 50/50 MeOH:H₂O solvent mix was a 15cm³ solution of 0.275M Fe₂(SO₄)₃.5H₂O (0.55M Fe³⁺) heated at 120°C for 3 days using a Parr autoclave with a PTFE liner. Earle *et al* claimed that Thermo-gravimetric analyser (TGA) data of the resultant jarosite produced an Fe³⁺ vacancy of less than 2%. In conjunction with the benefits of the Pyrex tubes and extending the Earle *et al* [21] method, a wide range of hydronium jarosites were synthesised.

Each hydronium jarosite sample was synthesised using a modified method outlined by Earle *et al* [21]: 0.275M Fe₂(SO₄)₃.5H₂O (0.55M Fe³⁺) were made up to 15cm³ solutions with a solvent mix ranging from 100% H₂O to 90/10 MeOH:H₂O and added into a 23cm³ Pyrex pressure tubes. The reactions were heated at temperatures ranging from 120-150°C for 21hours. The jarosite precipitate was washed several times with distilled water and the water decanted off each time and the sample dried in an oven between 110-120°C for a minimum of 4 hours. Yields ranged from 0.2g to 0.8g. Increasing temperature or MeOH concentration produced greater yields. There is a limit that can be used for temperature and MeOH concentration. The maximum working temperature for synthesis using 100% H₂O or H₂O/MeOH mix as a solvent is 150°C, above that temperature haematite forms, but the combination of increasing temperature and MeOH concentration can produce amorphous or unwanted iron oxy-hydroxy sulphates below 150°C. Hydronium jarosites synthesised using this method each had a distinguishable and different magnetic transition temperature. In addition, the use of MeOH and Pyrex tubes produced greater yields and in many cases large enough single crystals for single crystal X-ray diffraction.

Chapter 3. Experimental Methods

Similarly non-hydronium jarosites were synthesised using 0.55M Fe³⁺ 15cm³ solutions (100% H₂O solvent) using Pyrex tubes with a corresponding A-site sulphate or hydroxide dissolved in the 0.55M Fe³⁺ solution.

Pyrex Pressure tubes

Pyrex pressure tubes were used, as an alternative to PTFE lined steel bombs, manufactured by Ace Glass Inc., including a PTFE screw top (Ace Glass # 15) with a front mounted O-ring seal, refer to Figure 3.1 detailing the Pyrex pressure tubes. The original O-ring was replaced by a Viton O-ring (Figure 3.1(c)) which can withstand continued high temperature reactions and has a far greater resistance to super-critical water and low pH conditions. Viton can withstand temperatures of up to 250°C, which surpasses the Pyrex pressure tubes, and can thus sustain long reaction times up to 170°C and shorter periods to 180°C, before serious deformation of the PTFE screw top thread occurs - Figure 3.1(b) shows the #15 screw thread. The capacity of the tubes used was either 23cm³ or 38cm³ filled with 15cm³ or 25cm³ of solution respectively, giving a filling volume of ~66%. The benefits of Pyrex tubes for jarosite synthesis over PTFE lined autoclaves are; firstly, a better temperature gradient through the reaction vessel; secondly, it allows visual inspection of the reaction; thirdly, it gives a far better surface for jarosite crystal growth and finally it allows for a rapid turnaround and mass production of jarosite synthesis.

3.2.2 Oxidative Hydrothermal Synthesis

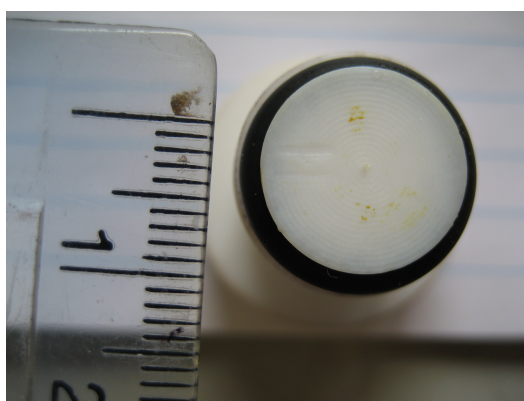
A new hydrothermal oxidative process, similar to that used for zeolite synthesis [23] claims to achieve 100% Fe coverage [24,25] and greater crystal size (<50µm across a face). This improvement to crystal quality has enabled greater insight into the crystal structure and magnetic characteristics. The drawback is that hydronium jarosite, arguably the most important jarosite for magnetism, cannot be synthesised via this method. This suggests there are at least two different reaction mechanisms for jarosite formation.

Syntheses of potassium jarosite were undertaken by implementing a modified version of the literature method by Grohol *et al.* The method used 38cm³ capacity

Chapter 3. Experimental Methods



(a) An Ace Glass Pyrex tube (size #15) with (b) Ace Glass #15 PTFE screw top showing the a front mounted O-ring seal positioned at the thread. This was the only size used, though end of the PTFE screw top. Jarosite formation the thread itself was prone to deformation and that grew up the side of the Pyrex tube near replacement PTFE screw tops had to be made. to the PTFE screw top can be seen.



(c) Ace Glass #15 PTFE screw top showing the front mounted Viton O-ring at the end of the PTFE screw top.

Figure 3.1: The Pyrex tubes from Ace Glass Inc., provided an excellent reaction for hydrothermal synthesis. There are many advantages of using Pyrex pressure tubes over conventional bombs: firstly, a better temperature gradient through the reaction vessel; secondly, it allows visual inspection of the reaction; thirdly, it gives a far better surface for jarosite crystal growth and finally it allows for a rapid turnaround and mass production of jarosite synthesis. The positioning of the Pyrex tube at an angle of deviation from upright of approximately 35° was found to provide the best angle for crystal growth up the Pyrex tube. The divisions on the ruler show millimeters.

Chapter 3. Experimental Methods

Pyrex pressure tubes (Ace Glass Inc) with PTFE screw tops with a Viton O-ring seated inside the tube. 0.33g (tolerance of up to +0.05g) of Fe wire cut into 4-6 pieces (2mm diameter, 99.9% purity) and 2.44g of K_2SO_4 were added to 25ml of H_2O (0.56M solution) and 1.1ml of H_2SO_4 was further added, giving a filling of 66%. The reaction was heated at 170°C for 48 hours. The addition of the H_2SO_4 reduces the pH to < 1 . A very acidic environment is needed as usual in jarosite formation but exceptionally low pHs are required for the oxidative method to oxidise the Fe wire. There is a tolerance for mass of the iron wire used because of the thickness of the wire and the precision obtained having to use wire cutters. Pyrex pressure tube allows visual inspection of the reaction (Figure 4.7) and better control of the hydrothermal conditions which is not possible with a PTFE lined steel bomb.

This method was then extended for other iron jarosites, including: sodium jarosite, silver jarosite, ammonium jarosite and rubidium jarosite. Non-potassium jarosites are harder to synthesize and therefore the reaction has a greater sensitivity to the reaction conditions, often producing hematite as a result or failure of the iron wire to oxidise.

A summary of reaction conditions for the above listed jarosites synthesised using the hydrothermal oxidative method are shown in Table 4.2 in the experimental Fe results section.

3.2.3 Forced hydrolysis and oxidative synthesis of deuterated jarosites

Large quantities of homogenous samples are required for neutron scattering experiments. Having discovered that Mikasaite (4.1.3) is a likely intermediate for the hydrothermal forced hydrolysis reactions of hydronium jarosite (refer to subsection - Mechanism for Jarosite formation ??) and the requirement for a very high percentage of D, it was best to proceed with high concentration of dehydrated $Fe_2(SO_4)_3$ (Mikasaite). The reaction conditions for the Mikasaite based preparations were in keeping with the modified method of Earle *et al* [?], using 2g of $Fe_2(SO_4)_3$ (Mikasaite) per 15ml of solution. The molar concentration of Fe^{3+} ions is increased to 0.67M because Mikasaite is anhydrous. Details of the reactions are laid out in

Chapter 3. Experimental Methods

Table 4.3.

Deuterated sample preparation using the oxidative method were followed as before for this method, but with the substitution of D₂O for H₂O and the relevant concentration of D₂SO₄ (1.1cm³ added per 25cm³ solution) was added instead of H₂SO₄.

3.3 Chemistry and Synthesis of Cr jarosites

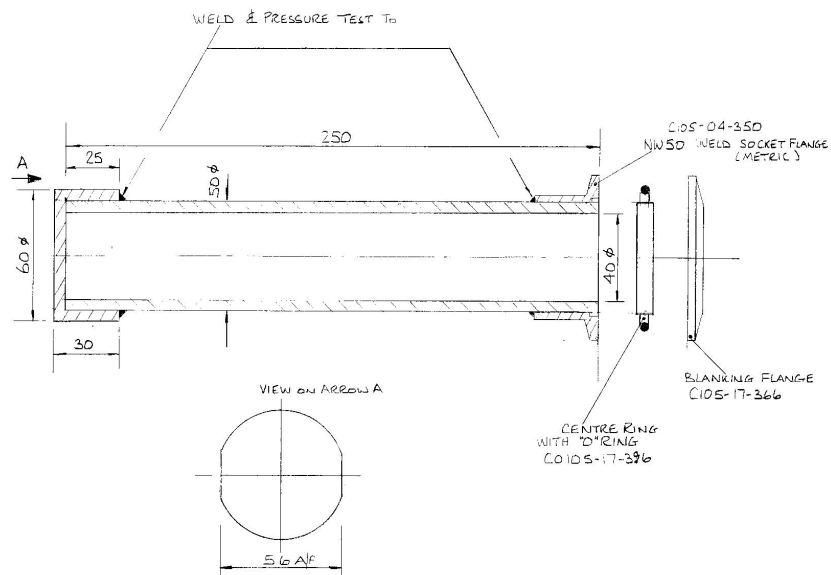
Synthesis of Cr jarosites require even more extreme conditions [22,26] than for the synthesis of Fe jarosites and Pyrex tubes were not able to used in the preparation because greater temperatures are required. Nor could PTFE lined bombs be used as the temperatures required were near to and or above the melting point of PTFE.

3.3.1 Hydrothermal Methods

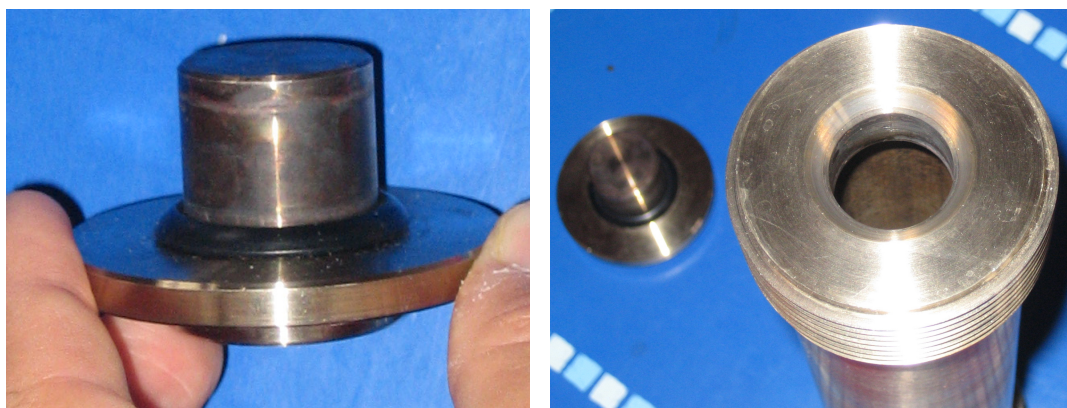
A new bomb was designed to allow experimentation up to 300°C, refer to Figure ??.

Solutions were made up to 15ml of D₂O containing 2.06g (0.35M) Cr₂(SO₄)₃.xD₂O and either 0.78g (0.3M) K₂SO₄, 0.64g (0.3M) Na₂SO₄ or 1.40g (0.3M) Ag₂SO₄ encased in a Pyrex tube (made from 14mm diameter, 1.5-2mm thickness, Pyrex tubing by glass blowing in an acetylene flame). The tube was placed inside the bomb with 15ml of water to balance the pressure on the Pyrex tube and placed in an oven for 48 hours at 230°C. Deuterated Cr jarosite was synthesised with 1.65g (0.3M) Cr₂(SO₄)₃.xD₂O dissolved in 15ml of D₂O and heated for 24 hours at 265°C. The samples were retrieved and washed several times with D₂O and placed in a drying oven 110°C for a minimum of 4 hours.

Chapter 3. Experimental Methods



(a) A schematic showing the original design for the bomb by Mike Sheehy. It is made from steel tubing with a cap welded at the bottom. The original flange at the top was removed and another flange with a narrow opening (Figure 3.2(c)) with a cut screw thread on the outside was welded in place. A steel plug (Figure 3.2(b)) then fits into a narrow gap with a back mounted O-ring and is secured by hand tightening using a heavy duty screw threaded cap.



(b) The steel plug shown with back mounted O-ring. The specialist O-rings that can withstand water temperatures up to 300°C.

(c) Both the plug and the narrow gap for the plug to secure. Inside the gap there is a beveled edge to allow the Pyrex tube to slip out when turned up side down.

Figure 3.2: Bomb design for Cr jarosite synthesis. Temperatures reaching 300°C are needed for Cr jarosite synthesis and the need for a heavy duty bomb made from stainless steel. A Pyrex tube, fashioned by glass blowing which contains the reactants, is slipped into the bomb and 15cm³ of water added to equalize the pressure upon the Pyrex tube. A stainless steel plug (Figure 3.2(b)) with back fitted O-ring fits neatly into gap and is secured using another cap.

3.4 Inductively Coupled Plasma Elemental Analysis Techniques

3.4.1 Introduction to Inductively Coupled Plasma

The use of Inductively Coupled Plasma (ICP) as a technique to provide elemental analysis was developed through research into uranium. There are two methods of elemental analysis using ICP, the first is to producing ions from the sample to be analysed and pass them through a mass spectrometer (MS), the other records the atomic emission spectra (AES). Both have their advantages; ICP-MS is very sensitive and is useful to measure trace elements within a sample and has an error of about 10%, however the concentrations measured are in ppb. ICP-AES is more useful for bulk elemental analysis and gives a very low error of about 0.1% but concentrations are measured in ppm. Only ICP-AES was used to analyse jarosite samples.

The plasma is generated by the induction of an electric current of a radio frequency to argon gas passing through a copper coil. This produces ionisation and a breakdown leading to the formation of a plasma, reaching temperatures of 10 000K at the core. The temperatures inside a plasma of argon are sufficient to ionise most elements that are introduced into the plasma for elemental analysis yet is cheaper than helium as a large flow rate is needed. The argon gas is introduced through a quartz tube prior to the copper coil. Inside, running along the centre of the tube is a second very thin quartz tube where the nebulized sample solution is mixed in with argon gas. A small amount (volume similar to a pipette drop) is introduced otherwise it will extinguish the plasma. A third quartz tube sheaths the first tube and argon gas flows in the gap between the two tubes to cool down the first quartz tube.

3.4.2 Acquisition of the ions for elemental analysis

Specially designed cones made from nickel are inserted into the plasma pointing into the plasma flame, which help separate the ions to be measured from the argon. A small aperture in the centre of the cone, approximately 0.5 mm for AES, allows

Chapter 3. Experimental Methods

only those elements for analysis to pass through for the atomic emission spectra to be measured whilst minimizing the number of surrounding argon ions. The cone for the AES is positioned further from the centre, in a cooler part of the plasma flame to measure the spectra resulting from electronic transitions. AES measurements are taken directly from the emission spectra using sophisticated optics. The AES technique gathers spectral information simultaneously and is ideal to obtain large elemental percentage weight values very accurately within a sample.

3.4.3 Calibration

Calibration is imperative for this technique. Standards of the elements to be analysed at various concentrations - ppm concentration are used for AES - are measured and a calibration curve of counts/second against concentration are plotted for each element by subtracting a blank background from the standards. Ideally a linear fit through each of the points is required; better the fit, the more accurate the results will be. The calibration curves also set the limits for the maximum and minimum concentration values that can be measured with confidence. Measurements of concentrations above the maximum on the calibration curve will assume that the straight line fit can be extrapolated.

Throughout the course of an extensive set sample measurements, the machine will drift: the main example is fluctuations in room temperature will slightly alter the configuration. The other contributing factor during the measurement of samples that can cause a drift in calibration is the performance of the peristalsis pump. This draws up the sample into the plasma chamber and the precision of the volume sprayed into the chamber may alter throughout a run of measurements. A drift monitor was placed between every 10 samples to measure changes in calibration.

Calibration for some elements may be more problematic; some elements poorly ionise, for instance only 30% phosphorus ionises. Although allowing for a weighting of ionisation, lighter elements are still slightly under counted, because of their lighter mass they have a greater radial axial distribution as they travel through the plasma flame and thus are more likely to be deflected by the nickel cone or caught in the charged net.

3.4.4 Sample Preparation

Good sample preparation is crucial for ICP analysis as many of the errors in a measurement may come from human error. Both ICP methods require solutions and these involve complicated processes to ensure all the sample is dissolved and to minimize interference (explained below). The method for jarosite digestion was dissolving 60mg of jarosite sample in aqua regia approximately 5cm³ and warmed on a heating bath until dissolved. The solution was then made up to 25cm³ using a 2% HNO₃ solution. 2% HNO₃ is required to achieve the right viscosity to pass through the ICP machine. The blank must also go through the same process of preparation.

3.4.5 Sources of Errors

Human error

A large source of error comes from sample preparation, for example in weighing and measuring. Loss of sample during the process necessary to produce a homogeneous solution for elemental analysis, usually through the solution spitting or evaporating whilst on the hotplate. Other source of human error is poor calibration of the instrumentation and measurements.

Systematic errors

The two most common are linked to the injection of the sample into the plasma flame. The most widely used method for uptake of the prepared solution into the machine is through a peristalsis pump, although highly efficient, the very nature of the mechanism of delivery may not provide a continuous flow into the nebulizer which in turn is another source of error. Only 1-2% of the sample which reaches the nebulizer is actually turned into a spray and the volume of spray is never constant.

Systemic errors “interference”

Considerable errors can come from the properties of the plasma and because its flame is open to atmosphere. In the case of the ICP-MS, many argon species

Chapter 3. Experimental Methods

formed have similar M/Z ratios as common elements. Iron can never realistically be measured on an MS with an argon plasma because many Ar-O_(n) species are formed and Ar-O has the same M/Z as ⁵⁶Fe which will give a false measurement. Hence why only ICP-AES was used for Fe jarosites.

Similar problems may exist with ICP-AES as there may be an overlap with the spectral lines. Though it should be resolved with higher resolution instruments. Sulphur represents a major difficulty, the spectral line appears in the UV range and is at the limit for the optics (mechanical problems from scanning such a large range), but also importantly the UV is absorbed by oxygen present in the machine and thus will reduce the intensity of the signal. In order to reduce this, the analysis would have to be carried out under a low atmospheric pressure environment which requires a larger flow rate of argon.

Another limitation with the ICP-AES is with high percentage weight of atoms which can be easily ionised. As the cone for ICP-AES is in the cooler part of the flame light ions like potassium or sodium may undergo electronic transitions and emit emissions before passing through the cone and therefore a slight drop in intensity may be noticed for such elements.

3.4.6 Collection of results

ICP-AES results were collected on two different machines. A commercial service using the ICP-AES at the Natural History Museum. Here the results were returned as percentage weight and as a service the preparation and result collection was undertaken by the machine operator. The solutions were dissolved in HCl following the method set out by A.M. Smith [26]. The ICP-AES ran with a high argon flow (low oxygen) and the optics were fully functional. The second machine was a Perkin-Elmer ICP-AES at Kingston university. Two batches of samples were run. The first set of results are effectively void: a breakdown in the optics meant the intensity of the sulphur line was very low and the sulphur content could not be quantified. The second set followed the same method outlined by A.M. Smith [26].

The results from the experiment were returned as ppm and were converted as a weight percentage. This requires normalisation to an element. Oxygen is not recorded because of the air content and thus to work out the chemical formula the

assumption is that the sulphate is always of full occupation for jarosites.

3.5 Scanning Electron Microscope

The Scanning Electron Microscope (SEM) is a very good tool for visualization of samples at the meso (μm) and nano (nm) length scales. It clearly shows the morphology, size and surface details of crystals and crystallites. SEM provides the best visual confirmation of any impurities, allowing the observation of amorphous content or impurity phases. One can see how the morphology clearly changes over a solution series. EDX SEMs (Energy Dispersive X-ray Spectroscopy) is a useful tool to undertake elemental analysis. This efficient and effective method for elemental analysis requires minimal sample preparation.

SEM uses a beam of electrons for the visualisation of microscopic objects in real space. This is performed by projecting a highly focused beam onto the surface of the sample. Scanning microscopes utilise the resulting electron interaction with the surface to obtain different measurements. Backscattered electrons and secondary electrons produce the visual information about the morphology. Backscattering occurs when a direct interaction happens between an incident electron and an atom on the sample surface. The degree of backscattering varies with atomic number, the heavier the atom, the brighter the backscattering.

Secondary electrons provide good information about the topology of the surface. As an incident electron travels into an atom, it will energise one or more electrons in the K shell. The resultant kinetic energy of the excited electron is small $\sim 5\text{keV}$ and because of the local probe of secondary electrons will give detailed information of the topology. These electrons are then accelerated towards a potential and counted.

The use of Auger electrons and X-rays generated by the excitation of the K shell electrons are used to determine elemental analysis as the X-rays and Auger electrons are characteristic of individual elements.

3.5.1 SEM Morphology studies

SEM images although monochromatic, can produce a 3D image because of contrasting occurring from the angle of incidence of the electron beam upon a surface.

Chapter 3. Experimental Methods

Electrons scattered or emitted from a perpendicular surface will give a uniform but less brilliant signal as some secondary electrons will penetrate into the sample, whereas edges and high angle of incidence will result in more secondary electrons being counted.

Morphology studies were carried using a Joel F operated with a 15KV electron beam and a probe distance of 16mm. Jarosites are insulating and thus need to be coated in gold to prevent charge from building up on the surface of the samples. The samples were not polished because of the brittleness of jarosites. The samples are mounted onto an aluminium stub with a very tacky black surface to hold down the sample which is delicately sprinkled upon the surface. It is then placed into a gold sputterer to coat the surface. The Joel can achieve very high magnifications, but requires a high vacuum to obtain this. Therefore it is important that samples are dry before placing into the vacuum chamber and only 1-3 samples at a time can be analyzed.

3.5.2 EDX SEM Elemental analysis

Elemental analysis was carried out using a Philips Environmental SEM with EDX. Environmental SEMs run at a lower vacuum and are not suitable for morphology studies but very successful for elemental studies. Attached is an Oxford instruments INCA energy dispersive X-ray spectroscopy which analyzes the energy of the associated electrons emitted from the sample surface which is dependent upon the atomic number of the atoms. EDX may have a lower resolution compared to wavelength dispersive but can operate at lower vacuums and can distinguish better between lighter atoms. The high water content of the jarosites rendered this technique unusable for elemental analysis. In essence the electron beam obliterated the surface and vaporized the water content rendering Fe:S ratios widely overestimated. The results are reported as percentage weight and with the loss of oxygen no meaningful elemental analysis can be undertaken using synthetic jarosites in particular hydronium jarosites with their high water content.

3.6 Superconducting Quantum Interference Device Magnetometry - SQUID

The SQUID is the most sensitive instrument available to measure the magnetisation of a sample. It measures, as an interferometer, changes in magnetic flux. The sensitivity can measure changes as slight as $2.07 \times 10^{15} \text{ Tm}^2$, which is size of one unit of quantised magnetic flux.

The SQUID uses Josephson junctions and measures the difference in phase between two currents that are split passing around a superconducting loop. The loop is made up of two half loops with a Josephson junction (a very thin insulating layer, which still allows a super current to tunnel through without loss of phase coherence) between the two points of contact. A constant persistent current is passed throughout the ring; one Josephson junction is coupled to the magnetic environment of the sample by two pick up coils wound in opposing directions; the current is able to pass freely through the second junction. The voltage will change as the phase changes on passing through the two different environments at the junctions, corresponding to changes in magnetic flux. Only phase differences of 2π are allowed, which is important when there is an applied flux; changes in applied flux will cause oscillations in the voltage traversing the loop, counting these oscillations relates to the number of quanta of flux the SQUID is exposed to.

To achieve a high sensitivity and to be able to measure small changes in magnetic flux, the SQUID uses the properties of Cooper pairs (condensate electron pairs). Cooper pairs are not scattered by phonon interactions and therefore have a resistance of zero. This means that the particle can remain phase coherent over long distances and a Cooper pair has the mass and charge of two electrons. A SQUID measures the change in the phase between two sets of travelling Cooper pairs around the loop. Great sensitivity can be achieved by changes in current density and magnetic field. The SQUID is setup to emulate a Young's slits for the Cooper pair waves as set out in Figure 3.3.

In the case of a SQUID (Figure 3.3), one junction X is subjected to the varying magnetic field caused by measuring the magnetic response of the sample, whereas the other junction ,Y, is unaffected (Figure 17). The two phases are recombined at

Chapter 3. Experimental Methods

Z producing an oscillating voltage caused by interference of the two Cooper pair waves, this can then be used to determine the field applied at junction X.

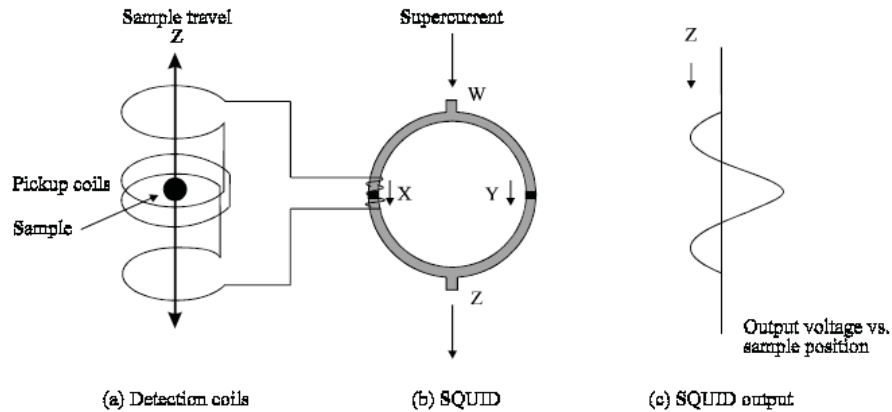


Figure 3.3: Schematic for DC SQUID. a) shows the pickup coils where the magnetic flux from the sample is detected, either in the absence or with an applied field. b) shows the loop with the two Josephson junctions at points X and Y. The current is recombined at Z and the output from Z is shown in c). The oscillating voltage relates to the magnetic flux applied at X, obtained from the interference of the two superconducting phases passing through X and Y.

All the magnetic measurements of the samples were made using a Quantum Design MPMS-7 DC SQUID. This machine was capable of measuring the magnetisation of samples from temperatures of 1.9K up to 310K. The maximum applied magnetic field is 7T and applied fields as small as a tenth of a Gauss can accurately be applied. There were two MPMS-7 DC SQUIDS instruments used, both had slightly different capabilities. The RI SQUID (Royal Institution of Great Britain) was capable of taking continuous measurements below 4.17 K and has the sweep facility to enable measurements to be taken without to wait for temperature stability, which is useful for quick characterization. The RI SQUID had a poor temperature stability which meant 4 measurements per data point were required to reduce errors. The CMMP SQUID (Condensed Matter and Materials Physics, UCL) did not have the extra options of the RI SQUID. Instead it contained up to date software which allowed more specific and precise sequences to be written, had a better temperature stability and thus only 2 measurements were taken per data

Chapter 3. Experimental Methods

point and importantly contained a magnet reset facility.

All jarosite samples were ground and approximately 50mg of each sample was placed inside a gelatin capsule, ensuring no contamination to the capsule or the sample with any impurities which may provide a ferromagnetic response. The gelatin capsule was then inserted ~ 5 cm into a Quantum Design straw. Two small T-shaped incisions across the straw were made above and below the gelatin capsule, and the flaps created pushed into the straw to help ensure the gelatin capsule did not move too much inside the straw. The capsule was sometimes wrapped in Kapton tape to provide a tighter fit inside the straw. Several small incisions were made near the top of the straw and the top of the straw was pushed about 1 cm onto the end of a long thin brass/stainless steel rod. Kapton tape is used to cover the end of the straw nearest to the sample to prevent the sample from falling out during the experiment. This rod with a sample mounted straw at the end is gently pushed all the way inside the Quantum Design SQUID.

The sample is then centered between the two pick up coils and any remnant magnetisation is removed or an opposing field applied to produce an effective zero applied field. The sample position was always set to 4 cm and depending on the instrument 2 or 4 measurements taken per data point. Positioning the sample and determining zero field is always done at a reasonably high temperatures (100K) far removed from any magnetic transitions for the jarosite samples.

Measurements below 4.17 K can sometimes become troublesome. To achieve temperatures below 4.17 K, then the small reservoir of helium surrounding the sample is pumped upon. The volume of the reservoir is limited and will have to be refilled and the maximum time usage can vary from as little as 30 minutes to 2 hours. When the helium reservoir has to be refilled the temperature reaches approximately 10 K before returning to the set temperature. This will cause the sample to be field cooled and influence the magnetic response of the sample compared to the zero field cooled environment. The RI SQUID has the advantage of a continuously filled helium reservoir, though temperature tolerance has to be increased.

3.6.1 Temperature Sweep Measurements - Zero Field Cooled and Field Cooled (ZFC/FC)

To obtain the following physical information; Curie-Weiss constant, θ_w , susceptibility, χ , effective moment, μ_{eff} and to determine the temperature of magnetic transitions and their nature; temperature sweep measurements in a fixed field can provide all this information. A sample is cooled down to the lowest temperature possible (2 K) or 5 K (if He is limited) in zero applied field, from a temperature far above the expected transitions temperatures ($T_g \sim 11 - 20$ K for hydronium jarosite and 45-65 K for non-hydronium jarosites). Once at base temperature and the sample has reached thermal equilibrium an external field is applied. A low applied field of 100 Oe was applied for all jarosites. The sample is warmed and a predetermined sequence will define at which temperatures to take measurements. Measurements are usually taken at temperature steps of 0.5 K or 0.25 K through the transition region, a range of 10-20 K. Whereas larger steps, 10-20 K, are sufficient for Curie-Weiss determination in the paramagnetic temperature region. The sample is warmed to as high a temperature as possible (usually 310 K) to obtain a Curie-Weiss fit to the data. After the final measurement the sample is cooled back down to the base temperature with the same applied field. After thermal equilibrium has been reached the sequence of measurements is repeated.

The sequences are set not to overshoot the required temperature for each data point and to wait for temperature stability before taking the measurement. The use of the sweep facility on the RI SQUID is useful to obtain the transition temperature(s) if unknown prior to a detailed ZFC/FC run.

To obtain the susceptibility, χ ; μ_{eff} and the Curie Weiss temperature, θ_W , from the data the following calculations are carried out.

$$\chi_{mol} = \frac{A_r \times emu}{(\mathbf{B} \times S) - D_{mol}} \quad (3.1a)$$

A_r is the molar mass (g), emu is the corrected magnetisation (cgs units) removing the diamagnetic contribution from the straw and gelatin capsule. \mathbf{B} is the applied field in Gauss and S is sample mass (g). D_{mol} is the molar diamagnetic contribution

Chapter 3. Experimental Methods

from the following ions; SO_4^{2-} , OH^- and A-site $^+$.

$$\mu_{\text{eff}} = \sqrt{(8\chi_{\text{mol}}T)} \quad (3.1b)$$

T is the temperature (K). The units for μ_{eff} in cgs are ergs/Gauss.

The Curie-Weiss temperature, θ_{W} , is determined by fitting a straight line fit to χ_{mol}^{-1} where the plot is linear (paramagnetic region) and θ_{W} is the temperature value where the line intercepts the x axis.

Diamagnetic corrections have to be made arising from the contributions of all atoms, ions, ligands and the straw and capsule. These are summed together and subtracted from the magnetisation measurement to make a correction for the susceptibility. Diamagnetism is independent of field and temperature and are tabulated as Pascal constants [27].

3.6.2 Field Sweep Measurements

Field sweep measurements were used to determine the presence of hysteresis. Three different types of hysteresis measurement were used.

Standard Hysteresis Measurements

Standard hysteresis measurement is to sweep in positive and negative field returning to maximum positive field: all at a fixed temperature with fields up to ± 7 T. The temperatures were set either above and below a given transition temperature. An illustration of an expected hysteresis loop by this method is shown in Figure 3.4

Hysteresis loops in a small positive field

Two hysteresis sub-loops were performed on a virgin curve. Please refer to Figure 3.5 for an illustration of the measurement. Starting from zero field, magnetisation measurements were made as the field is gradually increased. At a certain field, H_1 , the applied field is reduced and magnetisation measurements are taken in a loop back to zero applied field and then increased back to and through H_1 . The field is further increased, and upon reaching a larger field, H_L , another sub-loop

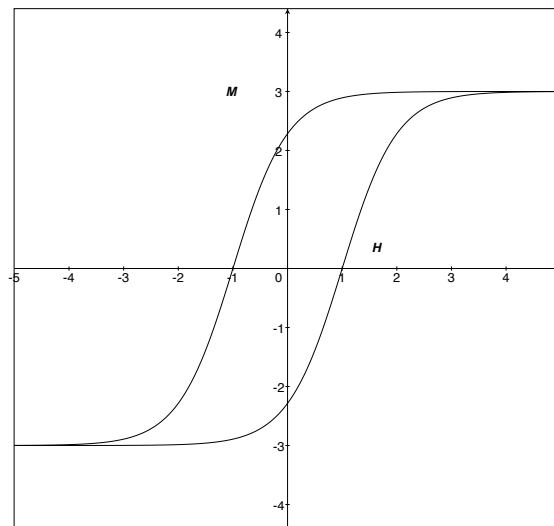


Figure 3.4: An expected hysteresis loop by applying large positive and negative fields to produce saturation in the magnetisation of the sample. The gap produced by the two magnetisation curves is called the coercivity and describes the hardness of the system. A more fluid movement of reorientation of spins will result in a small coercivity

Chapter 3. Experimental Methods

is performed by reducing the field back to zero, then increasing back to H_1 , then reducing back to zero before increasing again to H_1 and reaching H_L again.

It is expected far above the transition temperature then the two sub-loops should be congruent. Below a given transition temperature the expectation is for the two sub-loops not to be congruent supporting the build up of correlations prior to the magnetic transition.

Displacement Hysteresis

Displacement hysteresis measurements comprises of two standard hysteresis measurements: the sample was zero field cooled prior to the first hysteresis loop and field cooled in a small field prior to the second hysteresis loop. An expectant result is shown in Figure 3.6: displacement in magnetisation (y axis) between the two sets of hysteresis measurements.

3.7 Diffraction

The phenomena of diffraction, the interference of wave propagation, occurs when the wavelength of the incident wave front and the medium through which wave passes through is similar in size to the incident wavelength. This condition happens when X-rays pass through crystalline materials, the separation between planes of atoms and the wavelength of X-rays are very similar $\sim 1 - 2 \text{ \AA}$. The relationship between the separation of the planes of atoms and X-ray wavelength was derived by the William and Lawrence Bragg leading to Braggs' law (3.2).

$$2d \sin \theta = n\lambda \tag{3.2}$$

The derivation of the Braggs' law considers consecutive reflective parallel planes, where each plane is partially reflective. At zero angle of incidence between the X-ray and the electron, the scattered radiation is in phase and no interference occurs. As the angle of incidence increases so the scattered radiation destructively interferes and this increases with greater angle leading to drop in form factor for the atomic scattering.

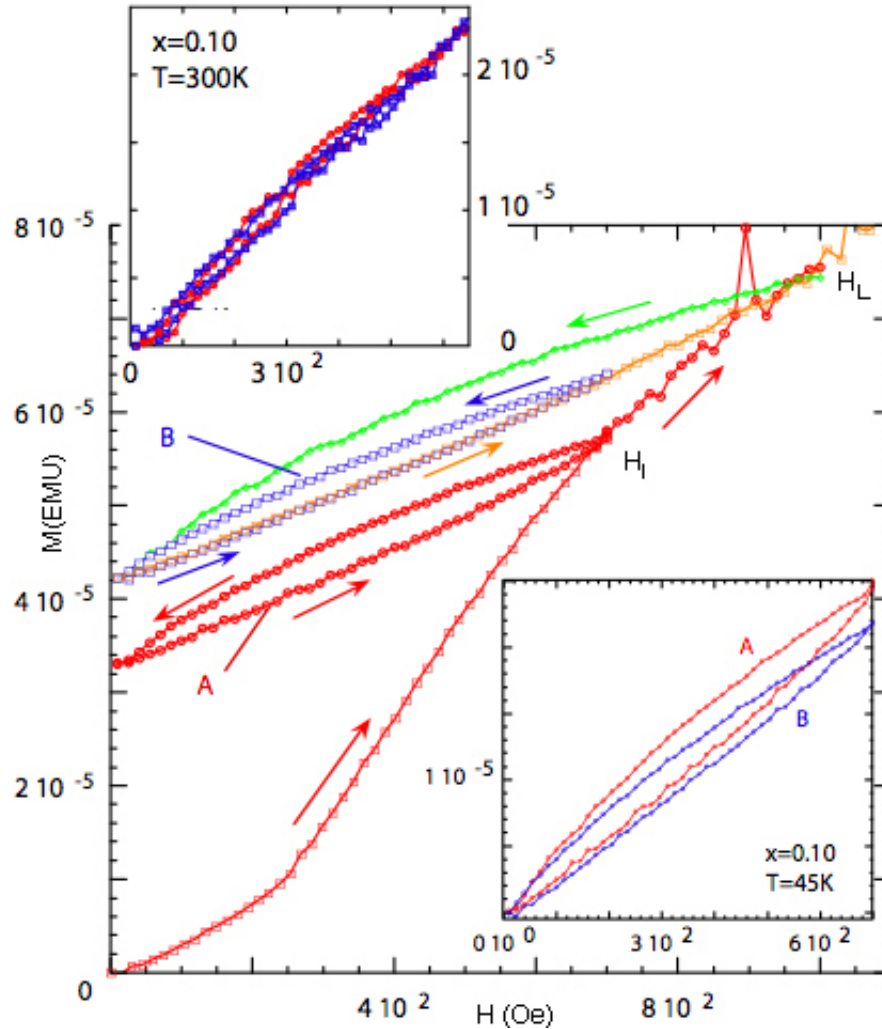


Figure 3.5: Positive hysteresis loops taken from a virgin curve. A small field is gradually applied (red squares) whereupon at a field (H_1) the field is gradually reduced to zero and then gradually increased back to H_1 (red circles). The field is continually applied to a new greater field, H_L , whereupon it is gradually decreased to zero field (green line) and following a loop is made from zero to H_1 and back to zero (purple squares) before increasing beyond (orange squares) H_L . Lower insert shows how the two positive sub-loops taken from the virgin curve are not congruent, whereas at 300K (upper insert) the two sub-loops are congruent highlighting that the domains at 300K are acting independently. (This figure is taken from the article [1] investigating magnetic correlations in the high temperature superconductor $\text{La}_{2-x}\text{Sr}_x\text{CuO}_4$ prior to the superconducting transition.)

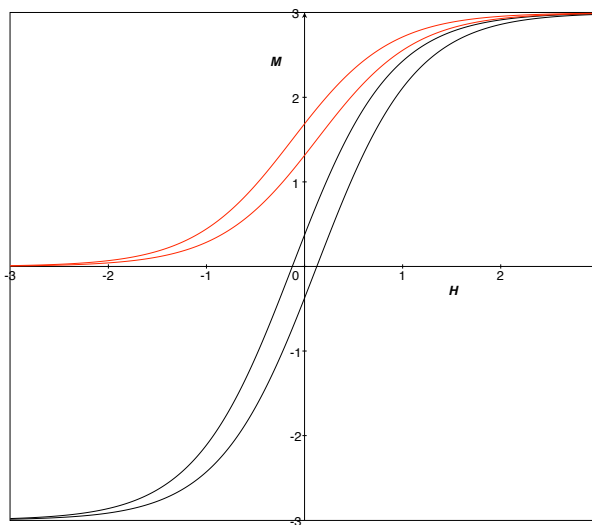


Figure 3.6: Predicted displacement hysteresis loops: the corecitivity is expected to be small or negligible but a displacement in the magnetisation between the red and black hysteresis curves. The red hysteresis curve is for where the sample has been field cooled in a small field prior to measurement.

The angle of incidence is equal to angle of reflection. A Bragg reflection is only observed when the reflective beams constructively interfere as shown in Figure 3.7.

To determine the scattering intensity from the electron distribution of the atoms in the cell Fourier analysis is used, as the electron density of a plane of atoms is arranged in a periodic fashion, representing a frequency ideal for Fourier transform. As the diffraction is defined using a period of a , and with p , the Fourier coefficient, $2\pi p/a$, represents a point in reciprocal space or a point on the reciprocal lattice. These reciprocal lattice points show us the allowed terms in a Fourier series expansion which is consistent with the periodicity of the crystal. To express the relationship of the periodic function of electron density $n(r)$ in three dimensions with the spatial distribution of the atoms, then the reciprocal lattice vector, \mathbf{G} , has to be invariant over all lattice translations (3.3),

$$n(\mathbf{r}) = \sum_{\mathbf{G}} n_{\mathbf{G}} \exp(i\mathbf{G} \cdot \mathbf{r}) \quad (3.3)$$

where $n_{\mathbf{G}}$ are the set of Fourier coefficients that determine the scattering ampli-

Chapter 3. Experimental Methods

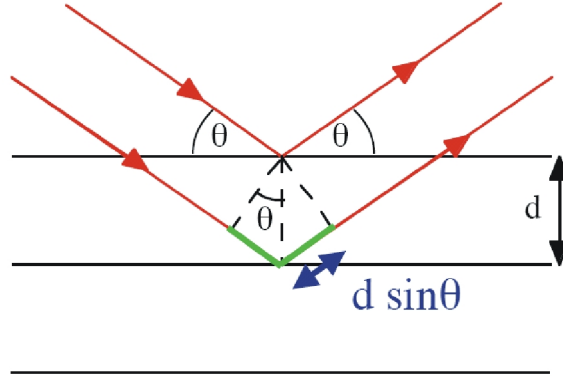


Figure 3.7: In order for constructive interference to occur, the beam which traverses an extra distance of $2d\sin\theta$, that distance must be equal an integral number of wavelengths, $n\lambda$: as θ increases so the d spacings become smaller.

tude. The set of reciprocal lattice vectors \mathbf{G} represents the possible allowed X-ray reflections. The reciprocal lattice points can be obtained from real space by the relationship in (3.4).

$$\mathbf{b}_1 = 2\pi \frac{\mathbf{a}_2 \times \mathbf{a}_3}{\mathbf{a}_1 \cdot \mathbf{a}_2 \times \mathbf{a}_3}; \mathbf{b}_2 = 2\pi \frac{\mathbf{a}_3 \times \mathbf{a}_1}{\mathbf{a}_1 \cdot \mathbf{a}_2 \times \mathbf{a}_3}; \mathbf{b}_3 = 2\pi \frac{\mathbf{a}_1 \times \mathbf{a}_2}{\mathbf{a}_1 \cdot \mathbf{a}_2 \times \mathbf{a}_3} \quad (3.4a)$$

The points in reciprocal space are mapped by

$$\mathbf{G} = v_1 \mathbf{b}_1 + v_2 \mathbf{b}_2 + v_3 \mathbf{b}_3 \quad (3.4b)$$

In the situation of an incident wave vector \mathbf{k} separated by a volume \mathbf{r} apart, the amplitude of the scattered wave vector (k') is proportional to the local electron density ($n(r)$) surrounding the volume origin. The total amplitude is proportional to the integral over the whole cell, $n(r)dV \cdot \exp[i(k - k') \cdot r]$, the exponential term is the phase factor. The amplitude of the vectors for a scattered electromagnetic wave is defined as F in equation (3.5),

$$F = \int dV n(\mathbf{r}) \exp(-i\Delta\mathbf{k} \cdot \mathbf{r}) \quad (3.5)$$

Chapter 3. Experimental Methods

where $\mathbf{k} + \Delta\mathbf{k} = \mathbf{k}'$ and $\Delta\mathbf{k}$ is the scattering vector.

In the case of elastic scattering, $\Delta k = \mathbf{G}$ (Figures 3.8), from a unit cell of N atoms this generates the structure factor which contains the total amplitude of the wave vectors scattered from a unit cell (3.6). The phase information is lost: knowledge of the phase is of utmost importance as knowing the phase relationship will know how the interference of the wave vectors occurred and correspond the correct structure factors. The phase problem will be discussed later in this chapter.

$$F_0 = N \int dV n(\mathbf{r}) \exp(-i\mathbf{G} \cdot \mathbf{r}) \quad (3.6)$$

In three dimensions to satisfy the condition that $\Delta k = \mathbf{G}$, then Δk has to lie on the intersection of three cones in the direction of their respective axis (3.4) shown in equation (3.7).

$$\mathbf{a}_1 \cdot \Delta\mathbf{k} = 2\pi v_1; \mathbf{a}_2 \cdot \Delta\mathbf{k} = 2\pi v_2; \mathbf{a}_3 \cdot \Delta\mathbf{k} = 2\pi v_3; \quad (3.7)$$

It is very unlikely for this condition to occur unless one scans through by angle or wavelength. This condition is illustrated by the Ewald construction (Figure 3.8).

3.8 Powder Diffraction

3.8.1 Powder Diffraction - X-ray

Powder diffraction allows the checking of phase purity and amorphous content. Powdered samples means that the resultant diffraction pattern will produce rings of scattered intensity in the diffraction sphere as many crystallites, each with their own orientation contribute to the pattern. Thus the data is effectively reduced to 1 dimension creating considerable peak overlap. Structure solution of unknown powdered samples becomes a non-trivial matter for powder diffraction, almost impossible, however, for known structure solutions powder does have many advantages over single crystal. The resolution of the diffraction can be much better than single crystal combined with the ability to obtain reflections over a much larger 2θ range (from $1 - 140^\circ 2\theta$) allows for greater precision of the lattice parameters. Phase

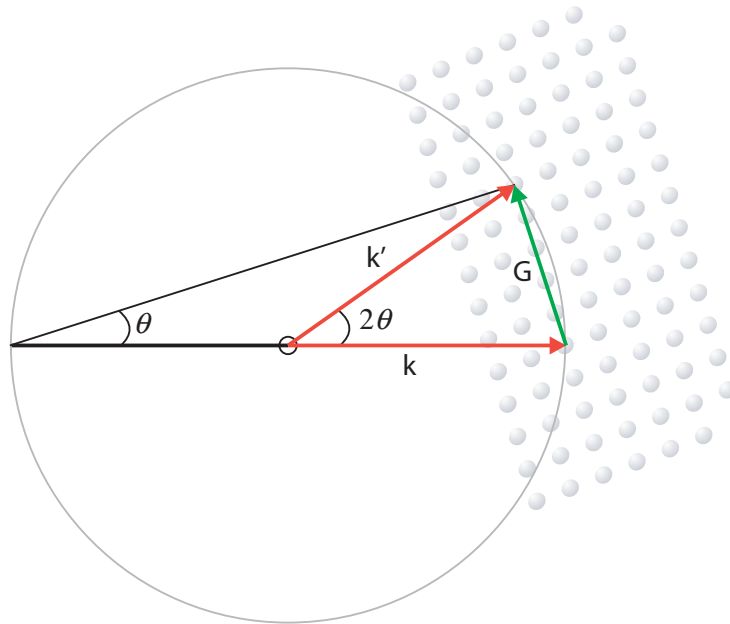


Figure 3.8: The Ewald construction shows how the unlikely condition of a Bragg reflection occurs. An incident X-ray with wave vector \mathbf{k} will terminate at any reciprocal lattice point shown as the shaded points on the right. This distance from a chosen origin to that lattice point will form the radius of a diffraction sphere, $k = 2\pi/\lambda$. A Bragg reflection will only occur if the sphere will pass through another reciprocal lattice point. The relationship between wave vector \mathbf{k} and the diffracted beam \mathbf{k}' is the reciprocal lattice vector \mathbf{G} , $\mathbf{k}' = \mathbf{k} + \mathbf{G}$ and the angle θ is the Bragg angle.

Chapter 3. Experimental Methods

purity analysis can also be used to check the sample as the powder diffraction is from the bulk and thus data may be more representative of the sample.

Data collection

All iron jarosite X-ray diffraction data were collected in Bragg-Bretano geometry on a low background silica plate using a Bruker D8 diffractometer with $\text{CuK}_{\alpha 1}$ radiation and a PSD detector with a step size, $\Delta(2\theta) = 0.073^\circ$, from 2θ range $5^\circ - 70^\circ 2\theta$ with a scan time of 65 minutes and rotated at 15 rpm at room temperature. Each sample was lightly ground and a small amount was added to centre of the low background silica plate and a couple of drops of acetone was added to make a slurry. All iron jarosite samples were measured in this standard procedure. The primary purpose was to firstly to check for phase purity and importantly to catalogue any changes with lattice parameters with synthesis conditions (Vegard's law). Lattice parameters were refined using the Rietveld method from a previously know model for the hydronium jarosite [28], the process of Rietveld refinement is explained later in this section. The data taken for the jarsoites was of insufficient quality to undertake a full structural refinement, only worthwhile for lattice parameters, because of the raised background as a consequence of the Fe fluorescence from CuK_{α} radiation.

Phase identification

To check the phase purity of the sample and to look for the presence of unwanted iron oxy-hydroxy sulphates the raw diffraction patterns were analysed using Bruker's own pattern matching software - EVA, by comparing with patterns in its database and also looking for changes in 2θ for the intense peaks.

3.8.2 Powder Diffraction - Neutron

Thompson scattering can be applied to describe the scattering by neutrons from the nucleus and instead of an atomic form factor closely related to Z , the scattering lengths for each element are random throughout the periodic table and some are even negative - ^1H . Elements also have a cross section, which describes the trans-

Chapter 3. Experimental Methods

parency of an element to neutrons. The greater the cross section the more neutrons will be absorbed by the nucleus and hence a decrease in intensity. Consideration needs to be taken into account to be aware of the individual scattering lengths and cross sections of each of the elements in a sample.

The benefit of using neutrons for diffraction experiment is the wide range of energies accessible from neutrons. From de Broglie's relationship this can lead to wavelengths λ (Å) from 0.1 to 100. Neutrons have a very high penetration into materials and because they have a nuclear spin of $S = \frac{1}{2}$ then make them of prime importance for magnetic diffraction. These properties enable investigations into many physical properties of materials; phonons, magnons, crystal and magnetic structure and even including investigating ancient artifacts.

There are two means of producing neutrons for diffraction; spallation and nuclear reactors. Spallation sources provide the highest energy neutrons - epithermal neutrons ($\lambda = 0.1 - 0.5$ Å) which give very high resolution for diffraction experiments. Neutrons are produced by bombarding a metal target (W, U or Hg) with protons accelerated in a synchrotron.

Constant wavelength neutrons are produced in a nuclear fission reactor (60-100MW). The energy is limited as most is dissipated as heat and only 1 neutron is available per fission event for diffraction. The neutrons are guided out of the reactor core and passed through a moderator and leave with energies no greater than $\lambda \sim 1$ Å. These sources provide a constant flux of neutrons.

Time of Flight Neutron Powder Diffraction

Time of flight neutron diffraction allows for high resolution diffraction over a wide range of d-spacings at a fixed scattering angle. This increase in resolution, $R(d)$, is achieved by increasing the time of flight, t , of the neutrons shown by the relationship in equation (3.8).

$$R(d) = \Delta d/d = \Delta t/t \propto 1/d \quad (3.8)$$

To increase the resolution then increasing the path length, L , of the neutrons will simply increase the resolution as there is a linear relationship with neutron wavelength and time of flight. The overall resolution is described by the function

Chapter 3. Experimental Methods

(3.9) [29]

$$R(d) = \Delta d/d = [(\Delta t/t)^2 + (\Delta\theta \cot \theta)^2 + (\Delta L/L)^2]^{\frac{1}{2}} \quad (3.9)$$

From equation (3.9) it can be seen that a detector placed at 180° from the sample will have the highest resolution.

The d-spacing from time of flight is obtained by using the de Broglie relationship as shown in (3.10)

$$\lambda = 2d \sin \theta \quad (3.10a)$$

$$\lambda = h/mv = ht/mL \quad (3.10b)$$

substituting (3.10a) into the de Broglie equation (3.10b), where h is Planck's constant, m is the mass of a neutron and v is the neutron velocity, gives the d-spacing relationship for time of flight (3.11).

$$d = ht/(2mL \sin \theta) \quad (3.11)$$

Time of flight diffraction was carried out at the High Resolution Powder Diffractometer (HRPD) instrument at ISIS. A schematic of the instrument is shown in Figure 3.9, the path length, L , is approximately 100m.

Constant Wavelength Neutron Powder Diffraction

Neutron powder diffraction was performed on a double axis diffractometer. This consists of one axis which contains the monochromator that will define the wavelength used and the second axis is where the sample is positioned. 2θ is usually measured using an area detector surrounding the sample. Powder diffraction patterns of the deuterated samples of both Fe and Cr jarosites were taken at the medium resolution instrument, D20, at the Institut Laue-Langevin (ILL). The D20 is constant wavelength high flux instrument enabling thermo-diffraction experiments as well as magnetic structure determination. A schematic of the detector is shown in Figure 3.10.

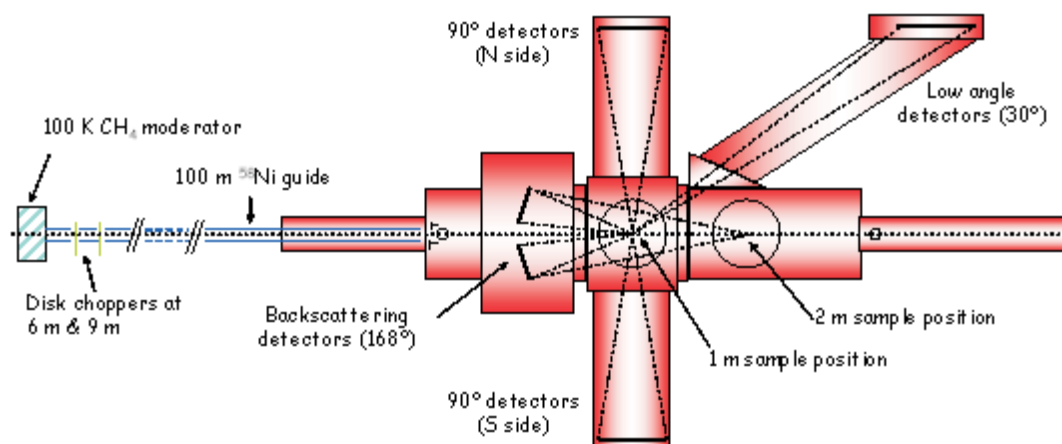


Figure 3.9: Schematic showing the instrument layout for HRPD. The greatest resolution is achieved by the back scattering bank and very useful for small d spacing going out as far as 5-6 Å. The 90° bank has the greatest solid angle and high flux. The low angle bank unfortunately has the poorest resolution and lowest intensity due to the small solid angle and is insufficient for magnetic scattering. The schematic is taken from the HRPD manual on the ISIS website.

3.8.3 Rietveld refinement

Rietveld refinement method was developed by Hugo Rietveld [30, 31] in the late 1960's when he realised that computing power could potentially solve crystal structures from powder data. Prior to Rietveld's work, only simple or high symmetry crystal systems could be solved from powder diffraction; whilst more complex systems suffered from overlapping reflections and, until Rietveld's method was introduced, their contribution to the overlapping peaks was difficult to identify.

The computer program devised by H. M. Rietveld is an iterative method which can simultaneously refine peak intensities - even if the intensities have contributions from several reflections - and is constantly updating and giving feedback on the refinement structure. The Rietveld method carries out a least-squares process until the best fit is obtained between the observed powder diffraction pattern and a calculated structure pattern. The calculated pattern is determined by the crystal structure, the instrument parameters and importantly lattice parameters. The peak profile can be represented as follows,

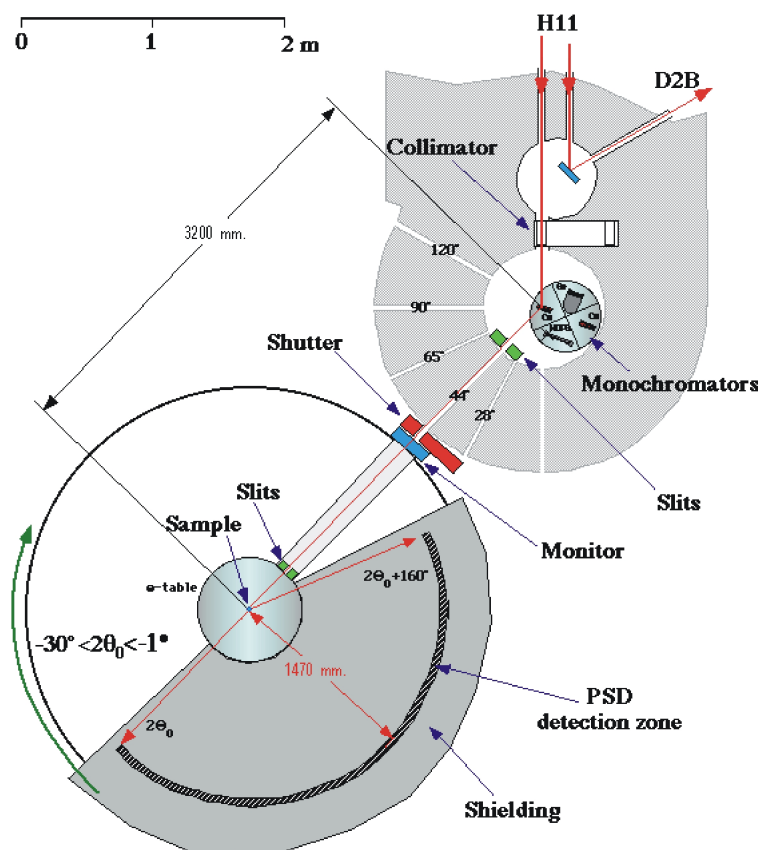


Figure 3.10: The D20 is a two axis medium resolution high flux powder diffractometer. The monochromator is a 111 single Ge crystal. The detector is a position sensitive detector, covering $160^\circ 2\theta$, containing ^3He and propane comprising of 1600 cells, the first and last 32 cells are redundant. The schematic is taken from the D20 manual on the ILL website.

$$y(2\theta) = b(2\theta) + [w(2\theta)g(2\theta)]f(2\theta) \quad (3.12)$$

$b(2\theta)$ represents the background and $f(2\theta)$ represents the sample. $w(2\theta)g(2\theta)$ represents the total instrument profile, made up from the $w(2\theta)$ function representing the wavelength distribution and $g(2\theta)$ which represents the instrument optics and corresponding sample effects (height, sample transparency, surface roughness, Soller and receiving slits and zero offset).

The function $f(2\theta)$ depends upon the sample characterisation. Upon Fourier transform of an infinite crystal, it will yield a Dirac delta function. In reality, differences in size and strain between the atoms will broaden a reflection. As powder diffraction is an averaging technique, oscillating between certain sizes, $f(2\theta)$ is modeled using a Gaussian or Lorentzian or a convolution of the two functions and the area is the integrated intensity.

Least-Squares

When data is collected it is recorded as intensity, y_i for each step, i , and the power of the Rietveld process simultaneously seeks to fit all the intensities with a non-linear least-squares method. The quantity is minimised by an iterative method using this equation to give the residual S_y

$$S_y = \sum_i W_i (y_i - y_{ci})^2 \quad (3.13)$$

$W_i = 1/y_i$ and y_i is the observed intensity for every step, i . y_{ci} is the calculated intensity at each step, i .

This is then fed back into the model and the process is repeated until convergence is achieved. This makes the Rietveld process so powerful: instead of trying to extract the intensity of individual peaks, the whole pattern is treated simultaneously and the calculated pattern from the model is improved upon by sequential feedback. A more detailed description of least squares is given in the Crystallography Appendix.

Chapter 3. Experimental Methods

Starting Refinement Model

In a Rietveld refinement of a powder diffraction experiment, the peak profile (equation (3.12)) is composed of many of reflections, each with its own profile: height, position, breadth, displacement of the peak from the profile position, and integrated area. The integrated area is proportional to the Bragg intensity, I_K ; K stands for the Miller indices, h, k, l . I_K is proportional to the squared magnitude of the structure factor $|F_K|^2$. The Rietveld method does not seek to differentiate each peak and subscribe an intensity to each, it simply refines the entire value of y_i using a structure refinement method, requiring a starting model. The overlap problem ensures the method cannot be used backwards, and hence cannot refine the structure without first knowing the symmetry and the composition. This is required for the structure model where $|F_K|^2$ values are calculated and subsequently y_{ci} can be found by summing up the whole relationship which contributed to the Bragg reflections; this includes the background and preferred orientation.

$$y_{ci} = s \sum_K L_K |F_K|^2 G(\Delta\theta_{iK}) P_K A + y_{bi} \quad (3.14)$$

Where, s is the scale factor, K represents the Miller indices for a Bragg reflection, L_K are the Lorentz polarisation and multiplicity factors, $G\Delta\theta_{iK}$ is the profile function, $\Delta\theta_{iK} = 2\theta_i - 2\theta_K$, $2\theta_K$ is the calculated positions of the Bragg peak, P_K is the preferred orientation function, A is the absorption factor, F_K is the structure factor for each K Bragg reflection and y_{bi} is background intensity.

The profile function, $G\Delta\theta_{iK}$, as stated above, is normalised so that the sum over the peak range is 1, (peak cut off becomes important into how much information is required to contribute to a model), as they are not Dirac δ functions and the sum of the reflections that contribute to that peak. One important tenet is to know $G\Delta\theta_{iK}$, thus making the most of the information contained within overlapping peaks.

Background is usually the first parameter to be refined and it needs to be done with consideration. Over weighting the background contribution will give rise to a false good convergence criteria upon least squares minimisation. Experience

Chapter 3. Experimental Methods

has shown to fit the background by hand, using a polynomial fit between each background point. The background is primarily generated from the sample; either fluorescence from the sample, impurity phases or amorphous content contained in the sample or incident radiation falling upon the sample holder. Misalignment of instrumentations and leakage of neutrons from other nearby instrumentation will also raise the background.

Profile Function

Determination of the profile function, $G\Delta\sigma_{ik}$ is the most important aspect of Rietveld refinement. The use of standards can be of considerable help to reduce the difficulty in determining what contributes to the peak profile: instrumentation contributes the most to the profile. There are many profile functions which seek to fit the profile of the peak as a function of the instrumentation and a small contribution from the sample.

Rietveld refinement was originally conceived with constant wavelength, medium resolution neutron radiation. The best profile function was simply a Gaussian: multiple combinations and convolutions of function results in a Gaussian distribution (equation (3.16a)). Though a Lorentzian (equation (3.16b)) contribution will become evident with X-ray diffraction with the appearance longer tails in the pattern. Low angle diffraction will produce asymmetrical peak shapes due to the curvature of the Debye-Scherrer cone at low angles. Higher resolution instrumentation will also highlight size-strain effects of the sample upon the peak profile, giving rise to peak broadening especially at the bottom of the peak.

$$H^2 = U \tan^2 \theta + V \tan \theta + W \quad (3.15)$$

$$\frac{C_0^{\frac{1}{2}}}{H_K \sqrt{\pi}} \exp\left(\frac{-C_0(2\theta_i - 2\theta_K)^2}{H_K^2}\right), \text{Gaussian}("G") \quad (3.16a)$$

$$\frac{C_1^{\frac{1}{2}}}{\pi H_K} \left(1 + C_1 \frac{(2\theta_i - 2\theta_K)^2}{H_K^2}\right)^{-1}, \text{Lorentzian}("L") \quad (3.16b)$$

Chapter 3. Experimental Methods

$$\eta L + (1 - \eta)G \quad (3.16c)$$

η is the mixing parameter that is a linear function of 2θ , the refinable parameters are NA and NB

$$\eta = NA + NB^*(2\theta) \quad (3.16d)$$

The equation by Cagliotti et al. [32] (3.15) refers to the parameters that define the peak profile. H is the Full Width Half Maximum and is dependent on the refinable parameters U , V and W . H thus defines the profile for corresponding Gaussian or Lorentzian distributions. Peak shapes are invariably a mixture of instrumental setup, source and sample, and therefore a convolution of both Gaussian and Lorentzian profiles. The peak shapes profile functions can be complicated to enable better descriptions of instrumentation, the most widely used throughout this project for constant wavelength used a pseudo-Voigt profile (3.16c) modified by Finger, Cox and Jephcoat [33] which is implemented in GSAS as profile function 3 - refer to Crystallography appendix for further details

Preferred Orientation

After establishing the background and peak profile function ΔG_{iK} the next stage is minimising or taking into account preferred orientation. Preferred orientation may be of little significance or can pose a significant refinement problem. It is caused by the sample orientating itself in one or more particular ways in the sample holder giving rise to certain Bragg intensities becoming stronger or weaker than is expected for a system. This can jeopardize a Rietveld refinement if this is significant because the profile will be over weighted or under weighted throughout the diffraction pattern, essentially undermining the Rietveld method to fit a model to y_i throughout 2θ . Preferred orientation arises from crystallites with a dominate directional axis of their shape, *e.g.* needle or platelet shaped orientating along that particular axis improving intensities of reflections arising from that direction and reducing intensity elsewhere. Usually preferred orientation is minimal for neutron diffraction because of the large sample size needed and the geometry of the setup further reduces any preferred orientation. Though for X-ray powder diffraction the

Chapter 3. Experimental Methods

sample size is smaller and the confinements of the sample holder can enhance a particular direction that the crystallites will orientate themselves in, this becomes more pronounced for needle or flat shaped crystallites.

In order to minimise this it is crucial to carefully pack a sample holder by a process which seek to minimise crystallite orientation or remove the effects. These include back-filing the sample holder, using crystallites of similar size, and the use of transmission geometry over flat plate Bragg-Bretano. Transmission gives an extra axis of rotation over a spinning flat-plate setup, improving the uniformity of the reflections. Unfortunately for jarosites, they sheer across the plane normal to the c -axis producing platelets and using acetone emulsion methods enhances the preferred orientation of the samples. This is removed by back filling, a process which improves the random distribution of the crystallites when placed in to a sample holder. Back filling is the process of filling an enlarged cavity between the sample holder and usually a glass microscope slide, the excess sample is retrieved. This method in effect increases the sample holder volume reducing the problems of confinement. Acetone slurries are useful for small amounts of sample; a small amount is placed upon the centre of a low background silica plate and a few drops of acetone is added to make a slurry. The acetone evaporates to leave a more uniform distribution of sample on the surface. This technique enhances preferred orientation because of the

Mathematically, this can be resolved using a simple axial system provided by March-Dollase [34] for cases of less severe preferred orientation where one or two axis can describe a particular direction as in the case of sample packing. The axes are modeled using ellipses which March [35] introduced and implemented using cylindrical symmetry by Dollase [34]. To analyze more pronounced preferred orientation or for texture analysis required by engineers to investigate stresses and strain in materials and for the analysis of grain boundaries, size and shape of minerals; a better mathematical description is using spherical harmonics. The mathematical implementation set out in GSAS by von Dreele for spherical harmonics is set out in equation (3.17)

$$y_{ci} = y_{bi} + \sum_h s_K |F_K|^2 G(\Delta\theta_{iK}) \quad (3.17)$$

Chapter 3. Experimental Methods

K is the correction factor for preferred orientation, it contains the texture function $A(b, y)$ that describes the change in intensity for each reflection. h is the reflection index and is comprised of a polar and azimuthal coordinate (φ, β) , y is the sample orientation and its polar and azimuthal coordinates are (ψ, γ) . The terms b and y are determined in equation (3.18)

$$A(\varphi, \beta, \psi, \gamma) = 1 + \sum_{l=2}^L 4\pi/(2l+1) \sum_{m=-l}^l \sum_{n=-l}^l C_l^{mm} k_l^m(\varphi, \beta) k_l^n(\psi, \gamma) \quad (3.18)$$

k_l^m and k_l^n are the crystal harmonic factors and C_l^{mm} are the harmonic coefficients. It is these factors which are refined by the least-squares method to generate the coefficients and texture values. The crystal harmonics for (ψ, γ) are defined by an instrument coordinate system (I, J, K) which are governed by Eulerian angles (Ω, X, Ψ) When carrying out the refinement the system is cylindrical, $\Omega = -90^\circ$ the other two angles are zero. Twelve terms of C_l^{mm} are used in the refinement of powder jarosite samples using laboratory X-ray equipment.

Thermal Displacement

Other important physical properties are also very necessary to refine, some are not refined until late into the refinement strategy. These include the temperature factor, B or U varies between refinement programs, atom position (x, y, z) and possibly site occupancy. It is expected after resolving the profile is to ensure that calculated peaks match the position for the observed peaks. This will involve lattice parameter refinement and any necessary refinement of the atom positions (x, y, z) . The last process in a refinement is to make sure calculated intensity match observed intensity. It may be possible that the wrong profile function is used or poorly implemented arising at a situation where the integrated intensity under a peak are equal for both y_i and y_{ci} , but the peak profiles do not match. Or simply some peaks may be stronger in intensity or weaker than others. This may be due to preferred orientation and hence why it is important to eliminate or minimise that effect as best possible. What remains are the displacement of electron density

Chapter 3. Experimental Methods

through thermal movement of the atoms. Changes in temperature, strength of the bonding and the symmetry for that crystallographic position will effect the displacement of an atom. The greater the displacement, the more diffuse and weaker the reflections are. This effect is noticed more in X-ray diffraction because X-rays are diffracted by electron density. In X-ray diffraction it is assumed that electron density accompanies the displacement of an atom and it considered to be a rigid body vibration.

Taking the Fourier transform of finding the probability of finding the centre of an atom $p(r')$ we derive the Debye-Waller factor

$$q(\mathbf{r}^*) = \int_{S'} p(r') \exp(2\pi i \mathbf{r}^* \cdot \mathbf{r}') d\mathbf{r}' \quad (3.19)$$

If the motion is isotropic - spherical symmetry - then it can be described by a Gaussian distribution,

$$p(r') \simeq (2\pi)^{-1/2} U^{-1/2} \exp[-(r'^2/2U)] \quad (3.20)$$

$U = \langle r'^2 \rangle$, the square mean shift of the atom about its position. r' is measured in Å.

The Fourier transform of (3.20) leads to the atomic temperature factor, B .

$$B = 8\pi^2 U (\text{Å}^2) \quad (3.21)$$

This is a very good value in relation to temperature, T , as proven by Debye through experimental work. It also explains why scattering become more diffuse with increasing $\sin \theta/\lambda$.

Goodness of Fit

Once the model is sufficiently close and all corrections are made, the process of the refinement is repeated improving the model continually by feedback, which is one of the important aspects of Rietveld refinement. In order to ascertain the quality of the fit of the calculated pattern with the observed data, there are many statistical routines to verify the criteria of fit. The primary check is looking at the

Chapter 3. Experimental Methods

χ^2 (Goodness of Fit) value upon minimising the residual (3.13) with respect to the number of profile points minus the number of refined parameters, the closer to the value 1 the better (1-1.3 is expected, anything above 1.7 and the model will need to be looked at), however, χ^2 can be rather crude and can be ignorant of correlations building up between the variables in the least-squares matrix.

$$\chi^2 = \sum_i W_i (y_i - y_{ci})^2 / (N - P) \quad (3.22)$$

N is the number of profile points and P is the number of refined parameters.

The most commonly quoted and used because its comparable to single crystal R values, is R_{wp} . This is not based upon observed Bragg intensities but, on from the model used in the refinement and is therefore biased to the model used. It is nonetheless the best available because it is the numerator that is being minimised and gives a good indication of how the refinement is progressing.

$$R_{wp} = \sqrt{\left[\frac{\sum_i W_i (y_i - y_{ci})^2}{\sum_i W_i y_i^2} \right]} \quad (3.23)$$

Both R_{ep} (3.23) and χ^2 (3.22) can be distorted and lead to misleading values. It is possible for χ^2 to fall below one or even negative. This should not occur because the summation in equation (A.2): if all the observations are independent resulting in the weight matrix (\mathbf{W}) being diagonal and the vales are the inverse of the variance of the observations, will be 1. To go below this value then there have to be more refined parameters than data collected. An artificially low value can be reached if the background is considerably raised as the background can be easily modeled or as a result of poor counting statistics. There has been one recently added statistical routine that watches out for any build up of correlations throughout a refinement [36]. This is the Durbin-Watson statistic, d , which should have an ideal value of 2.00

$$d = \frac{\sum_{i=2}^N (\Delta y_i - \Delta y_{i-1})^2}{\sum_{i=2}^N \Delta y_i^2} \quad (3.24)$$

Generally throughout a refinement d will start small and increase towards 2.00, showing how the model and observed intensities are providing a closer fit and is

Chapter 3. Experimental Methods

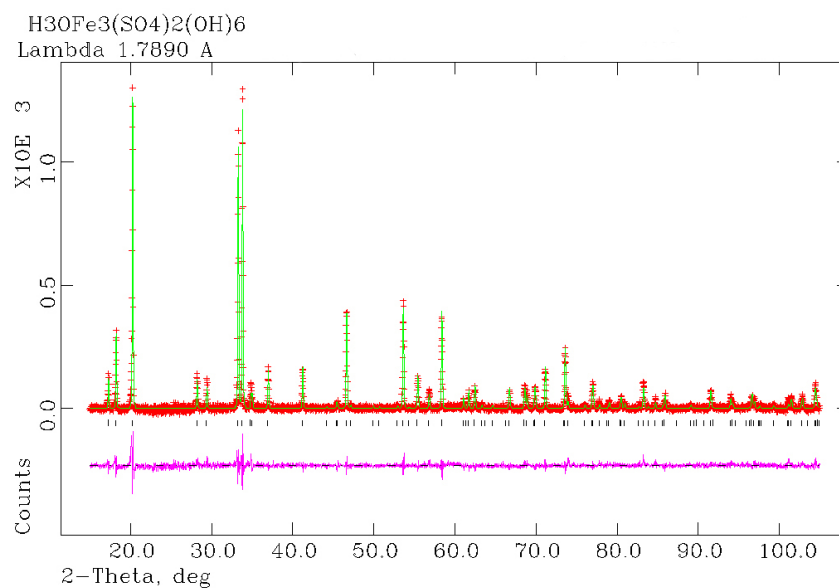
a good method to determine how good the model Bragg intensities match those of the observed Bragg intensities, which is less biased than R_{wp} . Though d might always fall short of 2.00 because of non-statistical errors.

Completion of Rietveld Refinement

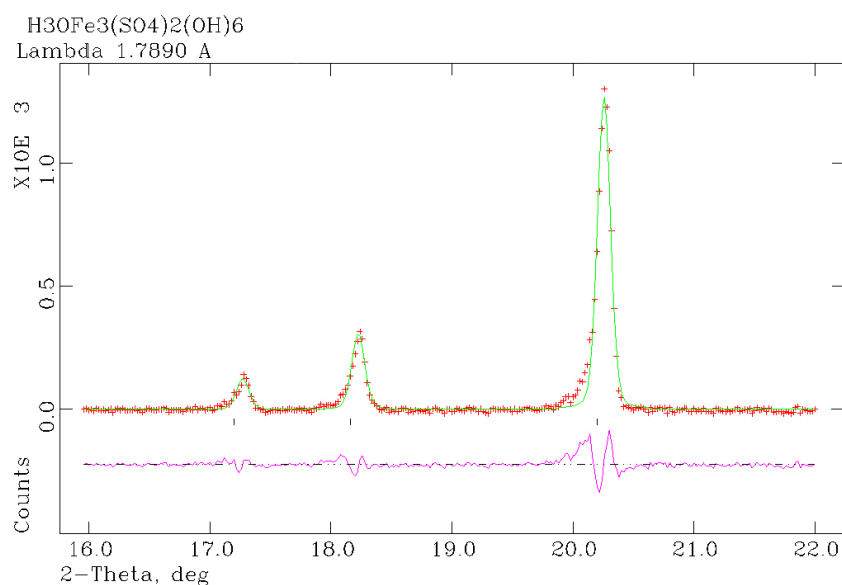
The best method of determining whether the fit is satisfactory is by carefully looking at the graphical output. All Rietveld programs provide graphical outputs to view and compare the calculated powder pattern from the model and the observed powder pattern. The human eye is very good at differentiating between Lorentzian and Gaussian distributions as well as spotting more obvious failures in the refinement model. Visualising the refinement fit also allows the user to interpret why the model fails to match the observed through scientific judgement and detecting systematic errors that have occurred but can not be modeled successfully. This becomes apparent with modern X-ray diffractometers where the Caglioti (3.15) might not be sufficient to adequately describe the radiation profile resulting from the complex optics and improved data collection instrumentation. The resolution of such instruments is improving, that the asymmetry arising from axial divergence increases or becomes more pronounced and in some cases the new generation of position sensitive detectors (PSD) using a strip of semi conductors with a small separation between each, which in effect creates several diffractometers adds to the low angle asymmetry. Unfortunately many Rietveld codes are not fully capable off modeling such extremes of asymmetry.

It is important to gain knowledge of the quality of the fit as this will impact upon the accuracy and precision of the values of the refined parameters obtained from the refinement. The estimated standard deviations (*e.s.d.*'s) produced are not a result of experimental error, but only the minimum error on the random variables used in the least squares matrix. Therefore systematic errors; 2θ offset, sample roughness, absorption, etc, will not appear in the *e.s.d.*'s only if the model is poor will that affect the *e.s.d.*'s. Improvements upon the *e.s.d.*'s are increases in resolution which help define peak positions and profiles more accurately and remove overlapping of peaks and thus improving the precision of the result. Accuracy can not be guaranteed for poor experimental setup.

Chapter 3. Experimental Methods



(a) Rietveld refinement showing the entire diffraction pattern.



(b) Rietveld refinement of the same diffraction as above, but focused at low angle highlighting the appearance of asymmetry.

Figure 3.11: Two plots of the same pattern (a) is the full pattern and (b) highlights at low angle the asymmetry that can result from axial divergence from high resolution X-ray diffractometers. The drop in form factor for X-rays can clearly be seen in (a), though collection to high 2θ provides accurate lattice parameters. The green line represents the model, the red crosses are the individual data points and the purple line is the difference between the model and the data.

3.9 Single Crystal Diffraction

Single crystal diffraction is far superior to powder for structure solution because of the greater number of independent reflections obtainable and with minimal overlap of reflections, space group determination becomes almost trivial certainly for higher symmetry systems.

3.9.1 Data collection techniques

Single crystal X-ray diffraction was carried out the National Crystallographic Service based at Southampton University in collaboration with Bill Clegg at Daresbury station 9.8. Most data sets were collected at Southampton which has two identical single crystal diffractometers (Dell boy and Damien) side by side.

Suitable crystals were selected using a light microscope fitted with two polarized filters. Crystal quality is tested by viewing the transmission of polarized light through the crystal. The result of the extinction phenomenon is that a single crystal (with the exception of cubic crystal classes) will transmit polarized light along at least one axis, upon rotation of 90° the crystal should appear opaque if it is a true single crystal. The size of crystal varied between $20\text{-}50\ \mu\text{m}$ across a face. Each crystal was mounted upon a glass fibre and affixed using adhesive. The crystal was aligned using an automated process controlled by software. X-Rays (MoK α , $\lambda=0.71073\ \text{\AA}$) were generated using a Bruker-Nonius FR591 rotating anode and collected on a four axes Bruker-Nonius 95mm KappaCCD camera on a k-goniostat. The sphere of diffraction from $2.91^\circ < \theta < 27.48^\circ$ was collected at room temperature and $\sim 80\text{K}$ using an Oxford Cryosystems cryostream 700 series. The crystal-to-detector distance was 30.00 mm with a resolution range of $7.00\text{-}0.77\ \text{\AA}$. Position and peak intensities were extracted from the raw data using DENZO SMN and scaled using SCALEPACK; SADABS V2.10 [?] was used for adsorption correction.

Adsorption corrections are very important for single crystal diffraction, unlike in a powder where adsorption corrections are made for the bulk of the sample. In powder X-ray diffraction longer wavelength X-rays will be absorb more, whereas in neutron powder diffraction, it is the sheer bulk quantity of sample needed that

Chapter 3. Experimental Methods

will give rise to absorption. In single crystal diffraction the size and shape, and the path the X-rays travel through the crystal are important (extinction) and thus adsorption corrections are very important. The jarosite crystals are pseudo cubes and thus scattering is near to uniform throughout the crystal, the only consideration is size. The crystals themselves are fairly small (30-100 μm across a face) and thus extinction is minimal and adsorption is small.

All data was collected in P1 rather than trigonal to ensure all reflections were collected or to confirm that there was no lower symmetry present but more importantly it was determined that allowing SHELX-97 to merge the data rather than SCALEPACK produced more consistent results.

3.9.2 Structure solution

XPREP was used for initial unit cell refinement and space group determination and to generate a SHELX input file. SHELX-97 [?], executed under WinGX V1.7 [37], was used for structure solution and refinement and only the atomic structure factors of Shelx-97 were used.

There were two methods used for structure solution; direct methods and Patterson methods. All but a few samples were refined using direct methods and a few structures were solved using the Patterson method. Direct methods concentrate on solving the phase problem, where as Patterson tries to obtain information on atom position and thus making a better approximation for the contributing phases.

For a greater description on structure solution and methods used please refer to the Crystallography Appendix.

In practice the crystal structure was solved and initially refined in $R\bar{3}$ because good values of conformity of fit were obtained from the initial structure solution.

Refinement

Refinement in Shelx-97 is undertaken using least-squares minimisation, instead the refinement is carried out against F^2 which ensures a more accurate result as better standard deviations can be obtained, $\sigma(F_0^2)$, but is computationally more extensive. This leads to an $R1$ factor (3.25) twice than that for R_{wp} in a Rietveld refinement (3.23).

Chapter 3. Experimental Methods

$$R1 = \left(\frac{\sum [w(F_0^2 - F_c^2)]^2}{\sum w[F_0^2]^2} \right)^{\frac{1}{2}} \quad (3.25)$$

The Goodness of fit, also based upon F^2 , is shown in equation (3.26),

$$Goff = \left(\frac{\sum [w(F_0^2 - F_c^2)]^2}{n - p} \right)^{\frac{1}{2}} \quad (3.26)$$

where n is the number of reflections and p is number of parameters refined.

After the initial refinement was concluded which involved; positional parameters and isotropic displacement for all atoms, the symmetry of the system was checked using PLATON V40M [?, 38]. The ADDSYM function of PLATON confirmed the presence of a mirror plane and the symmetry was increased to $R\bar{3}m$ for the final structure refinement which included anisotropic displacement for all atoms except the hydroxyl hydrogen. The hydrogens on the (H_3O^+) ion could not be satisfactorily located. The Shelx input file had to be modified after using PLATON to remove any legacy Shelx-86 lines that PLATON would add, in particular PLATON added its own atomic structure factors, however minor the difference, this did affect the final refinement and atomic positions.

Chapter 4

Iron jarosites $S = \frac{5}{2}$

4.1 Chemistry and Synthesis

Jarosites are notoriously difficult to break down in solution, they are impervious to very strong acids and dissolution is slow under high pH. Jarosite can only be formed in a pH range of 0.8 - 1.8 [8] Higher pH will result in the formation of Goethite and Haematite, a lower pH, in the formation of unwanted amorphous iron oxyhydroxy sulphates. In nature, jarosites occur through the weathering process of Pyrite, FeS high concentrations of Fe²⁺ released from the dissolution of FeS decreases the pH of the local water area and through either microbial action or dissolved oxygen oxidises Fe²⁺ to Fe³⁺. Around these Fe³⁺ centres, chains of hydroxysulphates attach themselves to form the characteristic iron flocs. Extremely low values of pH and the incorporation of a suitably sized cation will cause jarosite precipitation with the following formula: $A_{1-x}(H_3O)_xFe_{3-y}(SO_4)_2(OH)_{6-3y}(H_2O)_{3y}$, where $A=K^+, Na^+, Ag^+, Rb^+, NH_4^+, H_3O^+, Pb^{2+}, Tl^{2+}$. The high water content and the low temperature formation conditions in nature can lead to a large deviation from the ideal stoichiometry. Naturally occurring jarosites may be charge balanced by the incorporation of other cations in the B site which are not 3+ cations, such as copper or zinc leading to the formation of other minerals. If there are Fe deficiencies, charge balancing requires the replacement of an A-site with a H₂O unit or protonation of the bridging OH. Likewise, increasing incorporation of water the charge of structure will be balanced by Fe vacancies [8, 39, 40].

This unstoichiometric nature has major implications for the magnetism of the jarosite structure. If the basic triangular Fe unit throughout the *kagomé* is diluted with Fe vacancies then the geometric arrangement of the ions producing the magnetic frustration is lost and eventually the bulk will not display magnetically frustrated properties. The magnetic percolation limit in jarosites investigated by numerical studies or experimentation either suggests a remarkably robustness to disorder or minimal dilution that will destroy the frustrated manifold and as such the need to produce near 100% Fe coverage is crucial for research [21,28].

They have been many methods to produce jarosites synthetically to investigate and exploit this unstoichiometric nature [6,8,39]. Primarily researched for mining purposes to either remove unwanted elements or to ensure the desired elements are not absorbed by the jarosite structure [6,8,39,41], which forms during the hot acid leaching process.

4.1.1 Hydrothermal Methods(1) - Forced hydrolysis

Highlighted above, jarosites form naturally in ambient conditions and can be synthesized in the laboratory very simply using boiling water (98°C) [8]. However, there is little or no control on the stoichiometry and quality of the crystalline structure. Another drawback of sub 100°C reactions is inability make hydronium jarosite [8], perhaps the most important jarosite in terms of its magnetic properties [42, 43]. Magnetically, hydronium jarosite is the most interesting jarosite because it undergoes a spin glass transition [43] as a result of the frustrated manifold whereas all other jarosites eventually undergo long range Néel order [28,42,44].

Typically in the reported literature jarosite synthesis uses 0.1-0.275M solution of $\text{Fe}_2(\text{SO}_4)_3 \cdot 5\text{H}_2\text{O}$ with the required A-site in a 3:1 ratio A-site: $\text{Fe}_2(\text{SO}_4)_3 \cdot 5\text{H}_2\text{O}$, reverse of the general formula to minimize competition from H_3O^+ ions for the A-site. The pH adjusted with either the addition of concentrated sulphuric acid to reduce the pH to below 1.8 or LiOH to increase to the pH to 1.6. The solution is heated at 100-150°C in an PTFE lined steel bomb [8, 28] (usually a Parr design) or a titanium baffled autoclave [20, 21] for 8-72 hours. The solution is decanted off to leave behind the jarosite which is washed with distilled water several times before dried in an oven at 110-120°C for at least 4 hours. Yield increases with

increasing temperature, longer reaction time and higher concentration. For hydronium jarosite synthesis where there are no other A-site sulphates present there is a presumed assumption of a high H_3O^+ occupation in the A-site. Our research shows that PTFE lined bombs reduce the crystal size. The use of baffles or stirring will destroy the crystallinity of the jarosite product: although they have a high density they are soft. Far greater yields are achieved for non-hydronium jarosite compared to hydronium jarosite synthesis for similar conditions.

Non-hydronium jarosites

Synthesis conditions and yields for non-hydronium jarosites are shown in Table 4.1. In some cases LiOH was needed to adjust the pH if necessary and some A-site hydroxide salts were used: synthesizing Na-jarosite requires NaOH. A range of A-site salt concentrations were used to allow competition with the H_3O^+ ion for the A-site and to alter the magnetic transition temperature.

Unfortunately the quality of crystals from the jarosites formed in Table 4.1 were too small for single crystal analysis and another method has to be sort for larger crystals. Altering the A-site concentrations as shown in Table 4.1 alters the magnetic transition within a given A-site jarosite, thus proving and nonetheless hydrothermal synthesis preparation of non-hydronium jarosites have been important for understanding the magnetic behaviour.

Forced hydrolysis - hydronium jarosites

One mechanism to enhance the quality of jarosite precipitation is the use of forced hydrolysis conditions. [21,45,46]. The jarosite reaction is a hydrolysis reaction [47], with the pH continually dropping as more and more jarosite precipitation occurs [47]. The mechanism of the jarosite reaction is discussed in jarosite reaction mechanism subsection ???. Hydrothermal techniques increase the hydrolysis potential of jarosite precipitation and allow stabilisation of the jarosite precursor during synthesis [40,48] discussed further in the jarosite mechanism subsection ???. Forced hydrolysis conditions uses very high concentrations of $\text{Fe}_2(\text{SO}_4)_3$ and any appropriate A site - sulphate. Dutrizac [8] specified using 3:1 ratio of A-site sulphate to $\text{Fe}_2(\text{SO}_4)_3$ to minimize competition from the H_3O^+ ion and Kubisz [39] suggested

Table 4.1: Synthesis conditions for non-hydronium jarosites using hydrothermal techniques all solutions were made up to 15cm³ of H₂O.

A-site SO ₄ /OH	A ⁺ M	Fe ³⁺ M	Temp. (°C)	time (hrs)	yield (g)
KOH [†]	0.202	0.55	110	68	1.1545
K ₂ SO ₄	0.3	0.275	110	48	0.6933
K ₂ SO ₄	0.2	0.55	130	21	1.3091
K ₂ SO ₄	0.0925	0.55	130	21	0.905
KOH	0.339	0.55	130	21	1.3342
KOH	0.148	0.55	130	21	1.1341
NaOH [§]	0.330	0.55	130	21	1.186
NaOH [§]	0.120	0.55	130	21	0.926
Ag ₂ SO ₄	0.400	0.55	140	21	1.121
Ag ₂ SO ₄ [‡]	0.16	0.55	130	21	1.2449
Rb ₂ SO ₄	0.42	0.55	130	21	1.1340
Rb ₂ SO ₄	0.25	0.55	130	21	1.0441
(NH ₄) ₂ SO ₄	0.33	0.55	130	21	0.931
(NH ₄) ₂ SO ₄ [†]	0.33	0.55	130	21	1.113
(NH ₄) ₂ SO ₄ [†]	0.11	0.55	130	21	1.029

[†] pH adjusted with LiOH to bring the starting pH above 1.6

[§] Sodium jarosite could only be successfully be synthesised using NaOH

[‡] Contains impurities, Ag₂SO₄ and Ag

the use of A-site hydroxides instead as this improves the Fe:SO₄ ratio (2:3) and improves the A-site stoichiometry [49]. Certainly for sodium jarosite preparation the use of NaOH produces far better quality jarosite. In some of the reactions the pH was adjusted using LiOH to increase the pH range to be between 1.6–1.8; Li⁺ ions are not incorporated into the jarosite structure [50]. Hydrothermal synthesis is the only means to synthesize hydronium jarosite [8]. Existing hydrothermal techniques use PTFE lined steel bombs or titanium baffled bombs [51] and in combination with stirring [20]; my research showed poor quality jarosites with lower yields are produced using PTFE lined steel bombs, and any stirring will destroy the crystallinity of the jarosites due to their softness.

The hydrothermal technique for jarosite formation was a great success for synthesizing hydronium jarosite. Modifying the technique, outlined below, allowed for greater crystal growth as well as being able to manipulate the magnetic transitions

of hydronium jarosites. There are many improvements upon synthesis methods to increase crystal size, yield and believed improved stoichiometry. One method was the modified method of Earle *et al* [21] using Pyrex tubes.

The use of a Pyrex surface enabled greater yields and a better surface for crystal growth producing regular pseudo cubic crystals with a size of 30-50 μm across a face of hydronium jarosite. The angle of elevation of the Pyrex tubes also dictates the single crystal growth. Maintaining the tube in an upright position destroys or limits single crystal growth because the crystal growth requires a surface to along and the relatively high density of jarosite means after a certain size the crystallites will fall and collect at the bottom poorly formed.

Using 100% H_2O as the solvent for hydronium jarosites synthesis, the greatest yield and the largest and most numerate pseudo cubes (up to $\sim 150 \mu\text{m}$ across a face) form at 150°C . Greater temperatures result in the formation of hematite. Lowering the temperature reduces yield and quality of crystals. Crystal quality reduces with lowering temperatures because at temperatures below 145°C the crystal growth stalls at the stage where the sheets of interlinking pseudo cubes that grow up the side of the Pyrex tube, the individual pseudo cubes have not reached a sufficient size to fall away intact from the sheet. Instead upon cooling the sheets break apart and fracture many of the individual pseudo cubes in the process. Higher temperatures insure the formation of larger individual crystals and produce a much darker brown/ochre colour, whereas poorer formed crystals are lighter in colour.

SEM results for 100% H_2O solvent hydronium jarosites

Scanning electron microscopy (SEM) images using the Joel F???? in Figure 4.1 show improvement in crystal formation with increasing temperature.

Jarosite growth under hydrothermal synthesis conditions is a thermodynamic process of Ostwald ripening [47]. Nucleation sites of precursors for jarosites and unwanted phases of Fe oxy-hydroxy sulphates exist simultaneously from the start of the reaction. Over time, the thermodynamically favourable jarosite structure grows at the expense of the kinetically favourable amorphous Fe oxy-hydroxy sulphate phases, which dissolve and add to the crystal growth of the jarosites. Figure 4.2 highlights the influence of time upon jarosite formation. Insufficient time produces

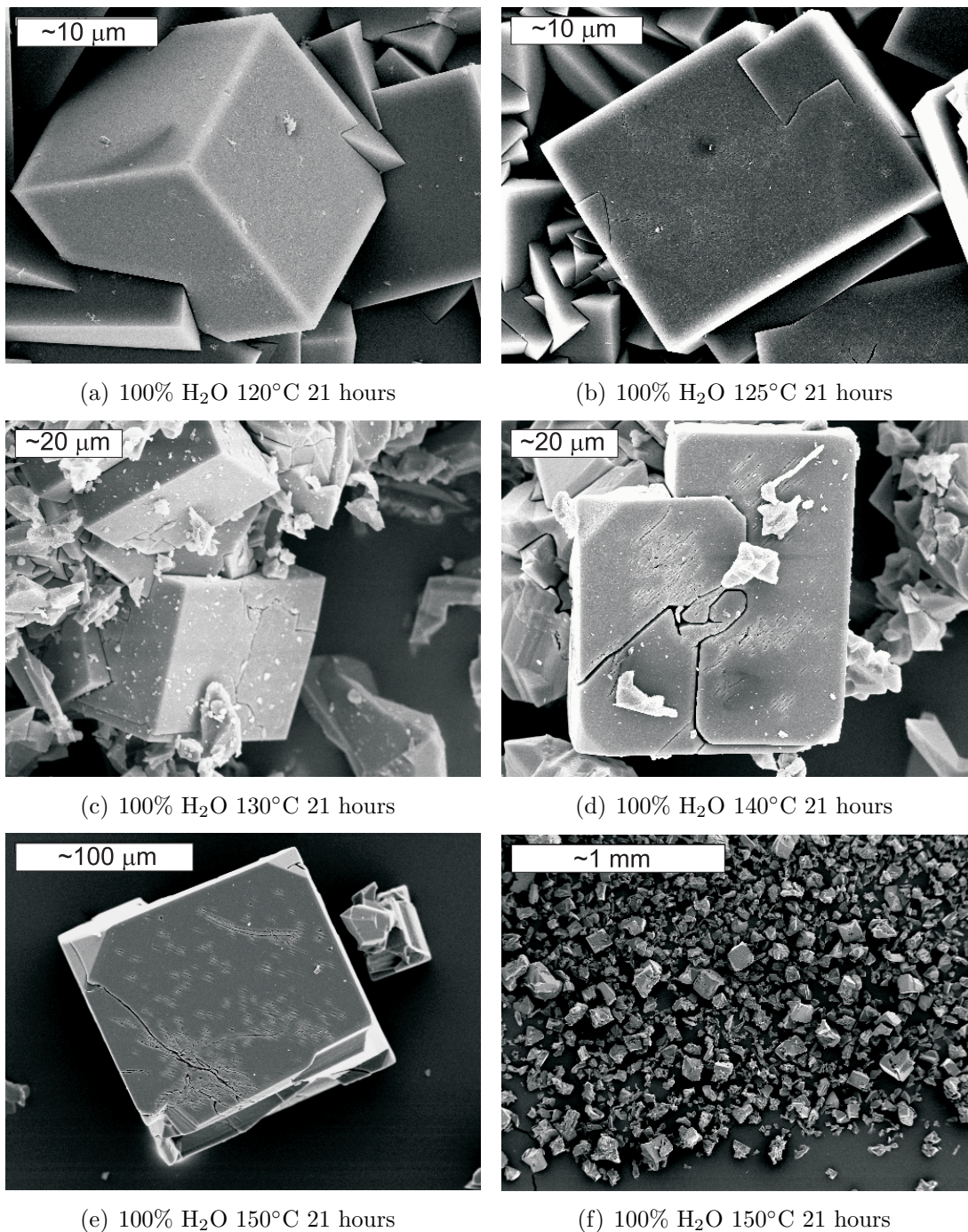


Figure 4.1: increasing temperature improves the size, quality and quantity of hydronium jarosite crystals using $100\% \text{ H}_2\text{O}$ as a solvent.

few and only poorly formed jarosite crystals in amongst a multitude of precursor nucleation sites. After 15 hours, regular sized pseudo cubes of jarosite are produced, though plenty of precursor debris still remains. Increasing reaction time produces larger crystals and less jarosite debris. After a longer time period, most debris comes from broken jarosite crystals rather than remnant nucleations sites. The beginning of pitting can be seen on the face of the pseudo cubes at 15 hours and this becomes more pronounced with striations appearing regularly across the faces and even crystal deformation with increasing time. The pitting and striations result from the ever decreasing pH levels, such acidic conditions etch at the surface, firstly stripping out the A-site (H_3O^+) [52]. Continued etching leaves triangular shaped holes revealing the trigonal crystal class of jarosites underneath the pseudo cube veneer. A reaction time of 21 hours was decided as a good balance between crystal growth, ensuring phase pure samples and efficiency of synthesis. Magnetic sample measurements later confirmed that reaction times greater than 15 hours did not affect the magnetic susceptibility of jarosites formed under identical temperatures using 100% H_2O as the solvent. This reaction time was then applied to all further jarosite production to ensure consistency.

SEM results for MeOH/ H_2O solvent mix hydronium jarosites

Introduction of MeOH as a solvent increases the effective temperature of the reaction and can radically change the nucleation and subsequent jarosite crystal growth. For similar reaction temperatures where one reaction contains 100% H_2O as a solvent and the other solvent a mixture of H_2O and MeOH, greater yields are achieved with increasing MeOH concentration. There is a limit to MeOH concentration. No jarosite can be made with a MeOH concentration of 90% or greater under hydrothermal conditions. This limit decreases with increasing temperature reaching 50/50 H_2O /MeOH mix at 150°C. Higher MeOH concentrations produce unwanted iron oxyhydroxy sulphates at lower temperatures it drives the system to form Schwertmannite bottom of Figure 4.3. At intermediate temperatures of 130°C, the morphology of jarosite changes again to form interpenetrating triangular prisms, leading to the formation of Schwertmannite at higher MeOH concentrations Figure 4.4, 4.4(f). Continued increase in temperature causes mottling of the pseudo cubes

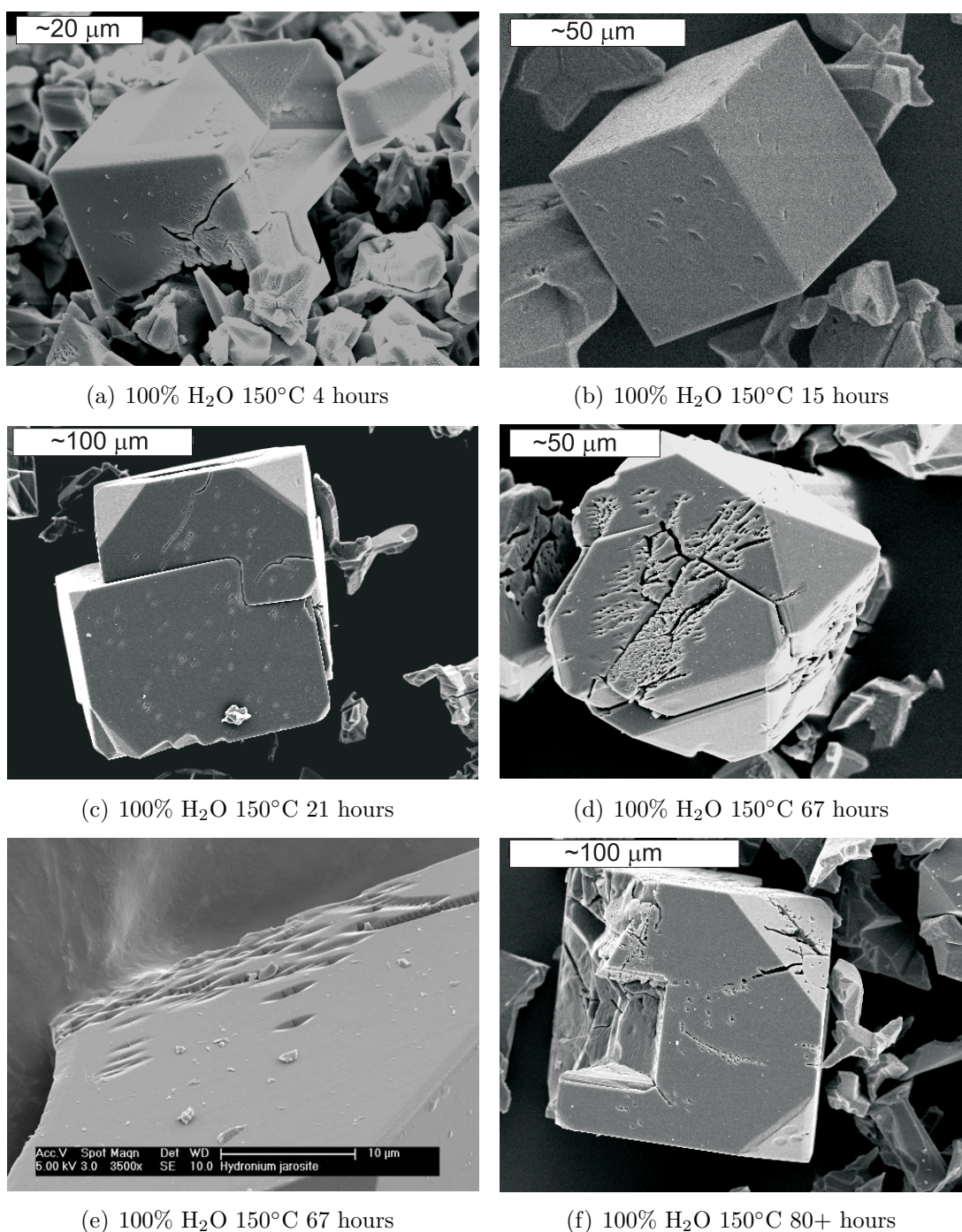


Figure 4.2: increasing reaction time improves the size of the jarosite crystals and reduction in precursor debris when using 100% H₂O as a solvent. The pH falls with increasing reaction time and in these conditions the surface is attacked pitting the surface with triangular holes. The reaction time is a balance to ensure no remaining unknown precursor material is left and good sized well formed crystals - decided to be 21 hours

of jarosite and produces unwanted X-ray diffraction amorphous Fe oxy-hydroxy sulphates shown by their needle like structure in Figure 4.5.

4.1.2 Hydrothermal Methods (2) - Oxidative synthesis

Table 4.2: Synthesis conditions for non-hydronium jarosites using the oxidative technique; all reactions were carried at 170°C for 48 hours

A-site sulphate	mass per 25cm ³ of H ₂ O	Molar concentration	yield (g)
K	2.44g	0.56	0.100
Na	0.85g	0.24	0.066
Rb	3.75g	0.56	0.0486
NH ₄	1.85g	0.56	0.697
Ag [†]	4.38g	0.56	1.67

In comparison with K-Jarosite, formation of the other A-site jarosites was more difficult. Phase pure rubidium jarosite was not achieved; hematite, which was always present, was decanted away during washing, its density being significantly less than that of rubidium jarosite. Silver sulphate – which is very insoluble – created a problem when retrieving the product as a large amount still remained undissolved or precipitated back out upon cooling. This was eventually removed by dissolving the residue silver sulphate with a large quantity of water and a highly dilute concentration of NH_3 stirred on stirrer plate. After successful washes, solid silver residue remained – removed with tweezers – and hematite, which due to its low density was decanted off during the successive washes. All remaining iron wire was removed using a stirrer flea magnet during the wash process for all the jarosites formed using the oxidative method and the remaining Fe wire was weighed, though accurate measurements could not be determined due to the loss of Fe during the washing and removal process. The remaining amount of Fe was consistent throughout all the reactions where a product appeared, whether it be hematite or jarosite product proper, usually between 0.008g-0.02g. This suggests that the reaction has several steps towards making jarosite, distinct from the non-oxidative forced hydrolysis synthesis.

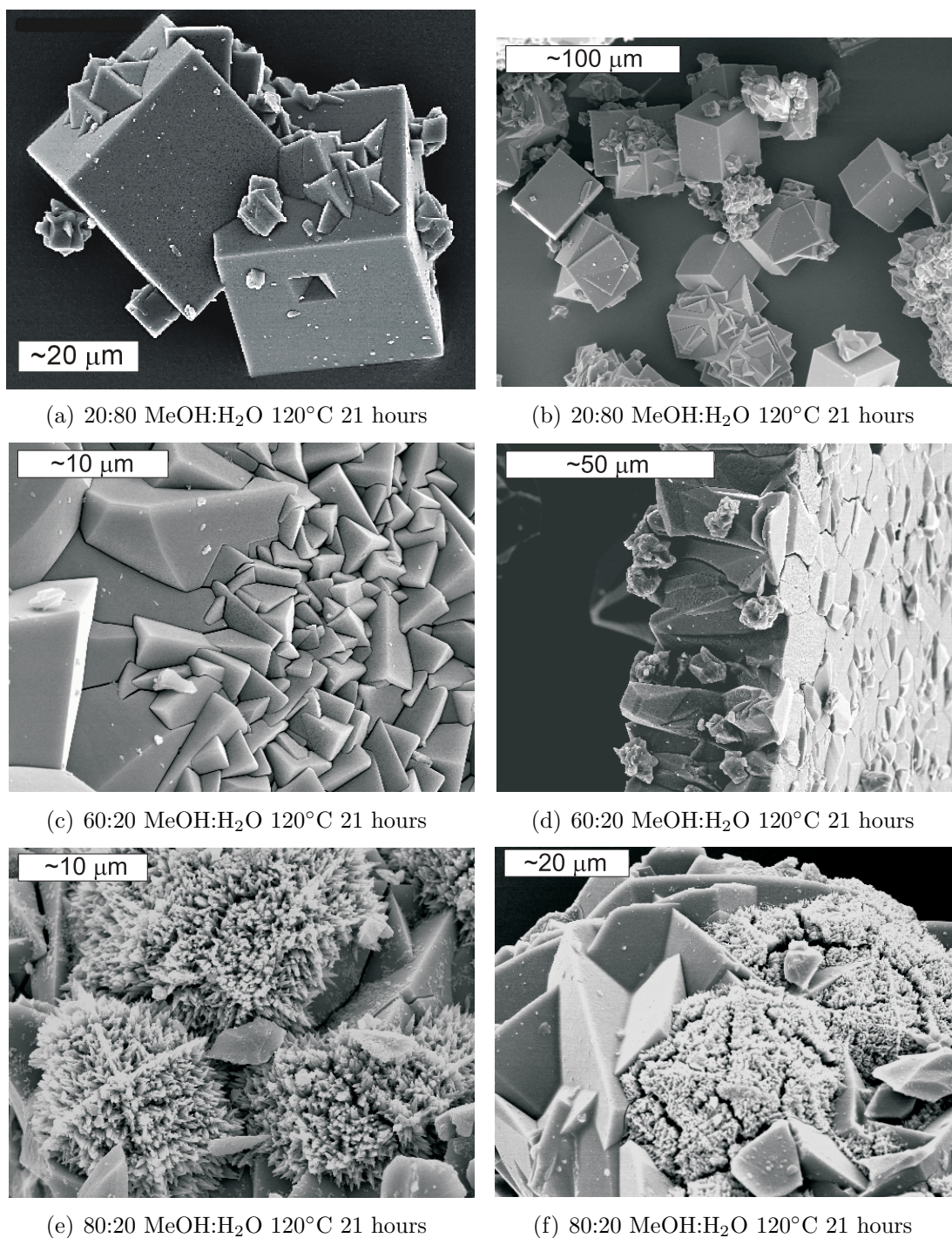
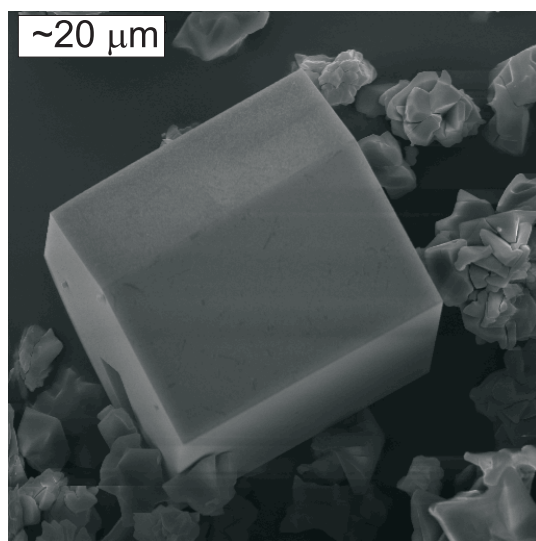
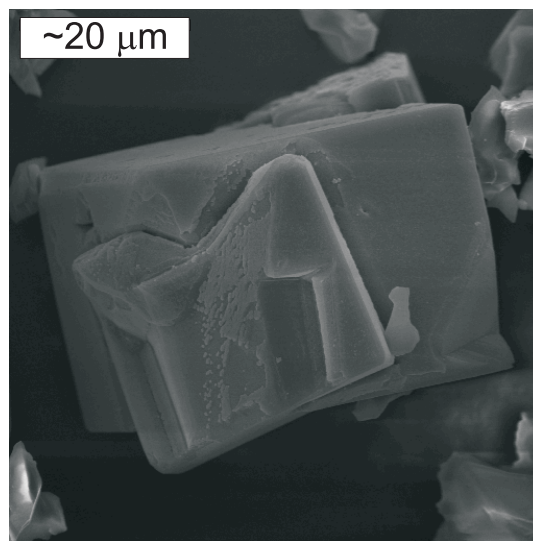


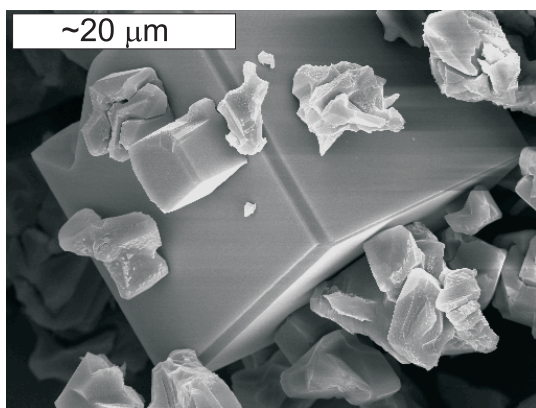
Figure 4.3: The SEM images of various H₂O/MeOH mixses at 120°C show how low concentrations of MeOH increase the effective temperature of jarosite formation and produce large single crystals - though an increase in twinning, interpenetrating crystals and stacking faults due to rapid crystal growth possibly centred on the inversion centre. High concentrations eventually leads to unwanted Fe oxy-hydroxy sulphates as shown by the occurrence of Schwertmannite (corel-like appearance)



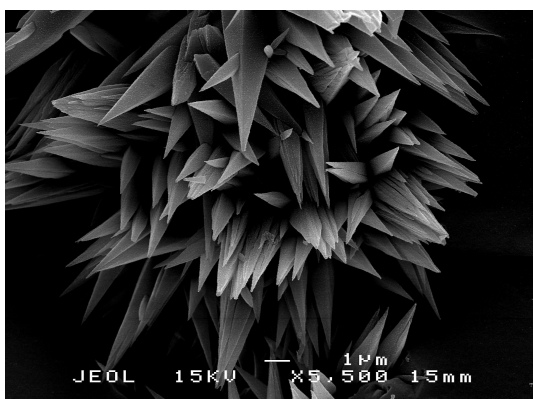
(a) 30:70 MeOH:H₂O 130°C 21 hours



(b) 30:70 MeOH:H₂O 140°C 21 hours



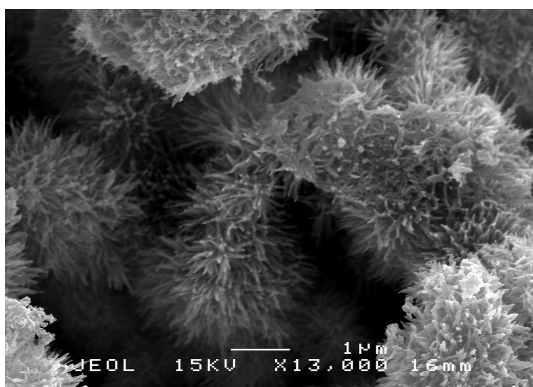
(c) 30:70 MeOH:H₂O 150°C 21 hours



(d) 70:30 MeOH:H₂O 150°C 21 hours



(e) 80:20 MeOH:H₂O 150°C 21 hours



(f) Schwertmannite

Figure 4.4: SEM images of various H₂O/MeOH mixses between 130-150°C to show how higher concentrations coupled with an increase in temperature causes changes to the crystal growth. At high temperatures with high concentrations of MeOH, mottling of the pseudo cubes occurs to the formation of unwanted Fe oxyhydroxy sulphates as shown by the occurrence of needle like structures. At lower temperatures high concentrations of MeOH produce interpenetrating triangular prisms, even producing fetching formations shown in the purple tinted picture.

4.1.3 Synthesis of Fe jarosite Samples for Neutron Diffraction

Deuterated Fe samples were made using Mikasaite as the source of iron sulphate. Deuterated mikasaite was made by completely dehydrating $\text{Fe}_2(\text{SO}_4)_3 \cdot 5\text{H}_2\text{O}$. To prepare, a stock $\text{Fe}_2(\text{SO}_4)_3 \cdot \text{H}_2\text{O}$ was washed with D_2O and the H_2O was rotary evaporated off, the process was repeated twice more to ensure removal of D_2O in subsequent washes. Towards the end of rotary evaporation remained a thick syrupy liquid, which was poured onto a large watch glass and dried in an oven ($120\text{-}150^\circ\text{C}$) to become anhydrous until a white/pink solid remains.

The quantities required meant many samples were made in a batch process and amalgamated together - refer to Table 4.3 for further details. All the solutions were made up for the required volume for the combined number of Pyrex tubes needed in each batch. Each batch was processed together throughout the whole reaction. In keeping with the oxidative method the relevant concentration of D_2SO_4 (1.1cm^3 added per 25cm^3 solution) was added.

Table 4.3: Synthesis conditions for deuterated jarosites using either the oxidative technique (Fe wire) or forced hydrolysis (Mikasaite). The mass shown for the Fe wire is the amount averaged between each Pyrex tube.

jarosite	A ⁺ M	Fe wire(g)	Mikasaite Fe ³⁺ M	Batch	Temp. [°] C	time(hrs)	yield(g)
D ₃ O	n/a	n/a	0.675	4x25ml	150	21	1.99
K	0.244	n/a	0.675	2x25ml	150	21	4.05
K	0.56	0.333	n/a	4x25ml	170	24	0.4
K	0.56	0.28	n/a	7x25ml	170	24	0.622
K	0.56	0.333	n/a	7x25ml	170	24	0.562
ND ₄	0.65	0.165	n/a	5x15ml	170	24	0.079
ND ₄	0.56	n/a	0.675	3x15ml	150	21	3.797

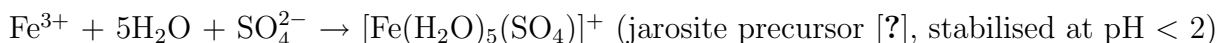
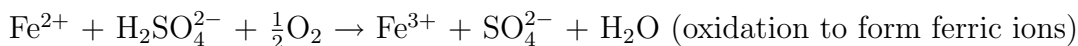
The yields from using Mikasaite show an interesting pattern. That is deuterium oxonium jarosite is less preferred than hydronium jarosite, yet enhances the yield for non-hydronium jarosites.

4.1.4 Mechanism for Jarosite formation

The synthesis of jarosite through the two methods, forced hydrolysis and hydrothermal oxidative synthesis, shows there are two distinct mechanisms behind the formation of jarosite.

Hydrolysis and forced hydrolysis

As previously discussed, Jarosite formation requires very low pH aqueous conditions and in nature usually starts from the dissolution of Pyrite (FeS) to provide a source of Fe^{2+} and SO_4^{2-} ions [53]. In low temperature regimes such as rivers and streams then the process of oxidizing Fe^{2+} to Fe^{3+} and subsequent jarosite formation happens via microbial action [47] and dissolved oxygen. Chains of hydroxysulphates form around the Fe^{3+} centres producing characteristic iron flocs [54]. Jarosite precipitation occurs when the pH falls below <2 and a suitably sized cation is present [46, 47]. The chemical reactions which describe this are shown below.



The reaction is self generating through hydrolysis by reducing the pH further continuing to stabilise the jarosite precursor material promoting jarosite precipitation.

Influence of pH

The key factor in all jarosite reactions is the pH. Control of the pH is crucial, for it determines the reaction pathway and nucleation and subsequent crystal growth. There are two Fe^{3+} precursor species $[\text{Fe}(\text{H}_2\text{O})_5(\text{OH})]^{2+}$ and $[\text{Fe}(\text{H}_2\text{O})_5(\text{SO}_4)]^+$, the latter being the jarosite precursor. A higher pH favours the former species [45, 47], whereas a lower pH, which continues to drop as further jarosite precipitation occurs, the latter species is preferred. The growth of jarosite follows a process of

Ostwald Ripening [55], this a balance between kinetic and thermodynamic forces in the reaction. The kinetic process of nucleation happens rapidly and in a jarosite precipitation many nucleation sites may occur, though many of these will not be necessarily be jarosite precursors. Instead, over time with ever decreasing pH levels, the less thermodynamically stable smaller nucleation sites will be dissolved because of the higher surface energies of a nucleation particle in comparison to a larger jarosite crystal, stabilised by the low pH conditions. The material from dissolved nucleation sites will be eventually added on to the growing surface of the small jarosite crystals. The greater thermodynamic stability of jarosites, because of the smaller surface area to volume ratio and the lowering of the internal energy because a bulk crystal structure ensures jarosite formation eventually succeeds at the expense of other iron oxy-hydroxy sulphates. Hence why time is necessary to form high quality jarosite crystals. Though this only appears to work for hydronium jarosites under hydrothermal conditions. Non-hydronium jarosite crystals do not grow as much as hydronium jarosite crystals using the hydrothermal methods outlined in this experimental chapter, because the absorption of a counter ion such as potassium probably reduces the surface energy of the growing crystal. The uniform charge and an ideal ionic radius to fit into the 12 coordinate between the T-A-T sheetings of the jarosite (Figure 1.1 a) helps to reduce the surface energy and hinders any further growth.

The influence of MeOH

The introduction of methanol as a solvent changes radically the balance between kinetic and thermodynamic energies in the reaction. Greater concentration of MeOH initially reduces the pH of the starting reaction, however it allows for more rapid nucleation and greater quantity of nucleation sites. This means that more jarosite precursor will be present, but also other unwanted iron oxy-hydroxy sulphates. The speed of crystal growth, increased twinning (Figure 4.3(a) 4.3(b)) and greater yields all highlight the raised kinetic energies the reaction. As has been highlighted in Figure 4.5 high concentrations of MeOH coupled with high temperatures produce unwanted iron oxy-hydroxy phases.

The addition of high concentration of MeOH pushes the reaction pathway away

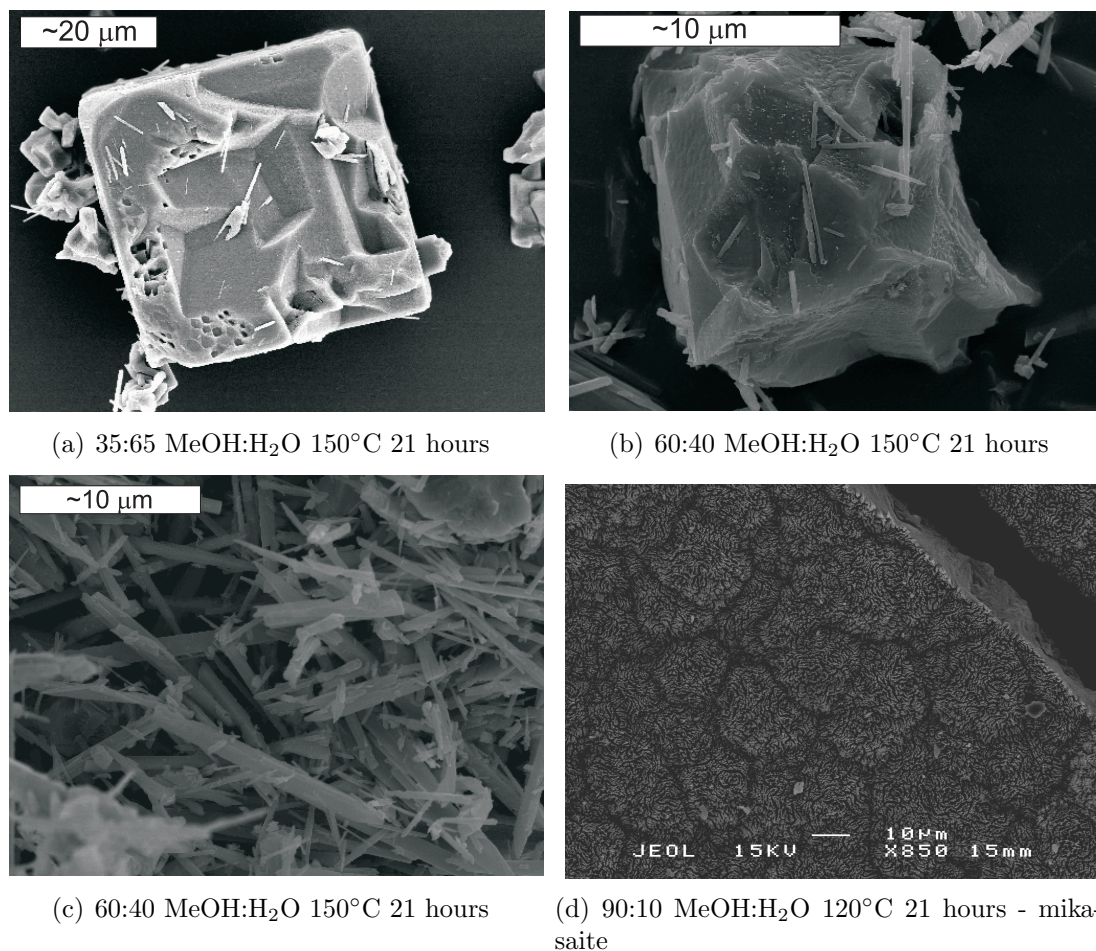
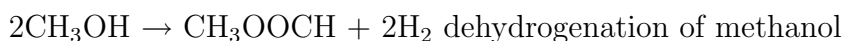


Figure 4.5: Showing how high methanol concentration combined with high temperatures favours the growth of amorphous iron oxy-hydroxy sulphate phases. Figure (a) shows a slight mottling occurring and the appearance of needle like unwanted phases. Figure (b) shows increasing methanol concentration leaves minimal jarosite formation instead predominately amorphous iron oxy-hydroxy sulphates any remaining jarosite formation is severely mottled. Mottling occurs as a result of the extremely low pH levels present. 90% MeOH concentration levels regardless of temperature fail to produce any Fe oxyhydroxy jarosites instead what appears to be Mikasaite - crystalline iron sulphate - $\text{Fe}_2(\text{SO}_4)_3$.

from jarosite formation. Jarosite precipitation is a hydrolysis reaction, as the $[\text{Fe}(\text{H}_2\text{O})_5(\text{SO}_4)]^+$ is reacted with an appropriate A-site so more H^+ ions are released. The other precursor which is prevalent, $[\text{Fe}(\text{H}_2\text{O})_5(\text{OH})]^{2+}$, leads to the formation of amorphous iron oxy-hydroxy phases through the bridging hydroxyl groups and this will favour a higher pH. How does the addition of MeOH push the reaction towards amorphous phases considering the low pH values?

Upon releasing the pressure of a Pyrex pressure tube with a high concentration of MeOH, amongst all temperature ranges, bubbling occurs and a sweet pungent gas is evolved. Though it is difficult to ascertain the product, it is believed to be methyl methanoate simply detecting it by smell and a reasonable product considering the reactants involved. The production of methyl methanoate is an industrial process from the dehydrogenation of MeOH using high temperatures and specialist copper catalysts.



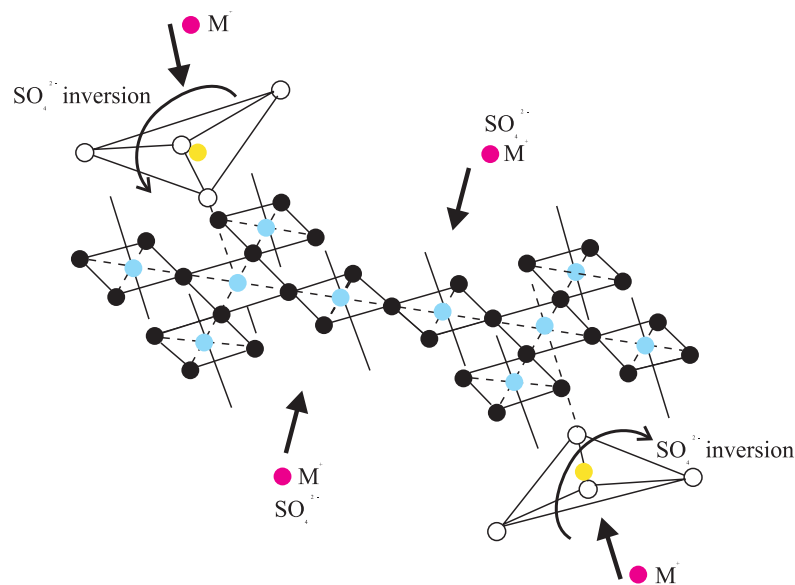
To rationalize this with jarosite precipitation, one has to appreciate that the formation of jarosite is a forced hydrolysis reaction [21,45,46]. Forced hydrolysis in the case of jarosite formation is using large concentrations of $\text{Fe}_2(\text{SO}_4)_3$ and forced hydrolysis further increased under hydrothermal conditions. Forced hydrolysis prevents extensive polymerization of the Fe^{3+} centres, which are bridged by OH^- or H_2O units separating out the Fe^{3+} units. Under low pH and forced hydrolysis conditions, the Fe^{3+} complex centres are more stable and can polymerize together to form tighter Fe^{3+} centres capped by SO_4^{2-} and bridged OH^- ions [40,48]. This is achieved by the stability of the $[\text{FeSO}_4]^+$ complex in low pH solutions [40]. The introduction typically of a monovalent cation (K^+ , Na^+ , Ag^+ or NH_4^+) will hasten the formation of tight Fe^{3+} centres [40,47,48], by preventing extensive polymerizing at higher pH levels of Fe^{3+} centres with hydroxo-bridges [47] to form various amorphous Fe-oxy-hydroxy sulphates or Fe-oxy-hydroxides. Figure 4.6 shows how upon the addition of SO_4^{2-} and a monovalent cation reduces the progressive polymerisation and instead produces a jarosite precursor as shown in Figure 4.6(a), before precipitation of jarosite proper (Figure 4.6(b)). During the formation of

jarosite it can be seen that the Fe-OH network becomes buckled with the OH⁻ residing slightly above and below the plane made up of the Fe³⁺ ions. This buckling is caused by the sulphate groups which are above and below the plane of Fe³⁺ ions binding to the Fe centres. This slight distortion of Fe-octahedral coordination is paramount to the magnetic properties of jarosites and thus it is very important to know how the chemistry affects the jarosite crystal structure which is discussed in detail in

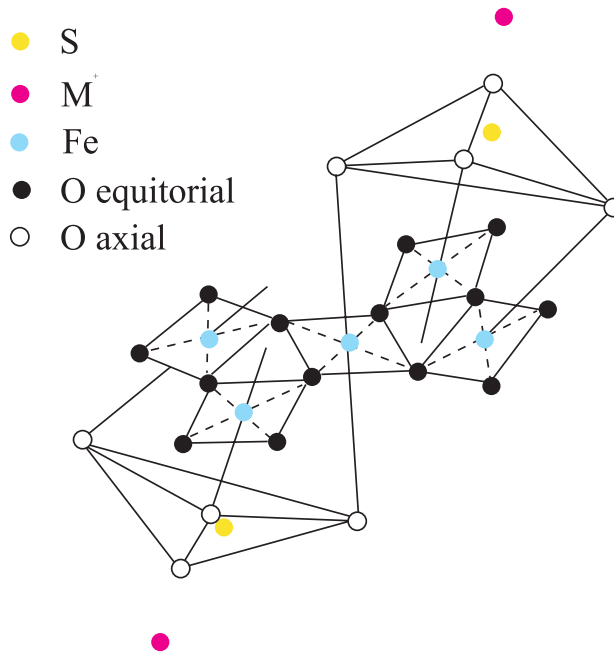
The high methanol concentration reactions highlight the stability of the [FeSO₄]⁺ complex with the possible evidence such that it can initiate other reactions such as methanol dehydrogenation. The positive Fe centre allows the oxygen from the methanol and possible dissolved oxygen to bind to the surface and initiate partial or full oxidation of methanol. Thus, either formaldehyde is released or continued methanol oxidation will result in esterification with the remaining methanol enabled by high quantities of SO₄²⁻ ions acting as a catalyst. The reason for the then lack of jarosite precipitation (Figure 4.5(c)) or the occurrence of unwanted amorphous phases (Figures 4.3(e) 4.3(f) 4.4(d)) is because there lacks the ability to solvate the H₃O⁺ ion. High concentrations of MeOH and little H₂O will fail to stabilise any resultant hydronium ion formed in the extremely low pH ranges of these reaction. The lack H₃O⁺ ion solvation will reduce the ability to form a monovalent cation which will then precipitate jarosite. If MeOH concentrations are to 90% MeOH and only 10% H₂O the only product left is a small yield of crystalline Fe₂(SO₄)₃ - Mikasaite, evidenced under SEM resembling artex in Figure 4.5(d)

Oxidative formation mechanism

Further evidence of a different reaction pathway was the appearance of a white solid appearing on the Fe surface hydrothermal oxidative synthesis. The white product could clearly be seen enveloped by jarosite precipitate that had collected at the at the bottom of the Pyrex tube. The visual evidence, shown in Figure 4.7, suggested that the white solid was an intermediate involved prior to the jarosite formation and after in the oxidation of the Fe wire.



(a) Jarosite precursor



(b) Jarosite precipitation

Figure 4.6: Figure (a) shows the jarosite precursor and the beginning of jarosite formation with the rotation of the SO_4^{2-} unit and the addition of further SO_4^{2-} units and a monovalent cation to ensure jarosite as the product, which results in Figure (b). The plane of the Fe-OH units becomes buckled upon jarosite formation because of the introduction of more sulphate units, octahedrally coordinating with the central Fe^{3+} ion. This distortion of bond angles will change the exchange pathway between the Fe^{3+} centres, in turn will affect the resultant magnetic behaviour.



Figure 4.7: Potassium jarosite (orange) and Szomolnokite (discovered as a white intermediate phase), covering the Fe wire and dispersed among the jarosite precipitate. Use of Pyrex tubes not only allows better temperature gradients, but allows visual inspection. The divisions on the ruler define millimeters

Identification of meta-stable intermediate in the oxidative synthesis

The white solid (Figure 4.7) disappeared upon cooling the sample and suggested that it was meta-stable. The white solid was successfully retrieved by quenching the reaction from 170°C to room temperature by placing the Pyrex tube directly into cold water. The white solid was scraped from the surface of the Fe wire, dried and placed on to a low silica background plate for powder diffraction using an acetone slurry. X-ray powder diffraction data was taken using a Bruker D8 diffractometer in Bragg-Bretano geometry using $\text{CuK}\alpha_1$ radiation, data collected using a PSD detector. The step size was $\Delta(2\theta) = 0.073^\circ$ with a counting time of 0.6s per $\Delta(2\theta)$ and the plate was spun at 15rpm. The data was only good enough for pattern matching due to the high Fe content giving rise to a raised background because of fluorescence from the Fe. Using the Bruker's own pattern matching software Eva a match was found to be Szomolnokite – $\text{Fe}^{2+}\text{SO}_4\cdot\text{H}_2\text{O}$. Figure 4.8 shows how the powder diffraction taken from meta-stable white residue from the oxidative reaction and a powder diffraction pattern for Szomolnokite [2] matches and confirming that Szomolnokite is an intermediate in the formation of jarosite

for this reaction.

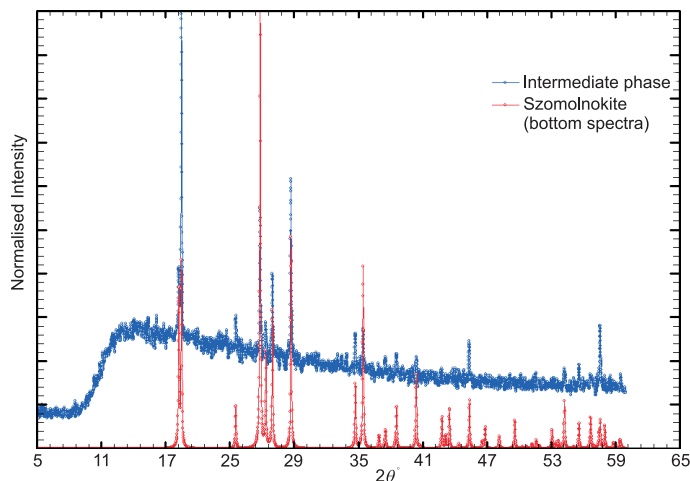
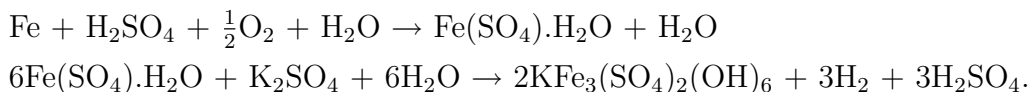


Figure 4.8: The powder data from the white intermediate (blue pattern) matches the powder taken by Wildner and Giester [2] of Szomolnokite (red pattern) – $\text{Fe}^{2+}\text{SO}_4\cdot\text{H}_2\text{O}$. Both powder diffraction data sets were imported into Fullprof [3] and plotted using WinPLOTR [4].

4.1.5 Analysis of the two Methods and Comparison with Natural Samples

Forced Hydrolysis versus Oxidative

The difference between the two methods, besides the obvious starting oxidation state of the Fe, is the mechanism of formation. Having detected the presence of Szomolnokite ($\text{Fe}(\text{SO}_4)\cdot\text{H}_2\text{O}$) as an intermediate, one can piece together the reaction mechanism for the oxidative method and compare this with jarosite formation under forced hydrolysis conditions. Another key component to the oxidative reaction is that jarosite does not precipitate from Szomolnokite without the presence of a non-hydronium A-site cation. During the reaction, hydrogen gas was liberated and detected by the accidental ignition of the gas produced. Using this information the mechanism for jarosite precipitation of the oxidative method is as follows,



Thus it appears there is a completely different reaction mechanism, one that does not allow for the formation of hydronium jarosite. This is primarily due to the absence of the $[\text{FeSO}_4]^+$ complex which, as it is solvated, [40] allows for H_3O^+ incorporation. Instead the jarosite formation from the intermediate can be evidenced from the similarity in crystal structures of the two iron sulphates derivatives. Structurally, jarosite shares many features, and in this case its origins, with Szomolnokite. The resemblance can be seen in the Fe coordination shown in Figure 4.9. The Fe-O(S) distance within potassium jarosite is 2.076 Å, slightly longer than in Szomolnokite, at 2.053 Å. The Fe-O(H) distance, bridging the Fe centres in jarosite, is about 1.9806 Å, in Szomolnokite the Fe-O(H₂) distance is much longer at 2.228 Å. Oxidation of the Fe^{2+} to Fe^{3+} in Szomolnokite hydrolyses the H₂O molecules and draws the OH units closer to the Fe^{3+} centres to allow bridging and subsequent formation of the Fe^{3+} octahedrons that make up the *kagomé* plane.

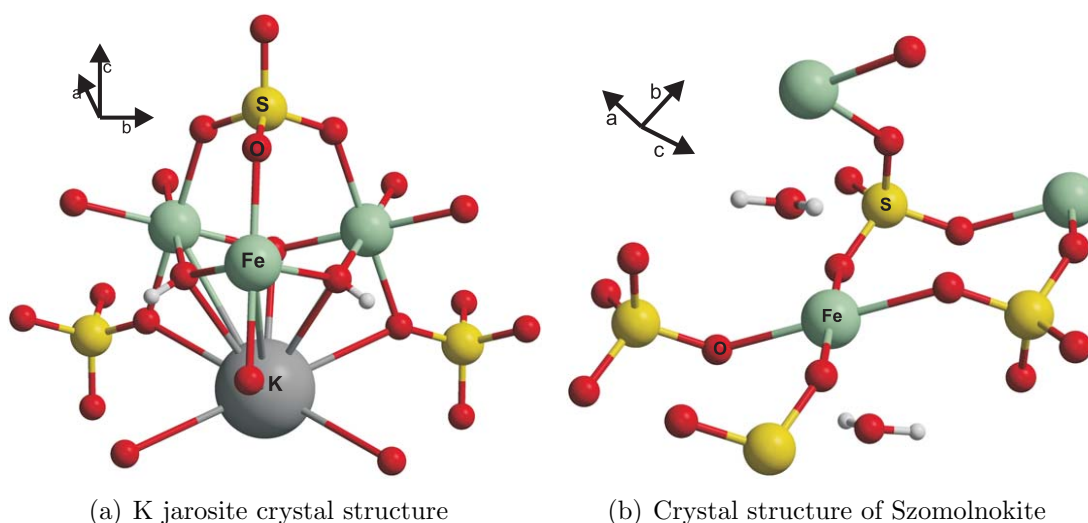


Figure 4.9: Structural representation of the jarosite structure. The sulphate groups cap above and below the Fe octahedra sitting along the 3-fold axis. Each of these subunits is separated by the A-site, K^+ in the diagram. (b) Szomolnokite has a more open structure; the distortion from rhombohedral is only slight: $\beta \sim 120^\circ$ and the a and b lattice parameters are similar to the a parameter in jarosite.

Minimal Fe vacancies are expected from the oxidative synthesis method because the charge neutrality of the Szomolnokite intermediate will reduce the need for

charge compensation and any associated Fe vacancies or H₂O inclusion. Formation of the jarosite can only be completed when the appropriate A-site sulphate reacts. It is therefore the high Fe occupation of Szomolnokite that keeps to a minimum the unstoichiometry of the resultant phase. Oxidation from Fe²⁺ to Fe³⁺ is very rapid and the associated incorporation of the A-site cation will almost be simultaneous still ensuring a almost ideal stoichiometry.

Likewise for hydronium jarosite, considering the extreme forced hydrolysis conditions one would expect a high Fe occupation with minimal deviation from the ideal stoichiometric formula, unlike for natural jarosite formation in weathering or as a result of Acid Mine Drainage. The greater stability of the [FeSO₄]⁺ complex under forced hydrolysis conditions ensures jarosite precipitation will eventually be the dominant phase - through the process of Ostwald ripening [55] - and will be almost true to the stoichiometric value.

The addition of MeOH as a solvent highlighted many factors underlying forced hydrolysis conditions. The addition speeded up the rate of formation of jarosite and increased yields beyond that obtainable for any reaction using 100% H₂O as the solvent. The explanation for lower yields for hydronium jarosite compared to other A-site ions is related to the hydration number for A-site cations and that MeOH helps lower the hydration number. The hydration number, h , for K⁺, Na⁺, Rb⁺ and NH₄⁺ in solution, $h=1.8\pm0.5$, 3.9 ± 0.5 , 1.8 ± 0.3 and 1.8 ± 0.5 respectively [56], is significantly lower than H₃O⁺, $h=6.7\pm0.7$ (H⁺) [56]. MeOH for comparison is $h=1\pm0.3$ [56].

This leads to a possible slightly different mechanism of formation for hydronium jarosite in comparison to the forced hydrolysis conditions mentioned previously based upon Mikasaite 4.5(d) which in essence is similar to the [FeSO₄]⁺ complex as discussed above.



The solvated hydronium ion occurs as the solvated complex [H₂O(H₂O₆)⁺ [56]

The premise to synthesis jarosite samples was the believe that better quality jarosites could be produced in the laboratory rather than found in nature [6, 8, 20] and to understand the formation process so that it can be improved upon [41]. The

problems of natural jarosite are the inclusion of other minerals, producing many similar minerals (beaverite and dorallcharite) based upon the jarosite structure but containing mixed valence metal ions (Cu^{2+} , Pb^{2+} , Al^{3+} or Tl^{2+}) and substitution of the sulphate group for arsenate or chromate groups. Hydronium jarosite is very rare to find naturally occurring and can be explained by the need for forced hydrolysis conditions because of the high solvation number, h .

Naturally found pure A-site jarosites for instance, K^+ , Na^+ or Ag^+ , have a high Fe content almost or 100% Fe iron coverage, for further details refer to PhD thesis by Smith A.M.L. [26]. Energetic computational studies have shown that the energy for an associated Fe defect is high and that it is unlikely that the structure can sustain many Fe defects and therefore Fe coverage is correspondingly high [57].

4.2 Results of Hydronium Jarosite Synthesis and Physical Characterisation

Most of the hydronium jarosites that were synthesised in Pyrex tubes were used to produce the following data and information to be shown in the proceeding section. Samples which were not used either produced unwanted Fe hydroxy sulphates as is the case for the high MeOH concentrations preparations at 150°C or in the rare occasion (sample S23.b) where the first preparation lead to a value for T_g widely different from what was expected from a series of preparations. Samples denoted with S are for MeOH mix preparations and each MeOH series is designated by the temperature of synthesis.

4.2.1 Elemental Analysis Results

There were several methods used to determine elemental composition.

Sample purity was confirmed using both X-ray powder diffraction and SEM (refer to Figures 4.1, 4.2, 4.3, 4.4, 4.5).

Tables 4.5 and 4.7 show the synthesis conditions, lattice parameters and basic magnetic characterisation, including the spin glass freezing temperature, T_g , for hydronium jarosites.

Sample	Synthesis		Lattice parameters (Å)			Magnetic characterisation (K)		
	Temp. (°C)	%H ₂ O	yield (g)	<i>a</i>	<i>c</i>	S.C.	T_g	$\theta_w(\pm 100)$
31	120	100	0.081	77.36537(28)	17.0571(8)	N/A	19.7	-1485
33	125	100	0.101	7.36820(30)	17.0618(8)	N/A	18.70	-1330
44	127	100	0.312	7.3658(4)	17.0616(10)	N/A	17.83	-1465
29	130	100	0.186	7.36940(34)	17.0548(12)	NCS	17.74	-1420
42	135	100	0.371	7.3673(4)	17.0541(11)	SRS	16.90	-1410
48	138	100	0.289	7.36992(25)	17.0546(6)	N/A	16.64	-U/A
30	140	100	0.340	7.37026(28)	17.0510(7)	N/A	16.32	-1475
47	142	100	0.361	7.36796(23)	17.0460(6)	N/A	16.8	-U/A
49	145	100	0.353	7.36944(28)	17.0453(6)	NCS	15.8	-U/A
24	150	100	0.498	7.3698(4)	17.0403(9)	NCS	15.69	-1400
16	150	100	0.458	7.3705(6)	17.0391(18)	NCS	15.78	-1580
27	150	100	0.530	7.3688(4)	17.0389(15)	NCS	15.71	-1530

Table 4.5: Table showing the synthesis conditions, lattice parameters and magnetic characterisation for hydronium jarosite samples prepared using 100% H₂O as the solvent. S.C. stands for single crystal and shows where the data was taken from - NCS (Southampton) or SRS (Daresbury station 9.8)

Sample	Synthesis			Lattice parameters (Å)			Magnetic characterisation (K)		
	Temp. (°C)	%H ₂ O	yield (g)	a	c	S.C.	T _g	$\theta_W(\pm 100)$	
S9	120	90	0.134	7.3668(4)	17.0613(9)	N/A	18.8	-1565	
S10	120	80	0.237	7.3650(4)	17.0547(12)	NCS	18.38	-1530	
S11	120	70	0.341	7.3670(5)	17.0513(14)	NCS	17.28	-1360	
S12	120	60	0.479	7.36833(33)	17.0488(9)	SRS	15.77	-1420	
S13	120	50	0.581	7.3699(4)	17.0421(10)	N/A	14.84	-1580	
S14	120	40	0.687	7.3706(9)	17.0211(29)	N/A	12.73	-1315	
S15	120	30	0.643	7.37523(32)	17.0125(7)	NCS	11.84	-1310	
S16	120	20	0.425	7.3738(8)	16.9960(29)	N/A	11.26	-1195	
S21	130	90	0.363	7.36734(26)	17.0540(6)	N/A	17.36	-1490	
S22	130	80	0.379	7.3694(4)	17.0520(10)	NCS	16.52	-1595	
S23_b	130	70	0.447	7.36981(34)	17.0515(8)	SRS	16.19	-U/A	
S24	130	60	0.666	7.3701(5)	17.0412(15)	NCS	13.65	-1480	
S25	130	50	0.559	7.37265(32)	17.0345(8)	SRS	13.10	-1520	
S26	130	40	0.745	7.3726(5)	17.0144(13)	SRS	12.00	-1355	
S27	130	30	0.903	7.37262(29)	16.9936(6)	NCS	11.57	-1285	
S28	130	20	0.765	7.37631(29)	16.9846(6)	N/A	10.92	-1305	
S30	140	90	0.573	7.37231(24)	17.0378(7)	SRS	14.17	-1670	
S31	140	80	0.415	7.37206(29)	17.0491(9)	N/A	15.1	-U/A	
S32	140	70	0.543	7.3698(4)	17.0360(11)	N/A	14.38	-U/A	
S33	140	60	0.613	7.37401(29)	17.0365(9)	NCS	13.7	-U/A	
S34	140	50	0.747	7.37193(23)	17.0289(7)	N/A	13.85	-1440	
S35	140	40	0.852	7.37506(25)	17.0203(8)	N/A	12.34	-U/A	
S1	150	90	0.514	7.3746(4)	17.0554(14)	N/A	15.71	-1490	
S2	150	80	0.571	7.3726(4)	17.0426(12)	N/A	15.36	-1505	
S17	150	75	0.584	7.3686(5)	17.0327(14)	N/A	14.63	-1415	
S3	150	70	0.655	7.37246(26)	17.0393(9)	N/A	14.76	-1415	
S18	150	65	0.638	7.3712(4)	17.0316(12)	N/A	14.5	-1450	
S4	150	60	0.711	7.37436(27)	17.0308(10)	N/A	13.87	-1400	

Table 4.7: Table showing the synthesis conditions, lattice parameters and magnetic characterisation for hydronium jarosite samples prepared using a mix of H₂O and MeOH as the solvent. S.C. stands for single crystal and shows where the data was taken from - NCS (Southampton) or SRS (Daresbury station 9.8)

4.3 Powder Diffraction Results and Analysis of Iron Jarosites

4.3.1 Phase identification

The pattern matching software EVA confirmed the presence of hydronium jarosite with its own database. Further confirmation that jarosite was the only product was by looking at two distinct peaks which appear with the following approximate d-spacings ~ 3.08 and 3.13\AA for hydronium jarosite whereas for unwanted iron oxyhydroxy sulphates these peaks are shifted to slightly larger d-spacings ~ 3.12 and 3.25\AA . EVA was also used to match for all other jarosites where its database contained many more diffraction patterns for non-hydronium jarosites to be confident the samples were phase pure.

4.3.2 Comparison of Lattice Parameters with Spin Glass Transition Temperature for the Hydronium Jarosites using Rietveld Refinement

All the crystal structural data for the preceding section relies on the Rietveld model described in the experimental methods: the atomic positions are taken from the data by the refinements by Andrew Wills on hydronium jarosite [28]. The data unfortunately is tainted by high background because of the fluorescence (Figure 4.10) and only lattice parameters could be investigated. The error bars expressed in the following subsection are the e.s.ds generated by GSAS for the lattice parameters and the error in T_g (K) is a judgment by determining the transition temperature by eye from the susceptibility data.

Diffraction patterns taken from all of the hydronium jarosites listed in Tables 4.5 and 4.7 show strong correlations amongst lattice parameters and synthesis conditions with the spin glass transition, T_g . Initially looking at the hydronium samples synthesised in 100% H_2O solvent there is a remarkable correlation between synthesis temperature and the spin glass freezing temperature as shown in Figure 4.11.

All the samples in Figure 4.11 were synthesised for a duration of 21 hours and it clearly shows the effect of temperature has upon the magnetic transition:

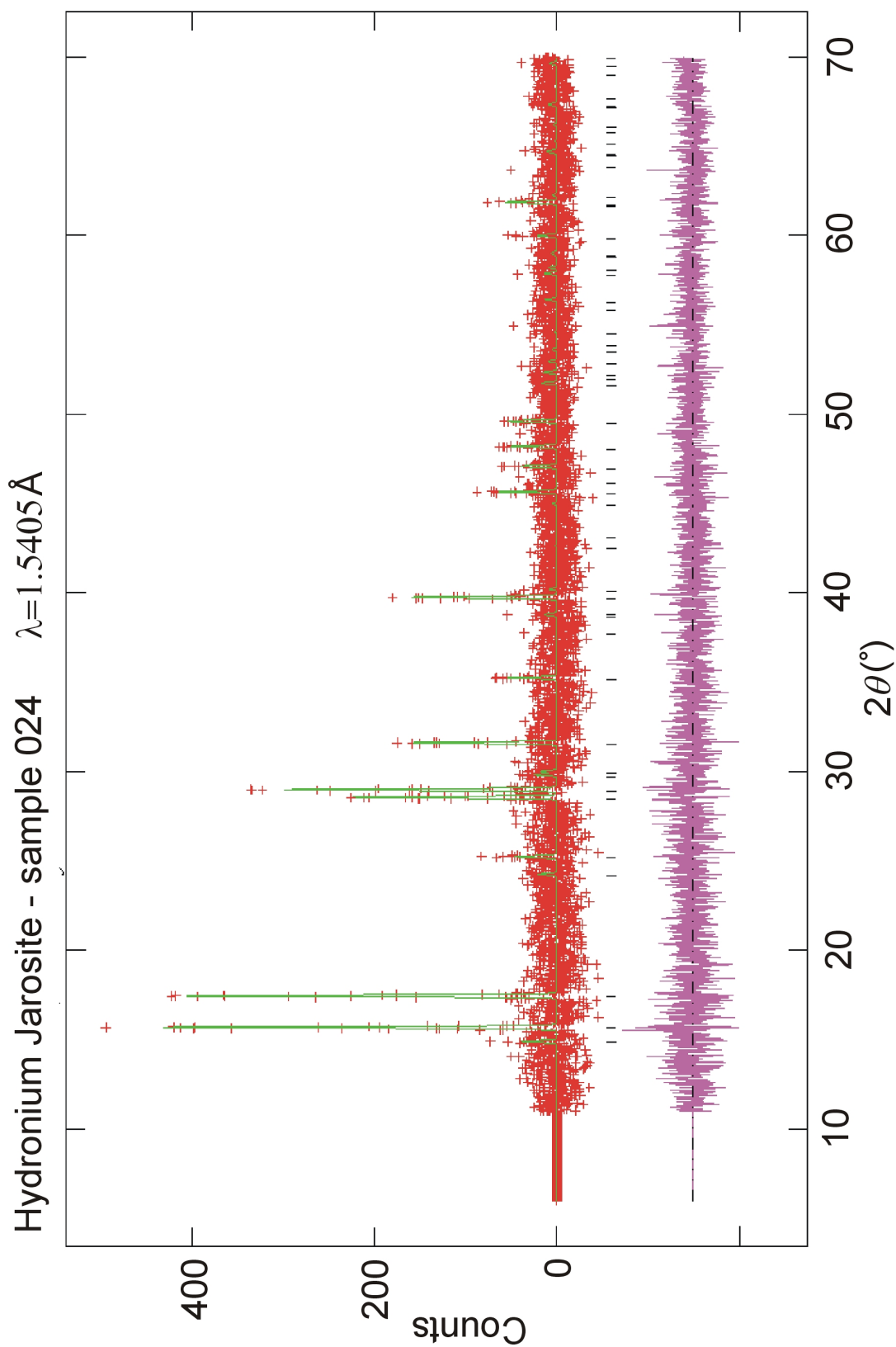


Figure 4.10: Rietveld refinement plot for hydronium jarosite sample 024 taken from the Bruker D8 diffractometer at room temperature. There is a raised background due to the Cu radiation causing the Fe to fluoresce, leaving the data sufficient only to obtain lattice parameters. The purple plot is the difference between the observed data (red) and the model (green). The same setup (refer to subsection 3.8.1) was used for all the other jarosites listed in Tables 4.5 and 4.7.

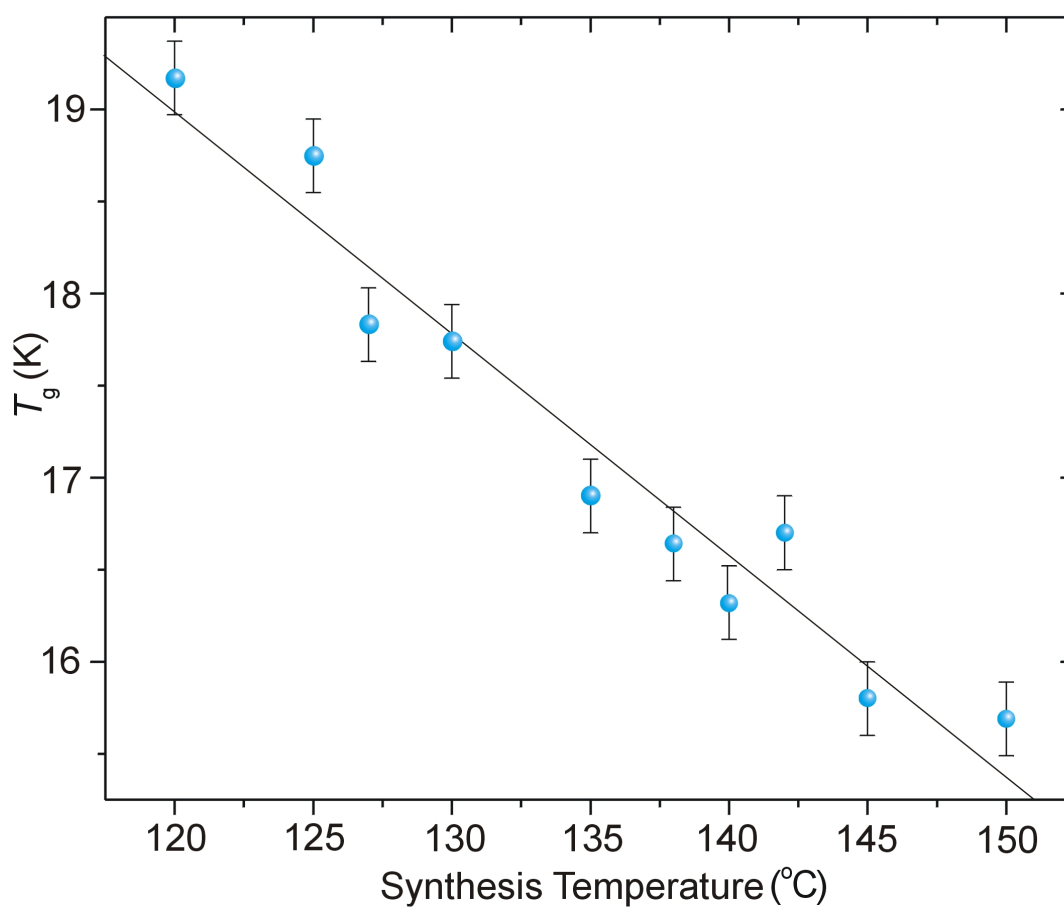


Figure 4.11: Spin glass freezing temperature plotted against the synthesis temperature of hydronium jarosites using 100% H_2O as solvent. It shows that synthesis conditions can influence the spin glass transition temperature and how there is a strong correlation between synthesis temperature and T_g .

increasing synthesis temperature lowers T_g . This would suggest, as summarized earlier - better jarosite formation with increasing temperature, that the consequence of “better” formed jarosites lowers T_g . Whether this is a consequence of improved Fe stoichiometry or a different structural confirmation can not be gathered at this stage as ICP-AES elemental analysis is inconclusive.

Comparison of the c Lattice Parameter with T_g .

This was then extended to try and find a physical consequence of increasing synthesis temperature with decreasing T_g . It was found there is a contraction along the c lattice parameter that correlates strongly with decreasing T_g as shown in Figure 4.12. The contraction arises primarily across the T-A-T sheeting which was revealed through X-ray single crystal diffraction experiments.

It turns out for each temperature series of preparation of hydronium jarosite using MeOH/H₂O mixes as a solvent produces similar correlations between the c axis and T_g : contraction along the c axis with decreasing T_g . These correlations are shown in Figures 4.13, 4.14, 4.15 and 4.16.

As can be seen for individual series of preparations correlations with decreasing values of T_g and decreasing length in the c parameter. The data is limited in quantitative quality because of the high amount of fluorescence, short scan lengths and the data was collected at room temperature, but qualitatively is very good, especially when all the data points are shown together on one graph. Figure 4.17 clearly shows that decreasing values of T_g are obtained by using a combination of high synthesis temperatures and high MeOH concentrations, this in turn relates to a structural change which causes a contraction in the c parameter correlating with values for T_g .

Changes in synthesis conditions clearly influences the crystal structure, albeit slight 0.08 Å, and these crystallographic changes affect the temperature for the spin glass transition. Which crystallographic changes are occurring are unknown from this powder data, but looking at the changes in the a parameter, though the correlation is not as strong, show it to be more than a simple overall contraction.

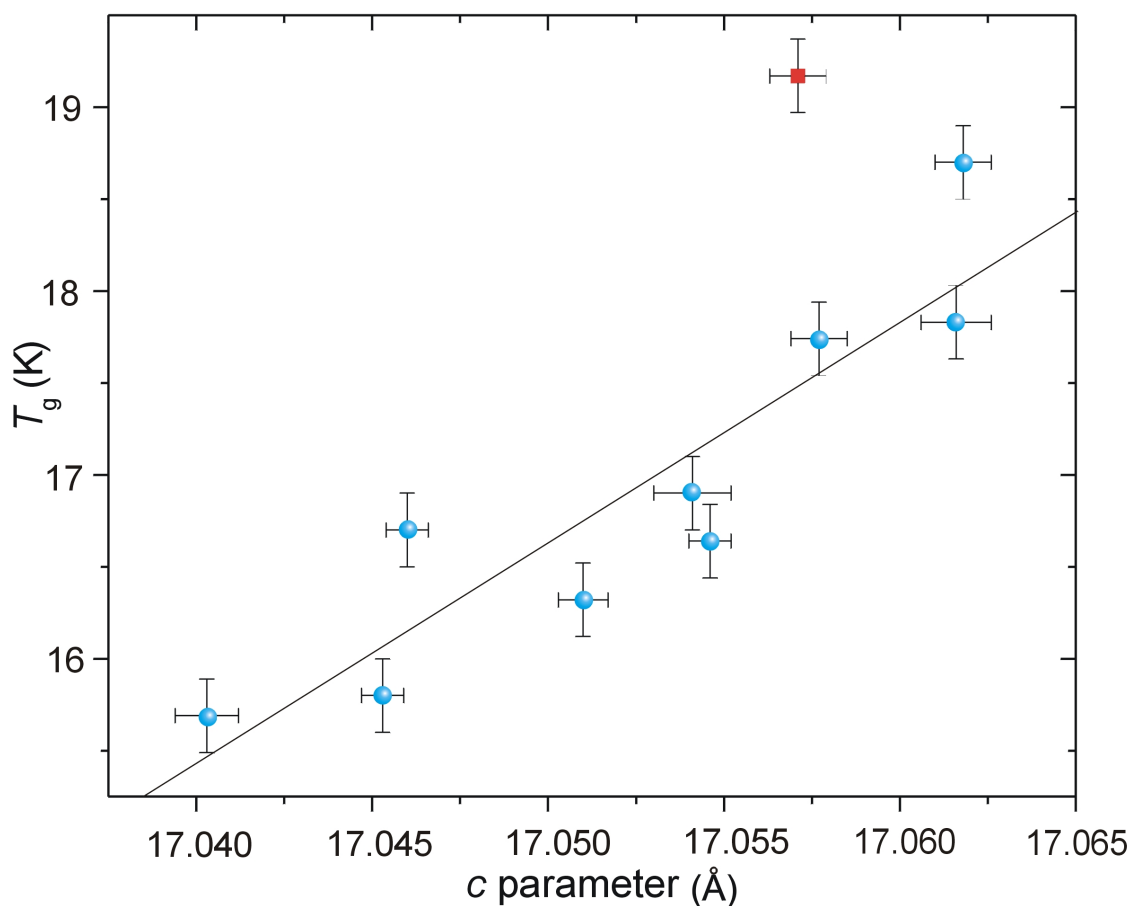


Figure 4.12: T_g plotted against the c parameter of the crystal structure for hydronium jarosites synthesised in 100% H_2O solvent; the samples included are listed in Table 4.5. The graph shows how this change in T_g correlates to a structural change in the c parameter of the unit cell: decreasing T_g corresponds to a more 3D structure as the jarosite structure contracts along the c axis. The red point represents the lowest temperature synthesis of hydronium jarosite (120°C) and results in poorly formed jarosite and this point is excluded in the data fit. The change along c occurs primarily in a contraction in the T-A-T sheeting across the 12 coordinate site, where the H_3O^+ unit resides in the A-site position.

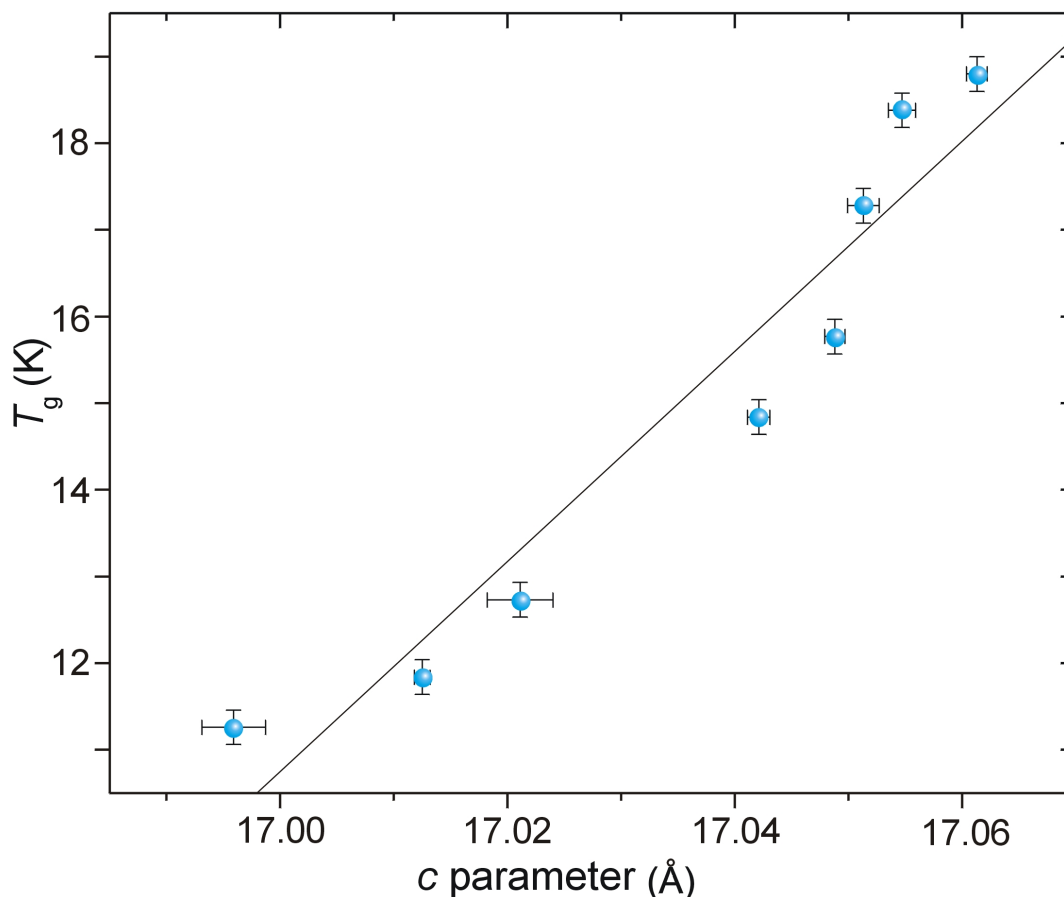


Figure 4.13: T_g plotted against the c parameter of the crystal structure for hydronium jarosites synthesised in various concentrations of MeOH/H₂O solvent at 120°C. The samples are S9-S16, increasing in MeOH concentration from S9-S16, refer to Table 4.7 for further information. The graph shows that values of T_g correlate to a structural change in the c parameter of the unit cell: decreasing T_g corresponds to a more 3D structure as the jarosite structure contracts along the c axis. The correlation between decreasing values of T_g and the contraction along the c axis also corresponds to an increasing MeOH concentration. The data points shown are sequential in MeOH concentration. The change along c occurs primarily in a contraction in the T-A-T sheeting across the 12 coordinate site, where the H₃O⁺ unit resides in the A-site position.

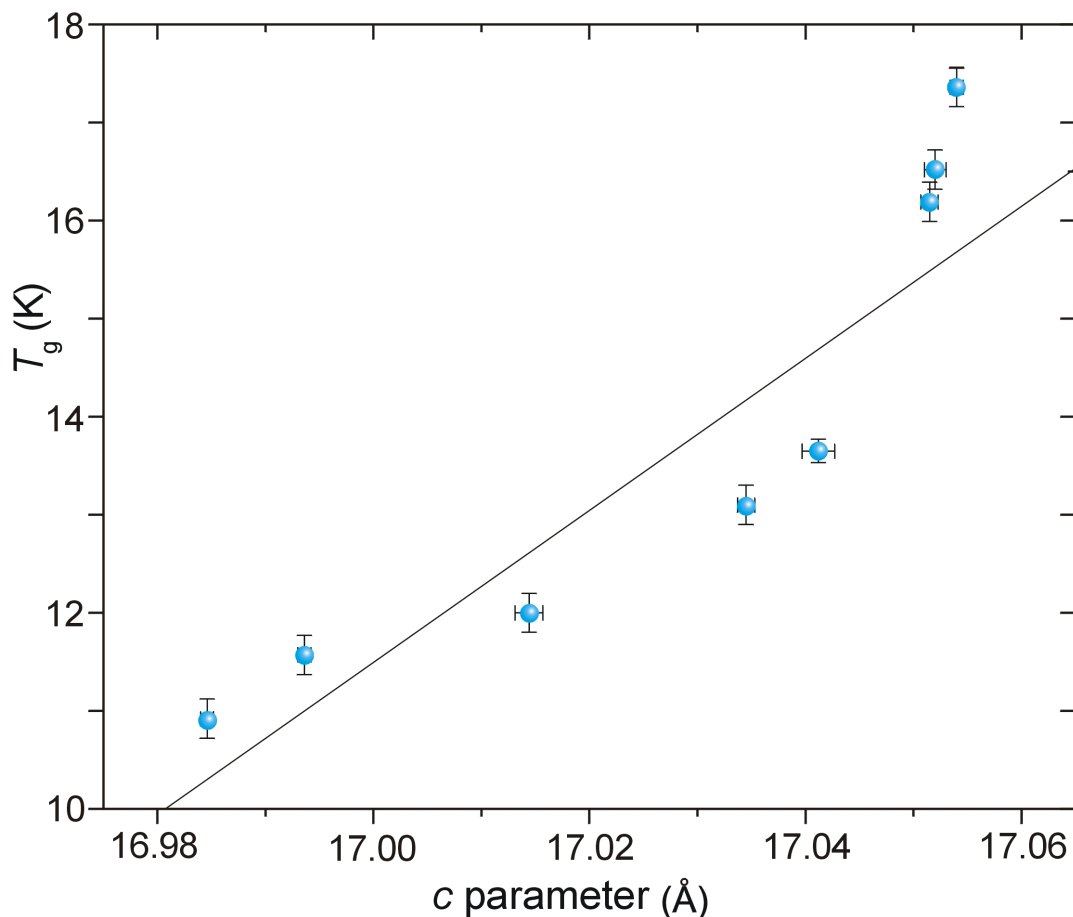


Figure 4.14: T_g plotted against the c parameter of the crystal structure for hydronium jarosites synthesised in various concentrations of MeOH/H₂O solvent at 130°C. The samples are S21-S28, increasing in MeOH concentration from S21-S28, refer to Table 4.7 for further information. The graph shows that values of T_g correlate to a structural change in the c parameter of the unit cell: decreasing T_g corresponds to a more 3D structure as the jarosite structure contracts along the c axis. The correlation between decreasing values of T_g and the contraction along the c axis also corresponds to an increasing MeOH concentration. The data points shown are sequential in MeOH concentration. The change along c occurs primarily in a contraction in the T-A-T sheeting across the 12 coordinate site, where the H₃O⁺ unit resides in the A-site position.

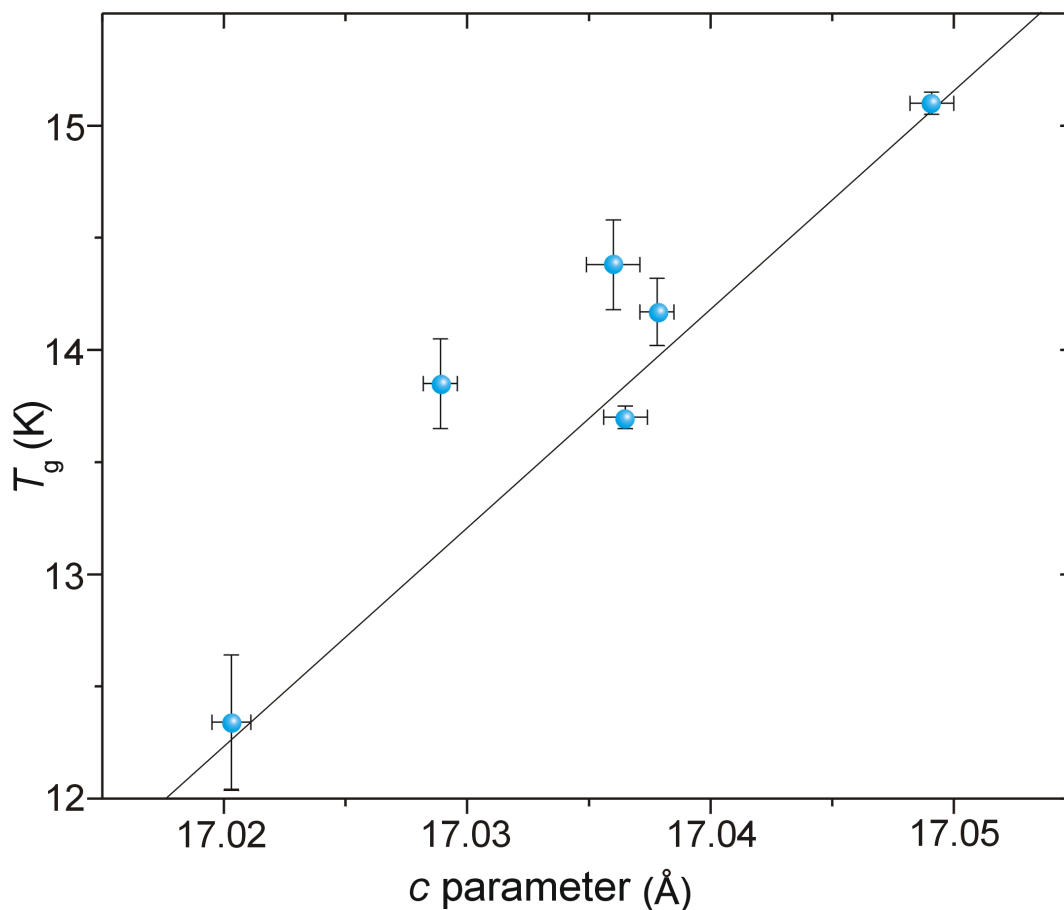


Figure 4.15: T_g plotted against the c parameter of the crystal structure for hydronium jarosites synthesised in various concentrations of MeOH/H₂O solvent at 140°C. The samples are S30-S35, increasing in MeOH concentration from S30-S35, refer to Table 4.7 for further information. The graph shows that values of T_g correlate to a structural change in the c parameter of the unit cell: decreasing T_g corresponds to a more 3D structure as the jarosite structure contracts along the c axis. The correlation between decreasing values of T_g and the contraction along the c axis also corresponds to an increasing MeOH concentration. The data points shown are sequential in MeOH concentration. The change along c occurs primarily in a contraction in the T-A-T sheeting across the 12 coordinate site, where the H₃O⁺ unit resides in the A-site position. The data set is not as extensive because increasing MeOH concentration coupled with increasing temperature result in the occurrence of unwanted Fe oxy-hydroxy sulphates.

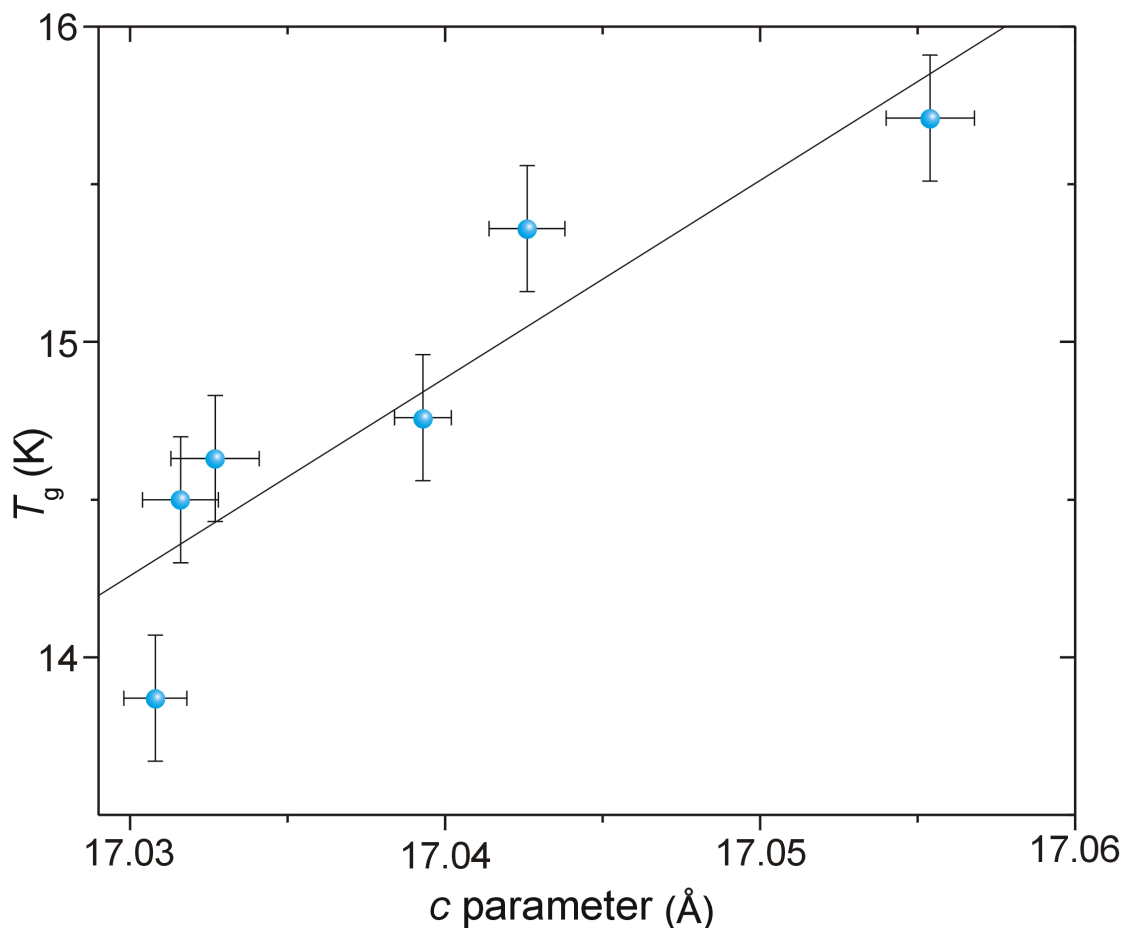


Figure 4.16: T_g plotted against the c parameter of the crystal structure for hydronium jarosites synthesised in various concentrations of MeOH/H₂O solvent at 140°C. The samples are S1-S4, increasing in MeOH concentration from S1-S4, refer to Table 4.7 for further information. The graph shows that values of T_g correlate to a structural change in the c parameter of the unit cell: decreasing T_g corresponds to a more 3D structure as the jarosite structure contracts along the c axis. The correlation between decreasing values of T_g and the contraction along the c axis also corresponds to an increasing MeOH concentration. The data points shown are sequential in MeOH concentration. The change along c occurs primarily in a contraction in the T-A-T sheeting across the 12 coordinate site, where the H₃O⁺ unit resides in the A-site position. The data set is not as extensive because increasing MeOH concentration coupled with increasing temperature result in the occurrence of unwanted Fe oxy-hydroxy sulphates.

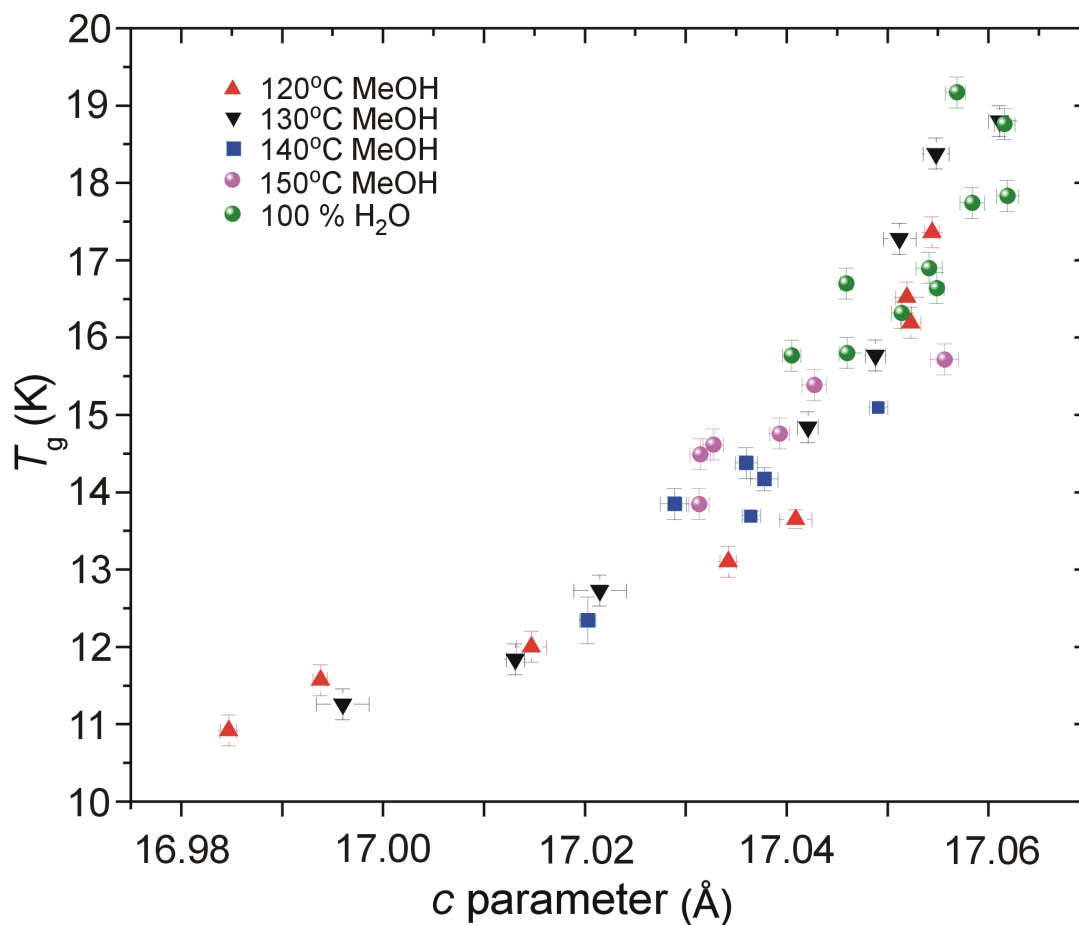


Figure 4.17: T_g plotted against the c parameter of the crystal structure for all hydronium jarosites shown in Tables 4.5 and 4.7. It clearly shows a structural change is occurring which causes an overall contraction along c that gives rise to a corresponding decrease in T_g .

Comparison of the a Lattice Parameter with T_g .

Looking at change within the a lattice parameter we see that a similar change happens, but an expansion across the a axis correlates with a decrease in T_g . Some of the data sets for the individual synthesis series do show a satisfactory correlation and where not, no line of best fit is provided. Figures 4.19 and 4.20 do show a correlation between the a lattice parameter and T_g , whereas for Figures 4.18, 4.21 and 4.22 no discernible trend appears. Though a combination of all the data points suggests a trend between expansion in the a axis and T_g as shown in Figure 4.23.

Overall, there appears to be another relationship between lattice parameters and the eventual magnetic transition temperature, shown in Figure 4.23. There is a trend shown by an expansion along the a axis corresponding to a decrease in T_g .

Summary of Lattice Parameters Investigations

The clearest change can be seen along the c axis, the changes in length are greater (0.08 Å) and the correlations are stronger between decreasing T_g and decreasing c . Whereas changes in the a parameter are slighter (0.012 Å) and the observed relationship between the a axis and T_g is more of a trend - exemplified by the distribution in a widening with decreasing T_g . The benefit of the comparing the two lattice parameters shows that as one parameter contracts the other appears to expand slightly, thus the changes are not a simple overall contraction in the crystal structure. Instead there must be a more profound structural change influencing the magnetic transition.

4.3.3 The Non-Hydronium Jarosites

4.4 Single Crystal Results and Analysis of Iron Jarosite

Table 4.8 shows data for hydronium jarosite sample No. 24 (100% H₂O solvent, 150°C) collected at Southampton University at 85(2)K.

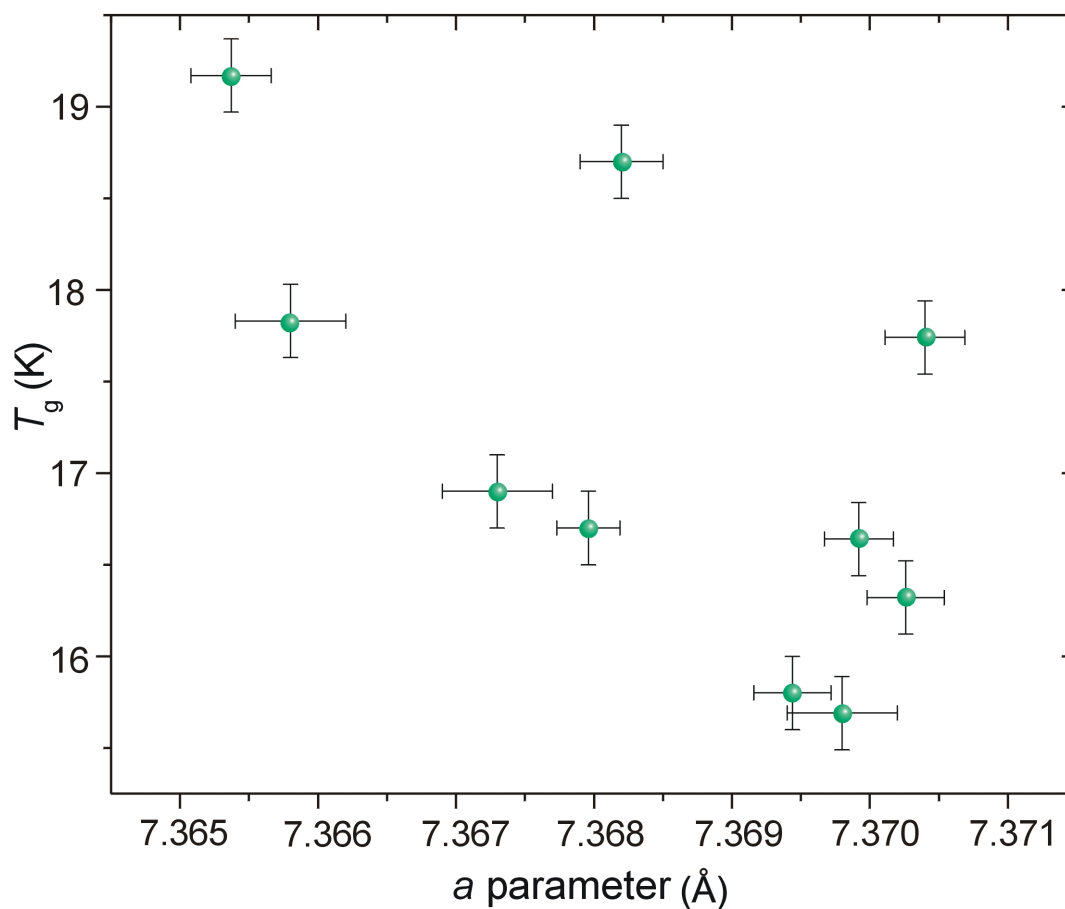


Figure 4.18: T_g plotted against the a parameter of the crystal structure for hydronium jarosites synthesised at various temperatures using 100% H_2O as the solvent; the samples included are listed in Table 4.5. The graph, unlike for other synthesis series, does not show any correlation between values of T_g and to a structural change in the a parameter of the unit cell.

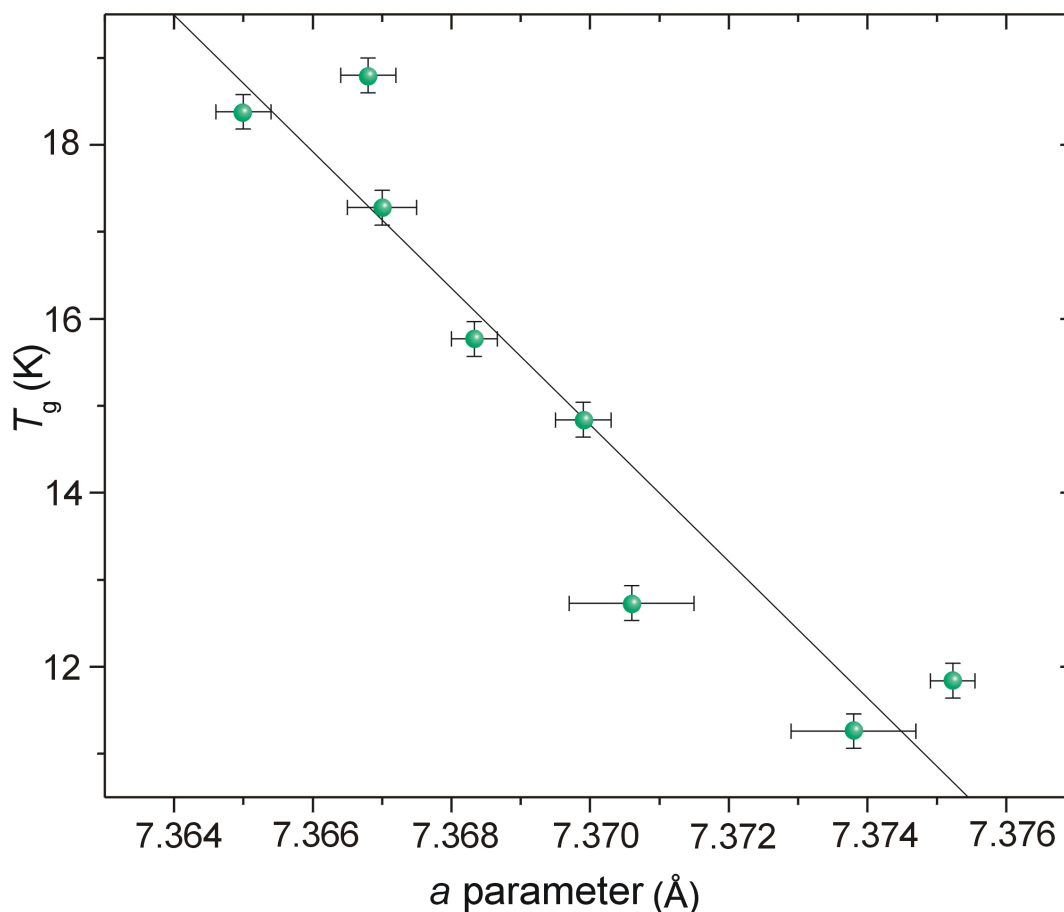


Figure 4.19: T_g plotted against the a parameter of the crystal structure for hydronium jarosites synthesised in various concentrations of MeOH/H₂O solvent at 120°C. The samples are S9-S16, increasing in MeOH concentration from S9-S16, refer to Table 4.7 for further information. The graph shows that values of T_g correlate to a structural change in the a parameter of the unit cell: decreasing T_g correlates with an expansion along the a axis. The correlation between decreasing values of T_g and the expansion along the a axis also corresponds to an increasing MeOH concentration. The data points shown are sequential in MeOH concentration.

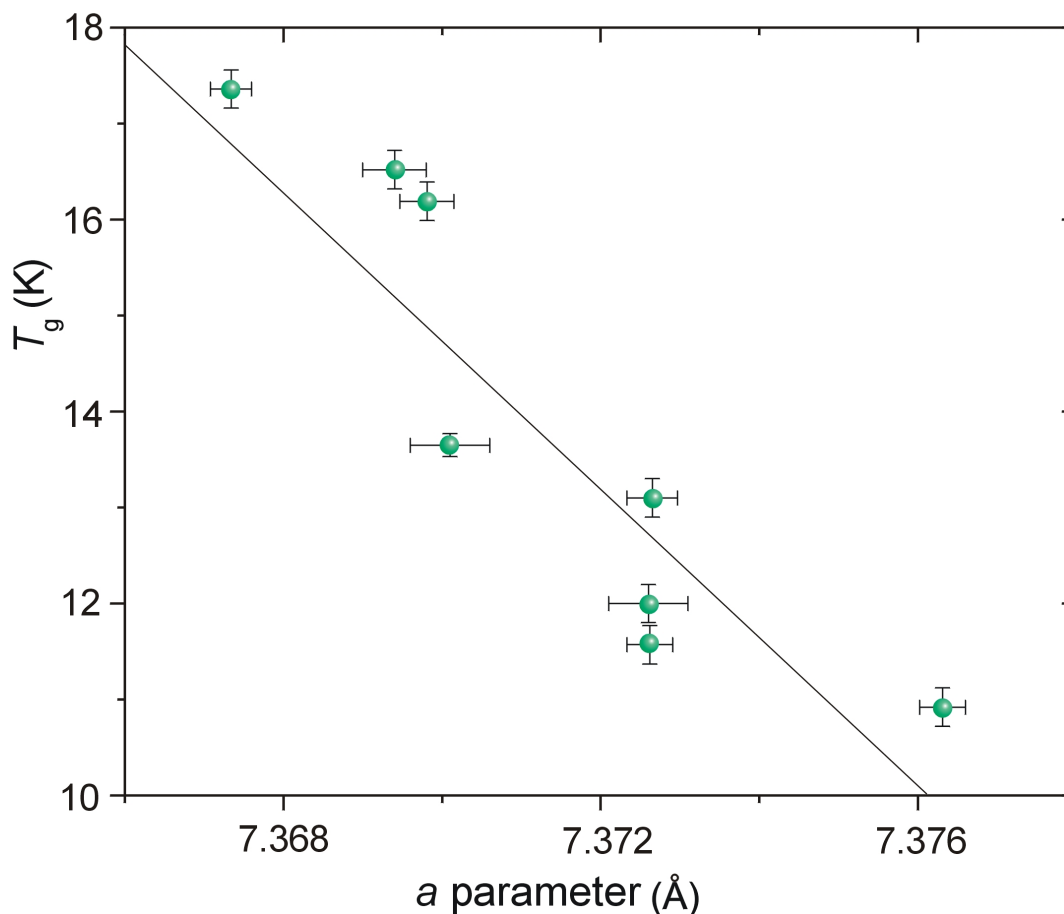


Figure 4.20: T_g plotted against the a parameter of the crystal structure for hydronium jarosites synthesised in various concentrations of MeOH/H₂O solvent at 130°C. The samples are S21-S28, increasing in MeOH concentration from S21-S28, refer to Table 4.7 for further information. The graph shows that values of T_g correlate to a structural change in the a parameter of the unit cell: decreasing T_g correlates with an expansion along the a axis. The correlation between decreasing values of T_g and the expansion along the a axis also corresponds to an increasing MeOH concentration. The data points shown are sequential in MeOH concentration.

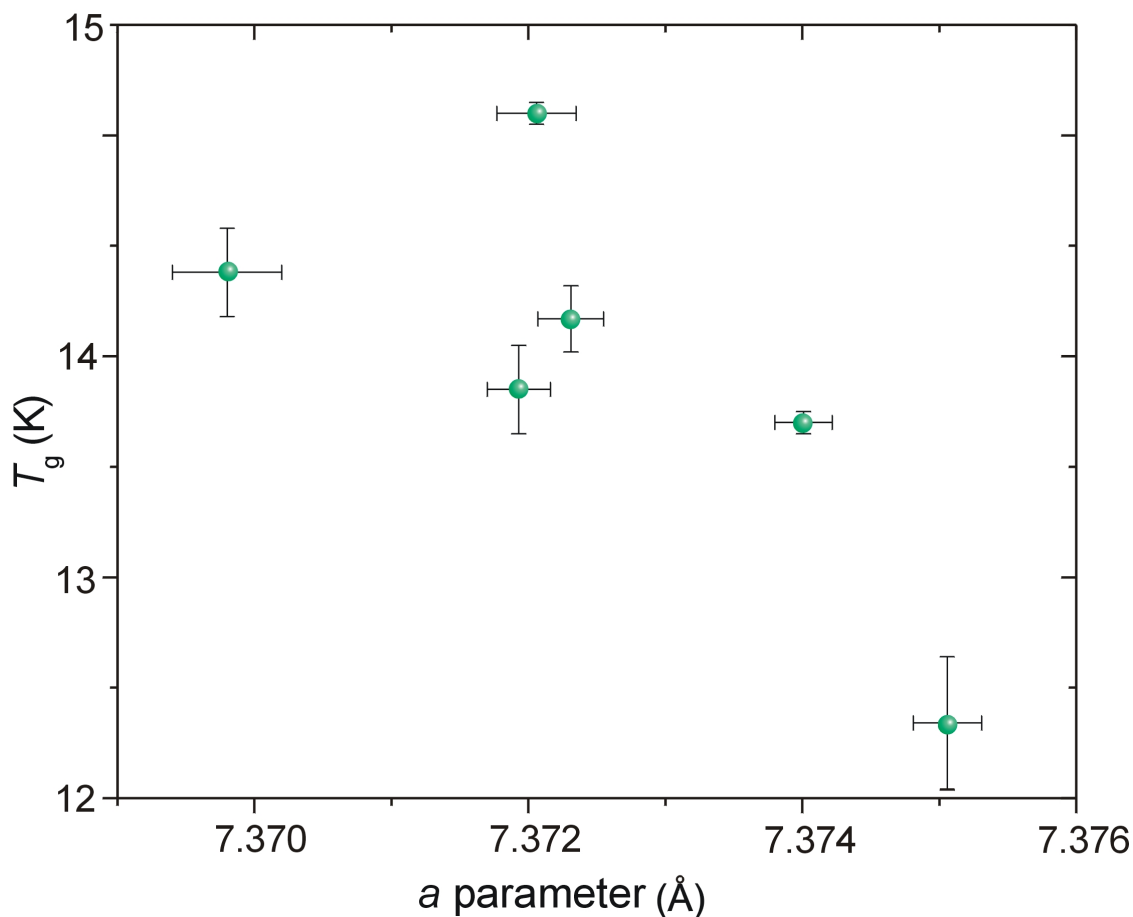


Figure 4.21: T_g plotted against the a parameter of the crystal structure for hydronium jarosites synthesised in various concentrations of MeOH/H₂O solvent at 140°C. The samples are S30-S35, increasing in MeOH concentration from S30-S35, refer to Table 4.7 for further information. The graph, unlike for other synthesis series, does not show any correlation between values of T_g and to a structural change in the a parameter of the unit cell.

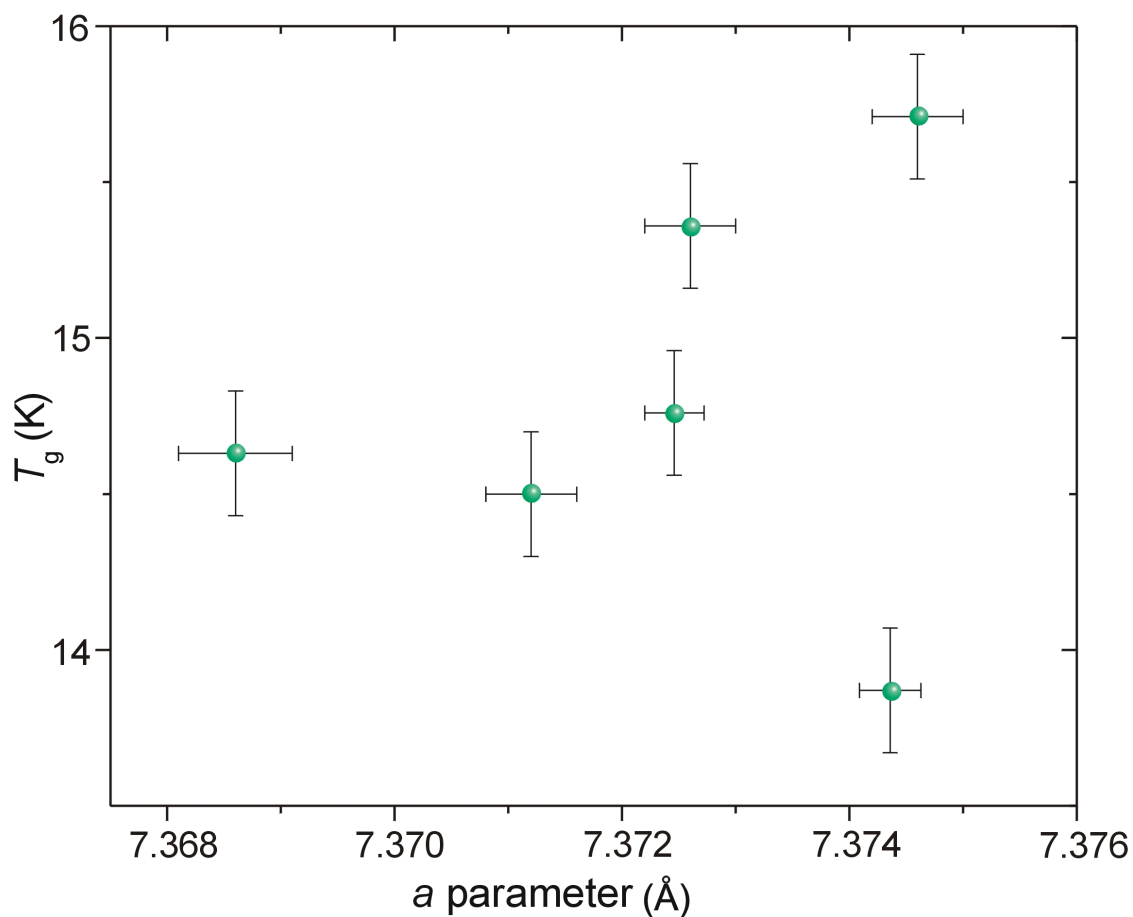


Figure 4.22: T_g plotted against the a parameter of the crystal structure for hydronium jarosites synthesised in various concentrations of MeOH/H₂O solvent at 150°C. The samples are S1-S4, increasing in MeOH concentration from S1-S4, refer to Table 4.7 for further information. The graph, unlike for other synthesis series, does not show any correlation between values of T_g and to a structural change in the a parameter of the unit cell.

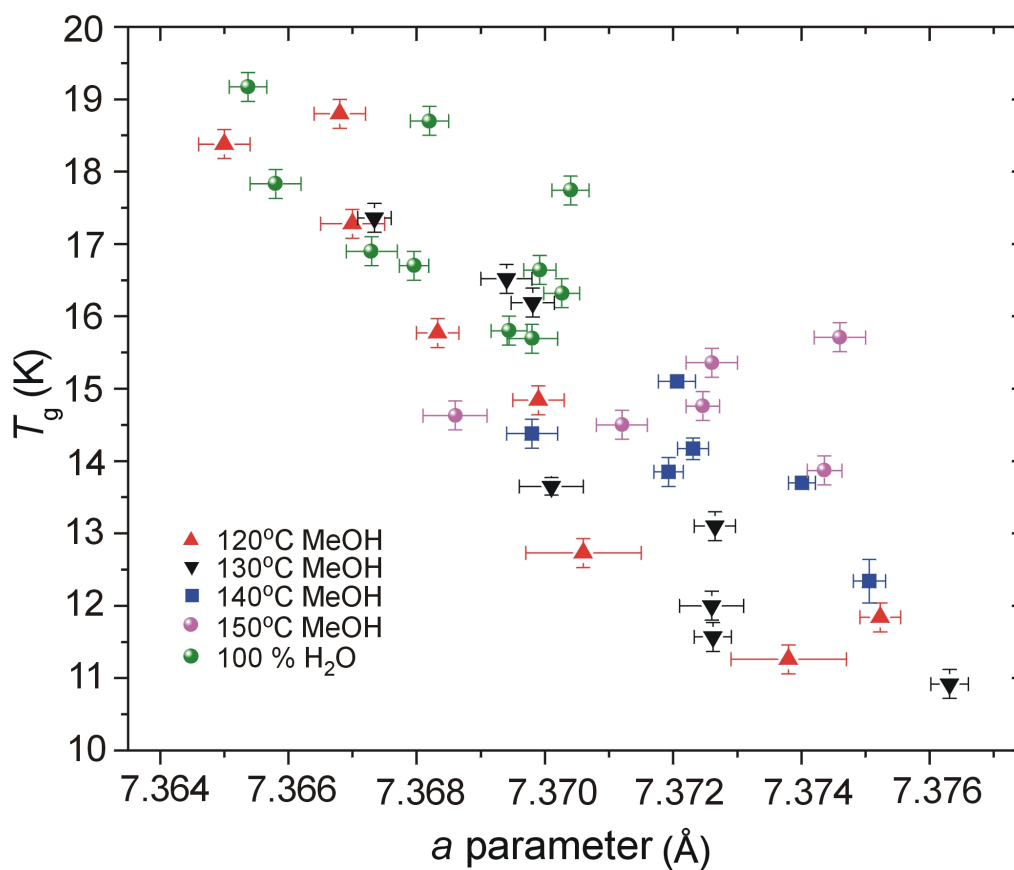


Figure 4.23: T_g plotted against the c parameter of the crystal structure for all hydronium jarosites shown in Tables 4.5 and 4.7. It shows a structural change is occurring which causes an overall expansion along a that gives rise to a corresponding decrease in T_g . This can only be said to be a trend as the distribution in the a axis widens as T_g decreases.

Atom	x	y	z	Multiplicity/ Occupancy	U_{iso}
O(H ₃ O)	0	0	0	3	0.0240(13)
Fe	0	$\frac{1}{2}$	$\frac{1}{2}$	0.979(5)	0.0054(2)
S	$\frac{2}{3}$	$\frac{1}{3}$	0.02473(6)	6	0.0044(3)
O(Fe _{apical})	0.4472(3)	0.22358(15)	0.05415(10)	18	0.0079(5)
O(S _{apical})	$\frac{2}{3}$	$\frac{1}{3}$	-0.06154(19)	6	0.0086(7)
O(Fe _{equitorial})	0.12751(16)	-0.12751(16)	0.13513(12)	18	0.0100(5)
H(OH)	0.1758	-0.1760	0.1139	18	0.012

Atom	$U_{\text{anisotropic}}$		
	U_{11}	U_{22}	U_{33}
O(H ₃ O)	0.026(2)	0.026(2)	0.020(3)
Fe	0.0044(3)	0.0062(3)	0.0050(3)
S	0.0054(4)	0.0054(4)	0.0025(5)
O(Fe _{apical})	0.0051(9)	0.0110(7)	0.0057(8)
O(S _{apical})	0.0119(10)	0.0119(10)	0.0018(14)
O(Fe _{equitorial})	0.0048(7)	0.0048(7)	0.0202(10)

Atom	U_{iso}		
	U_{11}	U_{22}	U_{33}
O(H ₃ O)	0.026(2)	0.026(2)	0.020(3)
Fe	0.0044(3)	0.0062(3)	0.0050(3)
S	0.0054(4)	0.0054(4)	0.0025(5)
O(Fe _{apical})	0.0051(9)	0.0110(7)	0.0057(8)
O(S _{apical})	0.0119(10)	0.0119(10)	0.0018(14)
O(Fe _{equitorial})	0.0048(7)	0.0048(7)	0.0202(10)

Table 4.8: Single crystal data for hydronium jarosite sample No. 24. Data was collected at Southampton university with MoK_α radiation at 85(2)K. Solved using Direct methods and refined using Shelx-97 The space group is $R\bar{3}m$ with a unit cell of $a = b = 7.34940(10)\text{\AA}$ and $c = 16.9411(4)\text{\AA}$. The R value is 0.0231

4.4.1 Structural Changes within the Hydronium Jarosites

Iron octahedra canting

Symmetry of the iron octahedra

4.4.2 Implications for the Magnetism of the Structure

4.5 Physical Characterisation of Iron Jarosite

4.5.1 Zero Field/Field Cooled Measurements

4.5.2 Hysteresis Measurements

4.5.3 Understanding the Magnetic Structure

Hydronium jarosites

Non-hydronium jarosites

4.6 Neutron Thermo-diffraction Studies and Magnetic Diffraction of Iron Jarosites

4.6.1 Neutron Powder Diffraction Technique

Nuclear Structure

Magnetic Refinement

4.7 Results and Analysis of Neutron Diffraction for the Iron jarosites

4.7.1 Nuclear Structure

4.7.2 Magnetic Structure

4.8 Origins of the Spin Glass Dynamics in Hydronium Jarosite

4.9 Origin of Long Range Magnetic Order in the Non-Hydronium Jarosites

4.10 Models to Explain the Anisotropy

Chapter 5

Chromium jarosites $S = \frac{3}{2}$

Cr jarosites are iso-structural with Fe jarosites, with a lattice of Cr^{3+} ions instead of Fe^{3+} making up the *kagomé* network. Bond distances and lattice parameters are similar to that of Fe jarosites, though there is less interpenetration between the T-O-T layers. Table 5.1 gives the crystallographic details for hydronium chromium jarosite at 85K.

5.1 The Crystallographic Structure

5.1.1 Neutron Powder Diffraction at HRPD

Neutron powder diffraction data of deuterated samples of Cr jarosites were taken at the High Resolution Powder Diffraction (HRPD) (Figure 3.9) instrument at ISIS. This was to provide high resolution data for structural refinement. HRPD is a time of flight instrument with data collected primarily at a 30-130ms window, however, the low flux and small solid angle of the low angle detector bank made magnetic structure determination not viable.

The cryostat used at HRPD is an Oxford instrument design based upon adsorption of ^3He onto a graphite mesh; the subsequent evaporation of ^3He from the mesh then allows the cryostat to reach a base temperature of 30mK, though for our experiments 250mK was the lowest needed. All samples were contained in V cans and sample preparation was done under an atmosphere of helium.

Atom	x	y	z	Multiplicity/ Occupancy	U_{iso}
O(H ₃ O)	0	0	0	3	0.0139(7)
Cr	0	$\frac{1}{2}$	$\frac{1}{2}$	0.947(4)	0.00425(15)
S	$\frac{1}{3}$	$\frac{1}{3}$	0.63935(4)	6	0.0065(2)
O(Fe _{apical})	-0.44514(10)	0.1097(2)	0.61015(7)	18	0.0093(3)
O(S _{apical})	$-\frac{1}{3}$	$\frac{1}{3}$	0.72544(13)	6	0.0098(4)
O(Fe _{equatorial})	-0.20563(12)	0.20563(12)	0.46830(9)	18	0.0126(3)
H(OH)	-0.161(2)	0.161(2)	0.4482(19)	18	0.018(8)

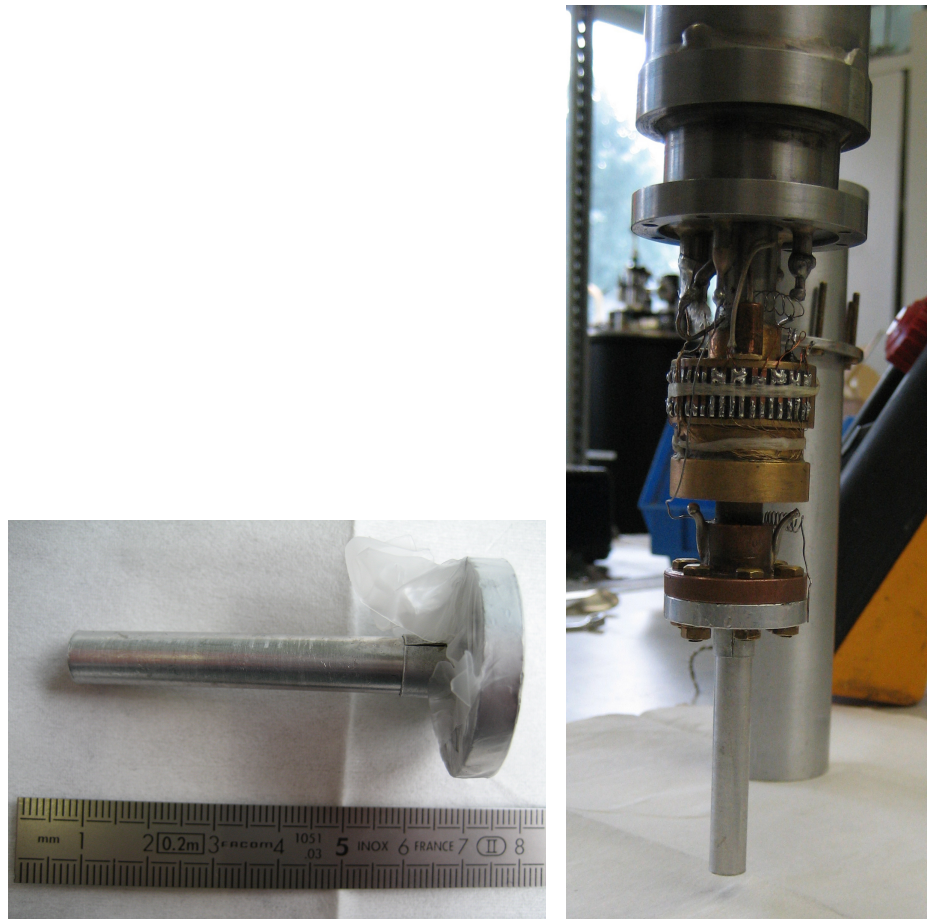
Atom	U_{11}	U_{22}	U_{33}	U_{23}	U_{13}	U_{12}
O(H ₃ O)	0.0154(10)	0.0154(10)	0.0110(13)	0.000	0.000	0.0077(5)
Cr	0.0025(2)	0.00295(18)	0.0072(2)	-0.00008(6)	-0.00071(12)	0.00124(10)
S	0.0063(3)	0.0063(3)	0.0071(3)	0	0	0.00314(13)
O(Cr _{apical})	0.0105(5)	0.0061(3)	0.0099(5)	-0.003(4)	-0.002(2)	0.00314(13)
O(S _{apical})	0.0111(6)	0.0111(6)	0.0071(9)	0.000	0.000	0.0055(3)
O(Cr _{equatorial})	0.054(4)	0.0054(4)	0.0248(7)	-0.0042(3)	0.0042(3)	0.0012(5)

Table 5.1: Single crystal data for a sample of hydronium chromium jarosite. Data was collected at Southampton university with MoK $_{\alpha}$ radiation at 85(2)K. Solved using Direct methods and refined using Shelx-97 The space group is $R\bar{3}m$ with a unit cell of $a = b = 7.2362(6)\text{\AA}$ and $c = 16.952(3)\text{\AA}$. The R value is 0.0187

5.1.2 Neutron Powder Diffraction at D20

The cryostat used for low temperature studies was a standard “orange” ILL cryostat with a ^3He insert (Figure 5.1(b)) to obtain sub 2K temperatures by pumping upon the ^3He . The base temperature for the experiment was 400mK rising to 100K maximum allowed with the ^3He insert. The wavelengths used were 1.3 and 2.44 Å for crystal structure and magnetic structure respectively. An Al can was used for sample containers and (Figure 5.1(a)) shows the setup for a ^3He insert with a Al can attached.

5.2 The Magnetic Structures of the Chromium Jarosites



(a) Al cans were used for the diffraction experiments below 2K (which included all the Cr jarosites), the divisions on the ruler are mm (b) The Al can below is attached to the ^3He insert using brass bolts. An Al sheath (shown behind) is then slipped over to protect the electronics

Figure 5.1: Pictures showing the experimental setup for sub 2K temperature diffraction studies for the Cr jarosites. Cr jarosite is gently packed into the Al can (Figure 5.1(a)) and the Al can is secured to the bottom of ^3He insert (Figure 5.1(b)).

Chapter 6

Conclusions

6.1 The Iron Jarosites

6.2 The Chromium Jarosites

6.3 Discussion of the Topological Nature of the
Kagomé Network

6.4 Comparison between the Classical and the
Quantum limit

6.5 Future Work

Appendix A

Crystallography Appendix

A.1 Rietveld Refinement

Least-Squares

Common throughout crystallography, none more so than the Rietveld method, is to find values of parameters x_{jk} from a theoretical model that generate calculated observations y_{ci} that best fit to experimental observations y_i . Equation (A.1) represents this in matrix notation.

$$\mathbf{y} = \mathbf{Ax} + \mathbf{e} \tag{A.1}$$

\mathbf{A} is a design matrix of $n \times m$,

\mathbf{e} is the error matrix.

The most satisfactory estimate of the adjustable parameters x_{jk} is when equation (3.13) is a minimum, this best holds for diagonal matrices where y_i depends linearly upon x_{jk} . To estimate the values of x_{jk} from the model $\mathbf{M}(\mathbf{x})$, which predicts the observable quantities \mathbf{y} , then as a function of \mathbf{x} the following quadratic is to be minimised.

$$\mathbf{Q} = [\mathbf{y} - \mathbf{M}(\mathbf{x})]^T \mathbf{W} [\mathbf{y} - \mathbf{M}(\mathbf{x})] \tag{A.2}$$

Chapter A. Crystallography Appendix

\mathbf{W} is the weight matrix

If the model is linear, $\mathbf{y} = \mathbf{A}\mathbf{x}$, the expectation for the observations is $\langle y_i \rangle = \mathbf{M}(\mathbf{x})$ and the expectation of the set of parameters which minimise \mathbf{Q} is equal to the correct value, $\hat{\mathbf{x}} = \mathbf{x}_c$, then the least squares matrix is unbiased, irrespective of \mathbf{W} . The lowest values for $\hat{\mathbf{x}}$ for any choice of \mathbf{W} are when observations of y_i are drawn randomly from a variance-covariance matrix, \mathbf{V}_y and $\mathbf{W} = \mathbf{V}_y$.

$$\hat{\mathbf{x}} = (\mathbf{A}^T \mathbf{V}_y^{-1} \mathbf{A}) \mathbf{A}^T \mathbf{V}_y^{-1} \mathbf{y} \quad (\text{A.3})$$

Equation (A.3) is said to be the best linear unbiased estimate of \mathbf{x} .

The problem with X-ray diffraction and neutron scattering is that they do not depend linearly on the parameters x_{jk} , so the model is non-linear. This means that S (3.13) can possess several local minima and thus returned values of $\hat{\mathbf{x}}$ will not be satisfactory to minimise \mathbf{Q} . For this to be achieved, a good starting value or approximation of another set of parameters, \mathbf{x}' is required. Furthermore, all values of y_i need to be expanded in a Taylor series about \mathbf{x}' . If $\hat{\mathbf{x}} \sim \mathbf{x}'$ then second and higher order terms of the Taylor expansion can be ignored to reach a good approximation in equation (A.4) where the gradient of \mathbf{Q} vanishes.

$$M_i(\mathbf{x}) = M_i(\mathbf{x}') + \sum_{j=1}^p (x_j - x'_j) \frac{\partial M_i(\mathbf{x}')}{\partial x_j} \quad (\text{A.4})$$

If the design matrix is set that $\mathbf{A} = \frac{\partial M_i(\mathbf{x}')}{\partial x_j}$, then the best least squares estimate is,

$$\hat{\mathbf{x}} = \mathbf{x}' + (\mathbf{A}^T \mathbf{W} \mathbf{A}^{-1} \mathbf{A}^T \mathbf{W} [\mathbf{y} - \mathbf{M}(\mathbf{x}')]) \quad (\text{A.5})$$

Since the second and further terms of the Taylor expansion have been ignored then the \mathbf{x}' will not be an unbiased estimate of $\hat{\mathbf{x}}$ and the approximation is only valid when $\mathbf{x}' = \hat{\mathbf{x}}$. This can only be achieved by a process of iteration where shifts in Δx_j produce,

$$\Delta x_j = \sum M_{ij}^{-1} \frac{\partial S_y}{\partial x_j} \quad (\text{A.6})$$

leading to

$$\Delta \mathbf{y} = \mathbf{A} \Delta \mathbf{x} + \mathbf{e} \quad (\text{A.7})$$

If we compare equation (A.7) with equation (A.1) showing the requirement that for non-linear least squares to work, then estimates of $\Delta \mathbf{x}$ have to approach zero or be very small; once this has been achieved, the refinement has reached convergence or completed the refinement cycle for that set of parameters.

A.1.1 Profile Functions

In GSAS the widely used profile function was constant wavelength number 3. It is represented in this equation.

in equation (A.8).

$$(\text{H}\Delta\text{T}) = \frac{L^2 \sin 2\theta}{4\text{HS}} \frac{\sum_{i=M}^N W_i \left[\frac{W(\delta_i) P(\Delta\text{T} - \delta_i)}{h(\delta_i) \cos \delta_i} \right]}{\sum_{i=M}^N W_i \left[\frac{W(\delta_i)}{h(\delta_i) \cos \delta_i} \right]} \quad (\text{A.8})$$

The equation is expressed as a summation because an integral can not be performed analytically, N and M therefore define the intervals for a sufficient integration. L, S and H are the diffractometer radius, detector and sample heights respectively. W and h are functions of L, S and H describing when the entire slit sees the sample and the minimum of this function tells when the Debye-Scheerer cone starts to see the sample. ΔT is the difference between the function that represents the reflection position and the function for the profile point. It is the convolution of these two functions that describe the Cagliotti parameter H .

This equation (A.8) is a convolution of the Debye-Scheerer diffraction cone for every value of 2θ with the pseudo-Voigt function (3.16c). This function is useful for profiles with asymmetry arising from low angle reflections arising in particular from X-ray diffraction because of axial divergence. ΔT is expressed in (A.9).

$$P(\Delta\text{T}) = \eta(L(\Delta\text{T}, \Gamma) + (1 - \eta)G(\Delta\text{T}, \Gamma)) \quad (\text{A.9})$$

ΔT is defined in equation (A.9) which is the modified pseudo-Voigt ((3.16c))

for X-rays. Γ is the FWHM for both Gaussian (G) and Lorentzian (L) components.

A.2 Single Crystal structure solution

To solve the structure we need to solve the structure factor, F , a complex number which represents the amplitude, $|F|$, and the phase, ϕ of each of the reflections, hkl , leading to structure factor equation (A.10),

$$F(hkl) = |F(hkl)| \cdot \exp[i\phi(hkl)] \quad (\text{A.10})$$

which has to be solved to obtain all the structural information from the diffraction pattern which is the Fourier Transform (FT) of the electron density. X-rays are scattered by the electron density, taking each point of electron density relative to the unit cell, $\rho(xyz)$, the amplitude and phase of each reflection scattered by the electron density integrated over the whole cell volume leads to the FT of electron density (A.11).

$$F(hkl) = \int_{\text{cell}} \rho(xyz) \cdot \exp[2\pi i(hx + ky + lz)] dV \quad (\text{A.11})$$

Another important consideration is the vibrational movement of the atoms. Greater thermal displacement of an atom will reduce the effective scattering power of the atom and a correction has to be applied to the individual atomic scattering factor $a(\theta)$. The correction for atomic isotropic thermal displacement is the same for powder diffraction (3.20) and atomic structure correction for single crystal diffraction is shown in equation (A.12),

$$a'(\theta) = a(\theta) \cdot \exp\left(-\frac{8\pi^2 U \sin^2 \theta}{\lambda^2}\right) \quad (\text{A.12})$$

leading to a better description of the FT of the electron density (A.13).

$$F(hkl) = \sum_j a_j(\theta) \cdot \exp(-8\pi^2 U_j \sin^2 \theta / \lambda^2) \cdot \exp[2\pi i(hx_j + Ky_j + lz_j)] \quad (\text{A.13})$$

In order to solve the structure the reverse FT of the diffraction pattern has to

Chapter A. Crystallography Appendix

be solved to obtain the electron density shown in equation (A.14),

$$\rho(xyz) = \frac{1}{V} \sum_{h,k,l} |F(hkl)| \cdot \exp[i\phi(hkl)] \cdot \exp[-2\pi i(hx + ky + lz)] \quad (\text{A.14})$$

this, however, is almost impossible because of the phase problem. Diffraction experiments simply collect intensity and the phase information of each reflection is lost. Most of the information of a diffraction experiment is contained in the intensity; deconvoluting the FT of the diffraction pattern will show a bias to the FT of the intensity of the reflection compared to the phase. Nonetheless solving the phase problem is crucial and there were two methods employed to solve equation (A.14): direct methods and Patterson methods.

A.2.1 Direct Methods

Direct methods as the name suggests tries to solve the phase problem directly. It has been shown that the phase gives more information about the atomic position in the electron density map than the amplitude [58] and direct methods should produce more

The phase and the intensity are dependent upon the electron density, by imposing constraints using expectant knowledge of the electron density, various phases can be removed. Only phases dependent upon; discrete atoms, introduction of a probability distribution function rather than discrete values and constraints by removing (Karle and Hauptman inequality [59] or ignoring (maximum value) of negative electron density will be considered.

The first constraint is typically to normalise the electron density so that all structure factors have the same peak shape. This reduces the FT to an atomic point and constrains the phase to be always produce atomic peaks in an electron density map and it allows reflections from high θ to be compared directly. A normalised structure factor is then generated as shown in equation (A.15).

$$|E(\mathbf{h})|^2 = \frac{|F(\mathbf{h})|^2}{\sum_{i=1}^N f^2} \quad (\text{A.15})$$

Chapter A. Crystallography Appendix

The next most important constraint is no negative electron density and the promotion of positive electron density. The first is defined by the Karle-Hauptman inequality [59] that imposes a constraint on the electron density to be positive as a sum of the Fourier series. A simple case of a three order determinate with centrosymmetry is shown in equation (A.16),

$$E(\mathbf{0})[|E(\mathbf{0})|^2 - |E(\mathbf{h})|^2 - |E(\mathbf{k})|^2 - |E(\mathbf{k})|^2 - |E(\mathbf{h} - \mathbf{k})|^2] + 2E(\mathbf{h})E(-\mathbf{k})E(-\mathbf{h} + \mathbf{k}) \geq 0 \quad (\text{A.16})$$

In the case of strong reflections then the likelihood of finding atomic positions is where the intersections of the electrons density waves from the h, k , (A.16) planes intersect and produce a positive region of density. This likelihood can be further enhanced with the use of a probability distribution rather than discrete values. This imposition places a greater constrained on the phases that produce positive electron density.

The equation that is generally solved in direct methods is a combination of the above mentioned constraints and by applying the constraint $\int \rho^3(\mathbf{x})dV = \max$ leading to the tangent formula (A.17), where a single term gives the phase relationship.

$$\tan(\phi(\mathbf{h})) \approx \frac{\sum_{\mathbf{k}} |E(\mathbf{k})E(\mathbf{h} - \mathbf{k})| \sin(\phi(\mathbf{k}) + \phi(\mathbf{h} - \mathbf{k}))}{\sum_{\mathbf{k}} |E(\mathbf{k})E(\mathbf{h} - \mathbf{k})| \cos(\phi(\mathbf{k}) + \phi(\mathbf{h} - \mathbf{k}))} \quad (\text{A.17})$$

Upon solving the tangent formula (A.17) reflections found with large E s are a good estimate for phase determination. Many poor reflections need to be removed and there must be a means of determining the reliability of the phases provided by the tangent formula (A.17). The quality of estimate is determined by $\alpha(\mathbf{h})$ (A.18), the larger value of $\alpha(\mathbf{h})$ the better the phase estimate. Nonetheless the initial value for $\alpha(\mathbf{h})$ is an estimate in itself.

$$\alpha(\mathbf{h}) = 2N^{-\frac{1}{2}}|E(\mathbf{h})| \left| \sum_{\mathbf{k}} E(\mathbf{k})E(\mathbf{h} - \mathbf{k}) \right| \quad (\text{A.18})$$

This further removes unwanted reflections. The process of phase determination by a random process of assigning values to define the origin of the unit cell and this can be repeated up to 5000 times for Shelx-97. The default value for the E s to be

Chapter A. Crystallography Appendix

considered in the refinement is set to 1.2, in some cases dropping the threshold to 1.0 allowed more electron density to be found and hence more atoms to be solved in the structure. The quality of these phases are assessed using a conformity of fit criteria, R_α , set out in equation (A.19).

$$R_\alpha = \frac{\sum_{\mathbf{h}} |\alpha(h\mathbf{h}) - \alpha_e(\mathbf{h})|}{\sum_{\mathbf{h}} \alpha_e(\mathbf{h})} \quad (\text{A.19})$$

$\alpha_e(\mathbf{h})$ is an estimate of $\alpha(\mathbf{h})$ which is obtained by the knowledge that the three structure factors in equation (A.16) share a common origin: they are structure invariant. Large E s will help improve the estimate given by $\alpha_e(\mathbf{h})$ and to determine an origin which then leads to determining individual structure factors.

In Shelx-97 the lowest R_α valued structure solution is then entered into the refinement. It is still possible for that to contain incorrect phase information and use of another randomly generated set of phases may be needed. They are each assigned with a random number, that can be entered into the refinement.

A.2.2 Patterson methods

The Patterson method is based upon the Patterson function (??)

$$P(uvw) = \frac{1}{V} \sum_{h,k,l} |F(hkl)|^2 \cos[2\pi(hu + kv + lw)] \quad (\text{A.20})$$

The patterson function relies on the fact hkl planes which strongly reflect X-rays is due to the atomic arrangement along those planes and by setting the phase to an effective zero, then information is retained but not necessarily easily to interpret. The map produced from the Patterson method is not an electron density map, but a map showing positions of the vectors between a set of interatomic positions but bears no relation to the origin. All resultant Patterson maps are centrosymmetric and each peak height in the Patterson map will be proportional to to the product of atomic numbers that each Patterson vector represents. Beyond small molecules ($N > 20$), with the atoms having similar scattering power then a Patterson map will look overcrowded as the vectors describing interatomic positions will all be similar and numerate as $P(uvw)$ will show N^2 interatomic positions.

Chapter A. Crystallography Appendix

The Patterson method will become very useful for searching for the atomic coordinates of heavy atoms aided with a centre of symmetry. The peaks of the pairing of the interatomic vector separation will be much higher and thus able to determine these positions. Knowing the coordinates of these heavy atoms an approximate phase can then be input back into equation (A.14) and an iterative process is undertaken to solve the structure.

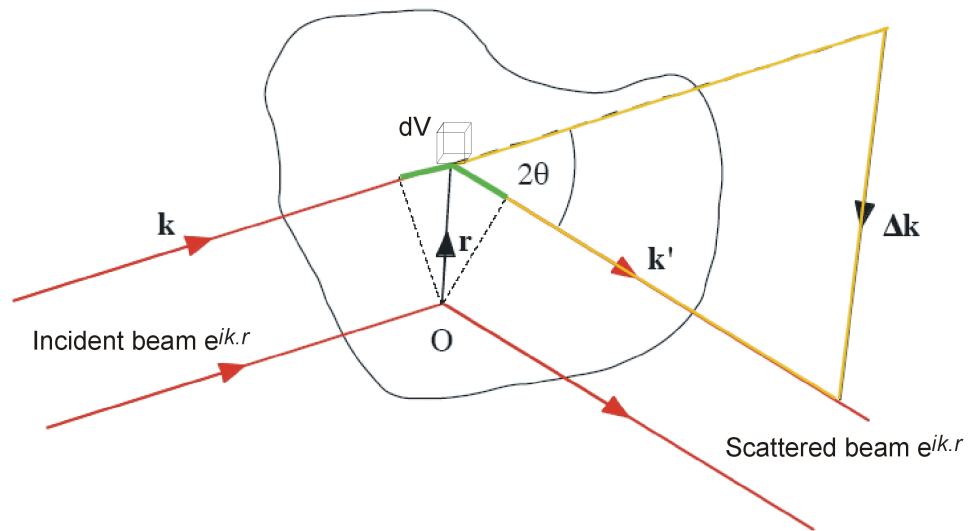


Figure A.1: This Figure shows two aspects of diffraction. O is the origin of a volume element, there are two origins separated by a distance r . The difference in diffraction phase angle for the wave vectors \mathbf{k} and \mathbf{k}' are $\mathbf{k} \cdot \mathbf{r}$ and $-\mathbf{k}' \cdot \mathbf{r}$ respectively. The total phase angle difference is $(\mathbf{k} - \mathbf{k}') \cdot \mathbf{r}$. The scattering vector is, $\Delta\mathbf{k}$, defined as $\mathbf{k} + \Delta\mathbf{k} = \mathbf{k}'$. In elastic scattering $\mathbf{k}' = \mathbf{k}$ and for a Bragg reflection to occur, $\Delta\mathbf{k}$ has to coincide with \mathbf{G} ($\Delta\mathbf{k} = \mathbf{G}$) for a particular reciprocal lattice vector and the occurrence is at an angle 2θ , twice the angle from the origin of scattering for wave vector \mathbf{k} .

Bibliography

- [1] C. Panagopoulos, M. Majoros, T. Nishizaki, and H. Iwasaki, *Physical Review Letters* **96**, 047002 (2006).
- [2] M. WILDNER and G. GIESTER, *Neues Jahrbuch Fur Mineralogie-Monatshefte* 296 (1991).
- [3] J. Rodriguez-Carvajal, *Physica B: Condensed Matter* **192**, 55 (1993).
- [4] T. Roisnel and J. Rodriguez-Carvajal, *Epdic 7: European Powder Diffraction, Pts 1 And 2* **378-3**, 118 (2001).
- [5] J. E. DUTRIZAC, J. L. JAMBOR, and J. B. OREILLY, *CIM BULLETIN* **76**, 78 (1983).
- [6] J. E. Dutrizac and J. L. Jambor, *Reviews in Mineralogy and Geochemistry* **40**, 405 (2000).
- [7] G. Klingelhofer, R. V. Morris, P. A. De Souza, D. Rodionov, and C. Schroder, *Hyperfine Interactions* **170**, 169 (2006).
- [8] J. E. Dutrizac and S. Kaiman, *The Canadian Mineralogist* **14**, 151 (1976).
- [9] C. J. Serna, C. P. Cortina, and J. V. G. Ramos, *Spectrochimica Acta* **42A**, 729 (1986).
- [10] J. S. W. G. M. Loiacono, G. Kosticky, *American Mineralogist* **67**, 406 (1982).
- [11] W. Gilbert, in *De Magnete, Magneticisque Corporibus et de Magno Magnete Tellure (Facsimile of 1893 Mottelay translation)*, edited by P. F. Mottelay (Dover Publications, ADDRESS, 1600).

BIBLIOGRAPHY

- [12] S. Geshwind, Phys. Rev. **121**, 363 (1961).
- [13] A. M. Afanasev, V. D. Gorobchenko, D. S. Kulgawczuk, and I. I. Lukashevich, Phys. Stat. Solidi (a) **26**, 697 (1974).
- [14] P. Bonville, V. Dupuis, E. Vincent, P. E. Lippens, and A. S. Wills, HYPERFINE INTERACTIONS **168**, 1085 (2006).
- [15] G. Toulouse, Commun Phys **2**, 115 (1977).
- [16] P. W. Anderson, P. A. Lee, M. Randeria, T. M. Rice, N. Trivedi, and F. Zhang, Journal of Physics: Condensed Matter **16**, R755 (2004).
- [17] P. W. ANDERSON, Science **235**, 1196 (1987).
- [18] J. KONDO, Progress Of Theoretical Physics **32**, 37 (1964).
- [19] M. A. RUDERMAN and C. KITTEL, Physical Review **96**, 99 (1954).
- [20] M. G. TOWNSEND, G. LONGWORTH, and E. ROUDAUT, PHYSICAL REVIEW B **33**, 4919 (1986).
- [21] S. A. Earle, A. P. Ramirez, and R. J. Cava, Physica B-Condensed Matter **262**, 199 (1999).
- [22] J. E. Dutrizac and T. T. Chen, Metallurgical And Materials Transactions B-Process Metallurgy And Materials Processing Science **36**, 33 (2005).
- [23] S. Shimizu and H. Hamada, Angew. Chem. Int. Ed. **38**, 2725 (1999).
- [24] D. Grohol and D. G. Nocera, Journal Of The American Chemical Society **124**, 2640 (2002).
- [25] D. Grohol, D. G. Nocera, and D. Papoutsakis, Physical Review B **67**, 064401 (2003).
- [26] A. M. L. Smith, Ph.D. thesis, University of London, 2004.
- [27] R. L. Carlin, *Magneto Chemistry* (Springer-Verlag, ADDRESS, 1986).

BIBLIOGRAPHY

- [28] A. S. Wills and A. Harrison, *Journal Of The Chemical Society-Faraday Transactions* **92**, 2161 (1996).
- [29] T. G. Worlton, J. D. Jorgensen, R. A. Beyerlein, and D. L. Decker, *Nuclear Instrument Methods* **137**, 331 (1976).
- [30] H. M. RIETVELD, *ACTA CRYSTALLOGRAPHICA* **22**, 151 (1967).
- [31] H. M. RIETVELD, *JOURNAL OF APPLIED CRYSTALLOGRAPHY* **2**, 65 (1969).
- [32] G. CAGLIOTI, A. PAOLETTI, and F. P. RICCI, *NUCLEAR INSTRUMENTS AND METHODS* **3**, 223 (1958).
- [33] L. W. FINGER, D. E. COX, and A. P. JEPHCOAT, *JOURNAL OF APPLIED CRYSTALLOGRAPHY* **27**, 892 (1994).
- [34] W. A. DOLLASE, *JOURNAL OF APPLIED CRYSTALLOGRAPHY* **19**, 267 (1986).
- [35] M. A. Z, *ZEITSCHRIFT FUR KRISTALLOGRAPHIE* **81**, 285 (1932).
- [36] R. J. HILL and H. D. FLACK, *Journal Of Applied Crystallography* **20**, 356 (1987).
- [37] L. J. Farrugia, *J. Appl. Cryst.* **32**, 837 (1999).
- [38] A. L. Spek, *Acta Cryst.* **A46**, C34 (1990).
- [39] J. Kubisz, *Mineralogia Polonica* **1**, 47 (1970).
- [40] N. LAZAROFF, W. SIGAL, and A. WASSERMAN, *APPLIED AND ENVIRONMENTAL MICROBIOLOGY* **43**, 924 (1982).
- [41] J. E. DUTRIZAC, *METALLURGICAL TRANSACTIONS B-PROCESS METALLURGY* **14**, 531 (1983).
- [42] A. Harrison, A. S. Wills, and C. Ritter, *Physica B* **241**, 722 (1997).

BIBLIOGRAPHY

- [43] A. S. Wills, V. Dupuis, E. Vincent, J. Hammann, and R. Calemczuk, *Physical Review B* **62**, R9264 (2000).
- [44] A. S. Wills, A. Harrison, S. A. M. Mentink, T. E. Mason, and Z. Tun, *Europhysics Letters* **42**, 325 (1998).
- [45] K. Kandori, J. Sakai, and T. Ishikawa, *PHYSICAL CHEMISTRY CHEMICAL PHYSICS* **2**, 3293 (2000).
- [46] K. Kandori, T. Shigetomi, and T. Ishikawa, *Colloids And Surfaces A-Physicochemical And Engineering Aspects* **232**, 19 (2004).
- [47] K. Sasaki and H. Konno, *CANADIAN MINERALOGIST* **38**, 45 (2000).
- [48] S. MUSIC, Z. OREHOVEC, S. POPOVIC, and J. CZAKONAGY, *Journal Of Materials Science* **29**, 1991 (1994).
- [49] D. Baron and C. D. Palmer, *Geochimica Et Cosmochimica Acta* **60**, 185 (1996).
- [50] J. E. Dutrizac and J. L. Jambor, *Jarosites and their application in hydrometallurgy*, 2000.
- [51] J. A. RIPMEESTER, C. I. RATCLIFFE, J. E. DUTRIZAC, and J. L. JAMBOR, *CANADIAN MINERALOGIST* **24**, 435 (1986).
- [52] B. Gasharova, J. Gottlicher, and U. Becker, *Chem. Geol.* **215**, 499 (2004).
- [53] P. C. SINGER and W. STUMM, *SCIENCE* **167**, 1121 (1970).
- [54] N. F. Gray, *WATER RESEARCH* **30**, 1551 (1996).
- [55] R. BOISTELLE and J. P. ASTIER, *Journal Of Crystal Growth* **90**, 14 (1988).
- [56] A. A. Zavitsas, *JOURNAL OF PHYSICAL CHEMISTRY B* **105**, 7805 (2001).
- [57] A. M. L. Smith, K. A. Hudson-Edwards, W. E. Dubbin, and K. Wright, *APPLIED GEOCHEMISTRY* **21**, 1251 (2006).
- [58] G. N. Ramachandran and R. Srinivasan, *Nature* **90**, 159 (1961).

BIBLIOGRAPHY

- [59] J. Karle and H. Hauptman, *Acta Cryst.* **3**, 181 (1950).